SAPIENZA
UNIVERSITÀ DI ROMA

PhD Program in ENERGY and ENVIRONMENT

XXXVII Cycle

Plasma thruster design for space transportation

PhD Thesis

Scuola di Dottorato in Scienze e Tecnologie per l'Innovazione Industriale
Facoltà di Ingegneria Civile e Industriale
Dipartimento di Ingegneria Astronautica, Elettrica ed Energetica

Daniele Iannarelli

Advisor
Prof. Antonella Ingenito

Co-Advisor
Dr. Ing. Francesco Napoli

A.A. 2024-2025

To me,
to the diligence I putted in this study
and to the passion that I have for this
science that leads me here.

Acknowledgements

My acknowledgment for the help and the vicinity received in this period of the PhD research goes to my family that was next to me in all these three years and in particular to my mother and my father that helped me in taking care of the daily needs, to my supervisor that in the PhD period was a reference for the work done and always available for advices to guide me in the necessary choices to take within the PhD project and to my co-advisor that was close to me in the entire development of the PhD research while I was maturating my new knowledge on plasma physics and on plasma propulsion, helping me to complete the PhD research project. Moreover I thank all my research group with which we spent wonderful and intense three years of study and work with which I will continue to collaborate for publications and research projects and in the end to my friends that were close to me during the three years of the PhD project and that made, with moments of freedom, this experience less hard and more complete.

Daniele Iannarelli, Rome, 23 January 2025

Abstract

The "Plasma Thrusters Design for Sustainable Space Transportation" project is a research initiative born from the collaboration between La Sapienza University of Rome's School of Aerospace Engineering (SIA) and the ENEA Research Centre in Frascati. This innovative plasma thruster project of arose from the PROTO-SPHERA experiment at the Frascati ENEA Research Centre, a new plasma magnetic confinement experiment aiming to generate a spherical, simply connected plasma with no central metallic conductor. This experiment inspired the study and conceptualization of a new nuclear fusion plasma thruster. The PROTO-SPHERA experiment is at the forefront of technology for machines that confine plasma magnetically, as it can generate a closed magnetic configuration for confining plasma from an axial plasma discharge. This magnetic configuration is also known as "simply connected" because it contains no voids or holes. This magnetic configuration is of interest in the study of magnetic reconnections, astrophysical space plasmas, and its potential to be transformed into a nuclear fusion reactor.

The lightness, energy efficiency, simple construction and low enviromental impact of PROTO-SPHERA led to its investigation as a plasma thruster and fusion plasma thruster. Based on the experimental results obtained from the machine in terms of plasma production and generation of spherical plasmas, it was decided to evaluate the performance of a nuclear fusion thruster in a scaled configuration of the present machine. The idea of transforming the PROTO-SPHERA experiment into a plasma thruster gave rise to this PhD project, which focuses on designing a helicon plasma thruster for cislunar missions and a nuclear fusion thruster for interplanetary missions. This category of low-thrust thrusters can be used for space flight beyond the terrestrial atmosphere, either in orbit or during interplanetary flight. This design study enables experimentation with this type of technology in laboratory setting and with space missions that can be performed using these rocket engines. In an international scenario in which demand for access to space is increasing rapidly, with hundreds of satellites launched into orbit every year and the need to remove decommissioned satellites, studying and designing innovative propulsion systems enables safe orbital transfers with high efficiency. A plasma nuclear fusion thruster, for example, is a space transportation system with a very high specific impulse that can provide moderate thrust (from few Newtons to thousands of Newtons) and can be used for interplanetary space missions carrying heavy payloads. Therefore, its application in this PhD project was conceived for interplanetary transfers within the Solar System. The helicon thruster, on the other hand, is in the low thrust and high specific impulse category, although this is lower than that of nuclear fusion thrusters. It is suitable for orbital transfers within the sphere of influence of Earth.

The design of the plasma thrusters is performed modelling the physics of their main components, which allows us to predict their behavior and performance and also determine their size. The resulting engines are then simulated using electromagnetic modelling to determine their operating conditions and propulsive performance. In particular, a design method is proposed for the helicon antenna and magnetic nozzle of the helicon thruster, based on analytical models and plasma simulations that size the thruster for assigned mission requirements. A design method has also been developed for the nuclear fusion thruster of a scaled fusion magnetic configuration obtained from

the PROTO-SPHERA experiment, combined with a mission analysis for an interplanetary nuclear fusion thruster mission to determine the engine size required to satisfy the mission's specifications.

These plasma thrusters are new technologies for space flight and are currently at the laboratory stage. They must be tested to increase their TRL (Technology Readiness Level), before they can be used. This PhD study proposes new modelling for both the helicon and nuclear fusion thrusters to increase the understanding of their main working principles and to facilitate their design using readily applicable sizing methods. The results obtained in this PhD study can be used in future new research projects on plasma thrusters and to design new propulsive systems based on the plasma technologies here reported.

Keywords: plasma, magnetic confinement, plasma thrusters, helicon thruster, fusion reactions, nuclear fusion thruster.

Contents

List of Figures

List of Tables

Nomenclature

1 Introduction **1**
1.1 Introduction to electric propulsion . . . 1
1.2 State of the art of the electric propulsion systems . . . 2
1.3 PhD project: objectives and obtained results . . . 3

2 Plasma propulsion physics **6**
2.1 Plasma magnetohydrodynamic description . . . 6
2.2 Plasma magnetic confinement and orbital theory . . . 8
2.3 Waves in plasmas and use of helicon waves . . . 10
2.4 Plasma acceleration in a magnetic field . . . 12
2.5 Equilibrium theory of the screw-pinch . . . 13
2.6 Plasma magnetohydrodynamic equilibrium (Grad-Shafranov equation) . . . 16
2.6.1 Analytical solution of the Grad-Shafranov equation: Solov'ev solution . . . 22
2.7 Thermonuclear fusion physics . . . 25
2.7.1 The Lawson criterion . . . 28
2.7.2 The nuclear fusion reactor: the tokamak . . . 31

3 Helicon thruster design **34**
3.1 Helicon thruster design for cislunar cargo missions . . . 34
3.2 The HELICARGO project . . . 36
3.3 Design of a helicon antenna . . . 37
3.3.1 Design method 1 . . . 37
3.3.2 Design method 2 . . . 40
3.3.3 Design method 3 . . . 41
3.3.4 Simulations for the design of the helicon antenna . . . 42
3.4 Design, FEM and PIC simulations of the helicon thruster . . . 46
3.4.1 0-D global design model . . . 48
3.4.2 Full-wave simulation model for the ionization chamber . . . 51
3.4.3 Particle-in-cell expansion model in the magnetic nozzle . . . 52
3.4.4 Simulation results . . . 53

4 Conceptual study of a nuclear fusion plasma thruster **60**
4.1 The PROTO-SPHERA experiment of the ENEA Research Center in Frascati . . . 60
4.2 Experimental estimate of the PROTO-SPHERA pinch electron temperature . . . 69

4.3 2D Magnetohydrodynamic equilibrium computation of the PROTO-SPHERA experiment . . . 81
4.3.1 The MHD equilibrium code (LIBRA v 1.0) . . . 81
4.4 Conceptual design of a nuclear fusion thruster based on the PROTO-SPHERA experiment for interplanetary missions . . . 89
4.4.1 Mission analysis of the nuclear fusion thruster . . . 90
4.4.2 2D equilibrium of the PROTO-SPHERA experiment . . . 99
4.4.3 Fusion scaling of the PROTO-SPHERA experiment and fusion plasma thruster performance . . . 110

5 Conclusion **118**

Bibliography **119**

List of Figures

2.1 Comparison between the analytical solution and the numerical solution 24
2.2 Plasma pressure distribution 24
2.3 Poloidal flux function distribution Ψ 24
2.4 Cross sections of the $D-^3He$ fusion reaction mechanism 26
2.5 Coefficient of the fusion reaction rate for the considered reactions, $<\sigma v>_{ij}$ 27
2.6 Fusion reactions power 27
2.7 Lawson criterion for the fusion reaction Deuterium-Tritium 31
2.8 Image of the tokamak ITER [1] 32

3.1 Mechanical design of the Nagoya type-III helicon antenna 37
3.2 Comparison of the antenna resistance values for the validation of the FEM code used in this work. ($B_0 = 100mT$, $p_n = 2Pa$, $b = 3cm$, $L_a = 5cm$, $T_e = 3eV$, $f = 15MHz$,[2]) 43
3.3 The antenna-plasma resistance (R_a) computed as function of the antenna length (L_a) (Case 1) 45
3.4 The antenna-plasma resistance (R_a) computed as function of the antenna length (L_a) (Case 2) 45
3.5 The antenna-plasma resistance (R_a) computed as function of the antenna length (L_a) (Case 3) 45
3.6 Modulus (in dB) of the S_k function in the Gauss plane, for the three simulation cases 46
3.7 Geometry of the ionization chamber, with highlighted the considered plasma parameters and the quasi-neutral plasma density values in the relevant positions 47
3.8 Particle-In-Cell simulation scheme for the magnetic nozzle, indicating the boundary conditions for the particles and the electric potential. The injection region is extended from $r = 0$ up to $r = R$. Notes that the graphed magnetic field is only qualitative and the simulations consider only the region where it is completey divergent. 53
3.9 Graphical solution of the plasma power balance equation for the helicon thruster with an input RF power of almost 2kW 55
3.10 Longitudinal oscillation of the axial component of the helicon magnetic field (Bz) . . 56
3.11 Magnetic induction field intensity and current lines 57
3.12 Evolution of the potential at infinity relative to the nozzle throat (positioned at z = 6 cm, r = 0). This potential difference is mediated in time on a window of 0,25 μs . 57
3.13 2D plasma properties maps, that show (a) the electric potential, (b) electric field intensity with direction, (c) electron density, (d) electron temperature, (e) relative charge density $(n_i - n_e)/n_e$, and (f) axial magnetic force density. The electric potential is assumed equal to 0 at the nozzle throat ($z = L/2, r = 0$). The more external magnetic field line that starts within the ionization chamber is shown as a black line. Results are time averaged on a window of $0,25\mu s$ and they are computed at a simulation time of $44\mu s$ 59

4.1 Composed image of the Crab Nebula built with the data collected in time from three space telescopes: Chandra represented in blu and white, Hubble in violet and Spitzer in dark pink. . . . 60
4.2 Pinch+torus magnetic configuration of the PROTO-SPHERA experiment and distribution of the poloidal coils divided in Group A and Group B [3]. . . . 61
4.3 Formation and evolution of the plasma central column and of the spherical torus [4, 5] 61
4.4 Pinch+torus magnetic configuration of the PROTO-SPHERA experiment with the addition of external coils PFExt . . . 67
4.5 Schematic of the PROTO-SPHERA power feeding system and of the vacuum chamber [3]. . . . 68
4.6 Magnetic configurations of the PROTO-SPHERA experiment with hydrogen plasma: (a)screw-pinch, (b)screw-pinch + torus . . . 69
4.7 Flowchart that describes the iterative procedure theorized for the estimation of the pinch electron temperature . . . 78
4.8 Radial equilibrium profiles of the plasma in the screw-pinch computed for two atomic species Hydrogen and Helium, in order: (a) magnetic field modulus, (b) current density modulus, (c) electron temperature, (d) neutrals density. . . . 79
4.9 Flowchart of the resolutive algorithm of the linearized Grad-Shafranov equation . . . 85
4.10 Convergence of the α_g parameter . . . 86
4.11 Convergence of the total toroidal plasma current I_T . . . 86
4.12 Relative error on the Ψ map . . . 87
4.13 Distribution of the dimensionless poloidal flux function $\tilde{\Psi}$ . . . 87
4.14 Distribution of the poloidal flux function Ψ . . . 88
4.15 Comparison between the computed solutions for DTT with the LIBRA code and with a reference code . . . 88
4.16 Image that shows an interplanetary transfer Earth-Mars . . . 90
4.17 Trajectory in the geocentric reference system . . . 94
4.18 Velocity in the geocentric reference system . . . 94
4.19 Exit trajectory from the Earth sphere of influence . . . 95
4.20 Interplanetary trajectory of the space vehicle . . . 95
4.21 Arrival trajectory of the space vehicle in the Mars sphere of influence . . . 96
4.22 Orbital radius variation in the martian reference system . . . 96
4.23 Velocity variation in the martian reference system . . . 97
4.24 Velocity profile of the interplanetary transfer in the heliocentric reference system . . . 98
4.25 Total mass variation of the space vehicle in the interplanetary transfer . . . 98
4.26 Distribution of the poloidal magnetic field of the PROTO-SPHERA screw-pinch . . . 100
4.27 Total plasma current density distribution in dB . . . 101
4.28 Plasma pressure distribution of the screw-pinch . . . 101
4.29 Contour plot of the screw-pinch poloidal flux function Ψ . . . 102
4.30 Distribution of the screw-pinch function $\tilde{\Psi}$ . . . 103
4.31 Convergence profile of the total plasma toroidal current of the screw-pinch . . . 103
4.32 Relative error convergence on the total toroidal plasma current of the screw-pinch at successive iterations . . . 104
4.33 Poloidal magnetic field distribution of the pinch+torus PROTO-SPHERA MHD equilibium . . . 107
4.34 Distribution of the function Ψ of the pinch+torus MHD PROTO-SPHERA equilibrium configuration . . . 108
4.35 Pressure distribution of the pinch+torus MHD PROTO-SPHERA equilibrium configuration . . . 109
4.36 Convergence of the toroidal plasma current of the PROTO-SPHERA pinch+torus MHD equilibrium configuration . . . 109

4.37 Relative error on the toroidal plasma current of the PROTO-SPHERA pinch+torus MHD equilibrium configuration 110
4.38 Poloidal field of the scaled non fusionist PROTO-SPHERA experiment with $L_1 = 2$. 111
4.39 Plasma shape (separatrix) of the scaled non fusionist PROTO-SPHERA experiment with $L_1 = 2$ 111
4.40 Ψ function distribution of the scaled non fusionist PROTO-SPHERA experiment with $L_1 = 2$ 112
4.41 Plasma pressure of the scaled non fusionist PROTO-SPHERA experiment with $L_1 = 2$112
4.42 Convergence of the toroidal current (red line) and screw-pinch current (blu line) of the scaled non fusionist PROTO-SPHERA experiment with $L_1 = 2$ 113
4.43 Flowchart of the NUCLEUS code for the fusion power balance 114

List of Tables

1.1 Electric thrusters classification 2

3.1 Design parameters of the helicon antenna 44
3.2 Comparison of the three design methods 44
3.3 Parameters considered in the global model for sizing the helicon thruster. 54
3.4 Parameters considered for the PIC simulation of the magnetic nozzle expansion. . . . 58

4.1 Comparison between the numerical data (indicated with the subscript *num*) and the experimental data (indicated with the subscript *exp*). The value indicated with the asterisk * is referred to a reference value taken from the shot 1910. 80
4.2 Design data table of the DTT tokamak 85
4.3 Table of the Earth-Mars mission analysis 91
4.4 Table of the simulated data of the pinch+torus MHD equilibrium 105
4.5 Properties of the scaled PROTO-SPHERA experiment ($L_1 = 2$) 113
4.6 Mass budget of the fusion propulsion system 116
4.7 Performance of the fusion plasma thruster based on the scaled fusion PROTO-SPHERA experiment 117

Nomenclature

τ_E	confinement time s
$(\hat{r}, \hat{\phi}, \hat{z})$	cylindrical reference system
$(\hat{x}, \hat{y}, \hat{z})$	cartesian reference system
ΔV	velocity increment m/s
$\dot{m}_{\mathrm{i}}$	ion mass flow rate kg/s
μ_0	vacuum magnetic permeability H/m
Ψ	poloidal flux function Tm^2
ρ	density kg/m^3
ε	electric permittivity $C^2N^{-1}m^{-2}$
ε_0	vacuum electric permittivity $C^2N^{-1}m^{-2}$
$\vec{v}$	velocity vector m/s
c_{s}	speed of sound m/s
g_0	gravity acceleration m/s^2
k_B	Boltzmann constant J/K
$ln\Lambda$	Coulomb logarithm
m_e	electron mass kg
m_i	ion mass kg
n_e	electron density $particles/m^3$
n_i	ion density $particles/m^3$
n_n	neutrals density $particles/m^3$
p_e	electron pressure Pa
p_i	ion pressure Pa
T_e	electron temperature K
T_i	ion temperature K
$v_{\parallel}$	parallel velocity to the magnetic field line m/s
$v_{\perp}$	perpendicular velocity to the magnetic field line m/s

$v_{th,e}$	electron thermal velocity m/s
Z_i	ion charge
$(\hat{r}, \hat{\theta}, \hat{z})$	cylindrical reference system
c	speed of light m/s
e	electron charge C
i	imaginary unit
t	time s

Chapter 1

Introduction

1.1 Introduction to electric propulsion

Electrical space propulsion is a category of system propulsion in which the technological limits of the traditional space propulsion (liquid, solid and hybrid propulsion) are surpassed, reaching propellant temperatures and exhaust velocities higher than the chemical propulsion. The higher temperature and exhaust velocities of the electric propulsion system allow a more efficient propellant consumption leading to lower propellant storage on the space vehicles and the possibility to do space mission with high velocity increment that would be otherwise impossible to do with the traditional chemical propulsion technology. Plasma thrusters are in the category of the electric propulsion, they have the features of merit mentioned before for the electric propulsion and in particular they are fed by electric feeding system and the propellant that is accelerated is in plasma state. The propellant can be in gaseous state (electrothermal propulsion) and in this case it is accelerated with a propulsive nozzle, or it can be in plasma state (electromagnetic and electrostatic thrusters) and in this case it is accelerated with a magnetic nozzle using the Lorentz force or with acceleration grids using the Coulomb force. A classification scheme for the electric propulsion is illustrated in Table 1.1. Each type of thruster is reported with an example system, which are designed or in development phase, with its technical data (datasheet). From the table the performances of the electric thrusters are evident and they all have a high specific impulse, exeption made for the resistojet and the arcjet that mantain the propellant in gaseous state, and a low thrust that is below 1 Newton as order of magnitude for the majority of the electric thrusters. Among the technologies reported in Table 1.1 the plasma thrusters mostly developed, with the highest TRL and with a high specific impulse are the hall effect thrusters (HET), already integrated in the satellite Smart-1 of the European Space Agency and launched for a lunar mission. Plasma thrusters treated in this thesis, instead, are among the most innovative and promising technologies under design for the space flight, even if for now they are the less mature being still laboratory technologies not already tested in flight. The helicon thruster, for example, is a promising plasma thruster technology that has different advantages with respect to the traditional electrical thrusters, it is indeed an electrical thruster without electrodes that therefore is not subjected to metallic erosion. It does not require a neutralizer in its design because the plasma that flows in it is globally neutral and it stays like that also in the jet. The helicon thruster is also a system of easy design because its main components are a helicon antenna of cylindrical geometry used for the plasma ionization and electromagnets that generate a desired

topology of the magnetic field for the plasma confinement and acceleration. The helicon antenna system for the plasma generation has been studied from the 1970 with the discovery from Boswell [6] that simple antennas that excited helicon waves in magnetized plasmas, could generate high density and low temperature plasma. The study on helicon waves and on helicon antennas has been conducted in years in many successive studies both theoretical and experimental, arriving to the conceptualization and the design of the first helicon thrusters that have succeded in ignition test and they have demonstrated their functionality, such as the helicon thruster from the University of Stuttgart [7] or the helicon thruster from the University Carlo III of Madrid, which was studied under the european project HIPATIA [8].

Table 1.1: Electric thrusters classification

Electric propulsion					
Category	**Name**	**Thruster**	**Power (kW)**	**Specific impulse (s)**	**Thrust (mN)**
Electrothermal propulsion	Resistojet	MR-501 B [9]	0,493	303	370
	Arcjet	MR-510 [10]	2	585	258
	Nuclear fission thruster	DRACO [11]	in progress	>800	-
Electromagnetic propulsion	Hall effect thruster (HET)	Smart-1 [12]	1,19	1540	68
	Magnetoplasma--dynamic thruster (MPD)	SX3 [13]	100	4665	2750
	Pulsed Plasma Thruster (PPT)	PETRUS 1J [14]	0,003	699	0,082
	Helicon thruster	HT [15]	2	N.A.	7,5
	VASIMR	VX-200 [16]	100	3400	3000
	Nuclear fusion thruster	PFRC [17]	$10^3 - 4 * 10^3$	8600 - 12000	$5 * 10^3 - 45 * 10^3$
Electrostatic propulsion	Gridded ion thruster (GIE)	NSTAR [18]	2,3	3300	92
	Field emission electric propulsion (FEEP)	LISA [19]	0,0015	>4000	0,015

1.2 State of the art of the electric propulsion systems

The first in orbit experiments on electric propulsion were made at the second half of the 1900 with the first test of an electric thruster that was made the 20th July 1964 on the SERT-1 (Space Electric Rocket Test 1) a NASA mission to test electrostatic ion thruster, with successive tests performed by the Russia in the mission Voskhod 1 with the test of an ion engine and in the mission Zond 2 with the tests of pulsed plasma thrusters during the Cold War. Studies and successive projects are continued towards the end of the 1900, with a strong interest in developing this technology that was

dedicated also in the last decades. Electric propulsion is considered a young technology with respect to the more traditional liquid and solid propulsion, due to its recent conceptualization and prototypatization. Nuclear propulsion based on fission or on fusion reactions are technologies on which it is studying nowadays for designing new space vehicles for interplanetary flights. In comparison with the traditional propulsion, electric propulsion and nuclear propulsion are characterized by higher specific impulse and lower thrust, suitable therefore for interplanetary missions being capable to operate for their low thrust only when they are already in orbit, with their performances reported in Table 1.1. Among the electric thrusters, the engines more employed in space missions are the hall effect thrusters, that have been studied from the 1950-1960 and they have been mounted on the lunar mission SMART-1 (launched in the 27th September 2003) and they are employed nowadays for the stabilization of the satellites in orbit. Different companies that provide space services do the production and the commercialization of hall effect thrusters (Sitael, ThrustMe) that are nowadays among the main electric thrusters integrated in space missions. Another type of electric thrusters that have the same specific impulse level and thrust level of the hall effect thrusters are the gridded ion engines, that as the hall effect thrusters were employed with success in various space missions and they have an acceleration mechanism of the charged particles simple and reliable, based on accelerations grids charged at a precise voltage. Electric thruster mentioned up to now have the disadvantage of being constituted by electrodes that degrade in time, limiting the functionalities and the operative life of the thruster itself, therefore new concepts of electric thrusters have been proposed, such as the helicon thruster that is one of the thrusters studied in this PhD thesis. The helicon thruster is an innovative thruster because it does not have electrodes for the plasma generation, but a helicon antenna and it has performance level comparable to the ones of the hall effect thruster and of the gridded ion engine, even if the helicon thruster has a very low propulsive efficiency as computed in this research. All these thrusters have feeding powers of the order of kiloWatts and low thrust of the order of milliNewtons; with the magnetoplasmadynamic thrusters and the VASIMR thruster [16] instead the thrust levels are higher with higher feeding powers of the thrusters, of the order of a fraction of MegaWatts, but these are thrusters that have not already flown in a space mission. Nuclear thrusters are instead a technology still in conceptualization and design phase [17], both fission nuclear thrusters and fusion nuclear thrusters. Many are the projects proposed up to now, from the first NASA Nuclear Thermal Propulsion (NTP) project based on a fission reactor (the NERVA project) up to the more recent DRACO (Table 1.1) project, while for the fusion nuclear thrusters it can be mentioned the Princeton Field Reversed Configuration (PFRC) (Table 1.1) that would apply the experimental results of a stable magnetically confined fusion plasma to a Direct Fusion Drive [17] concept that can use the field reversed configuration to feed and to propel a spacecraft for interplanetary mission. These are all of particular interest for the high specific impulse and the high thrust obtainable from this category of thrusters with respect to the other electric thrusters. The nuclear fusion thruster conceptualization and design is treated in this PhD thesis and its performance capability are demonstrated.

1.3 PhD project: objectives and obtained results

The PhD project of the XXXVII cycle of the PhD course in Energy and Environment, with the title "plasma thrusters design for sustainable space transportation" is a research project that started

from the studies on the PROTO-SPHERA experiment of the ENEA Research Center of Frascati that had as main objective to study the transformation of the PROTO-SPHERA experiment from a plasma physics experiment to a nuclear fusion thruster. The study has been conducted both on electric propulsion and on nuclear fusion propulsion and it resulted in two main projects on plasma propulsion: the design of a helicon thruster and the design of a nuclear fusion thruster. The first project, the one based on the helicon technology is of easier realization, requiring technologies already tested in laboratory and that have already demonstrated their functionalities, and the research and the work made within the PhD project will allow to test in the ENEA laboratory a prototype of a helicon plasma thruster. The second project on the nuclear fusion thruster based on the PROTO-SPHERA experiment is a more complex project that requires the design of a nuclear fusion reactor that can be integrated inside a space thruster for interplanetary flight, it starts from the current configuration of the PROTO-SPHERA experiment and as a nuclear fusion thruster design it has the advantage to be based on an already existing experiment. The research made within the PhD project studied the design of both plasma thrusters. For the helicon thruster it is arrived to the conceptualization of a design method that is based on analytical formulas and numerical simulations for the sizing and the performance analysis of the main propulsive components. The design method of the helicon thruster is based on fundamental equations of space propulsion and of plasma physics to which it has been added an extensive study on the helicon waves and on the helicon antennas literature, with which analytical and numerical models have been used for sizing the helicon antennas that have been validated with electromagnetic simulations. In addition, simulations have been performed of the magnetic field topology for the plasma confinement magnetostatic field and Particle In Cell (PIC) simulations of the plasma acceleration in the magnetic nozzle, to estimate the propulsive performance of the helicon thruster. On the project of the nuclear fusion thruster based on the PROTO-SPHERA experiment, instead, there have been made studies on the magnetic configuration of the PROTO-SPHERA experiment, with simulations of the plasma magnetohydrodynamic equilibrium (MHD equilibrium) obtained with a code (LIBRA) developed for this purpose with objective the computation of the plasma ideal magnetohydrodynamic equilibrium inside the magnetic configuration. The MHD simulation code has been validated comparing the obtained solutions with some reference solutions as the analytical Solov'ev solution for the plasma magnetohydrodynamic equilibrium, and also the magnetostatic equilibrium solution and the magnetohydrodynamic equilibrium solution of the DTT tokamak in phase of construction in the ENEA Research Center of Frascati. The extension of the NUCLEUS code [20] to the fusion regime of the PROTO-SPHERA experiment is a further computation that has been performed within the PhD project in which it has been studied the functionality of the PROTO-SPHERA experiment as a nuclear fusion reactor and from the power of the fusion products it is estimated the propulsive performance of the system as a nuclear fusion thruster. Both the studies were and are subject of scientific publications that have been presented at international conference and published on scientific journal.

In the next chapters are presented the main studies made in this PhD thesis, starting in Chapter 2 from the physical models that are at the basis of the plasma propulsion modeling with a particular focus on the physics of the magnetohydrodynamic equilibrium and on the helicon waves in plasma. In the successive chapters are reported the main results obtained in the study of the plasma thrusters on which it is focused the research work, in Chapter 3 the HELICARGO project

is introduced from which started the research on the helicon thruster. The main models developed for the design of the helicon thruster main components are presented, along with simulations of the entire helicon thruster. Chapter 4 is dedicated to the nuclear fusion thruster based on the PROTO-SPHERA experiment and in the various sections are described the studies used to model it such as: the mission analysis for the interplanetary transfer of the propulsion system, the computation of the fusion magnetohydrodynamic equilibrium and the evaluation of the propulsive performance. Finally the conclusions are presented in Chapter 5.

Chapter 2

Plasma propulsion physics

2.1 Plasma magnetohydrodynamic description

The plasma magnetohydrodynamic description is based on the assumption that it is a conductive fluid for which the fluid equations, the Ohm law and the Maxwell equations are valid. With this approach is possible to describe the variation in time and in space of the plasma quantities, putting in a system the fluid conservation equations (conservation of mass, conservation of momentum and conservation of energy), the Ohm law for a perfectly conductive fluid ($\sigma \to \infty$) and the Maxwell equations, obtaining the following system of equations [21]:

$$\begin{cases} \frac{\partial \rho}{\partial t} + \nabla \cdot (\rho \vec{v}) = 0 \\ \rho \frac{\partial \vec{v}}{\partial t} + \rho(\vec{v} \cdot \nabla)\vec{v} = \vec{J} \times \vec{B} - \nabla p \\ \frac{d}{dt}(\frac{p}{\rho^{\gamma}}) = 0 \\ \vec{E} + \vec{v} \times \vec{B} = 0 \\ \nabla \times \vec{E} = -\frac{\partial \vec{B}}{\partial t} \\ \nabla \times \vec{B} = \mu_0 \vec{J} \\ \nabla \cdot \vec{B} = 0 \end{cases} \tag{2.1}$$

where the conservation of mass implies that the total number of particles in the volume is conserved, neglecting ionization, recombination, charge exchange and emission of charged particles. The conservation of momentum corresponds to the one of a fluid on which three forces act: the inertial force, the magnetic force and the pressure gradient, the conservation of energy states that in absence of dissipative phenomena the entropy of the system is conserved. The Ohm's law states that for a perfectly conductive fluid the electric field is perfectly balanced from the Lorentz force for unit of charge, the Faraday law states that at a space variation of the electric field corresponds a time variation of the magnetic field, the IV Ampère-Maxwell equation states that the circuitry of the magnetic field on a closed surface is equal to the total net current that flows in it and the II Maxwell equation states that the magnetic field lines are curved closed lines [21]. In the complete system of the MHD equations that include the dynamic $\vec{E}$ is the vector electric field, $\vec{B}$ is the vector magnetic field, $\vec{v}$ is the fluid plasma velocity, ρ is the density of the plasma fluid, $\vec{J}$ is the plasma current density vector, p is the plasma pressure and $\gamma = 5/3$ [21] is equal to the specific heats ratio. This system of equations can be written for each specie (ions and electrons) that are in the plasma,

but combining the equations of ions and electrons it can be obtained a single system of equations that describes the plasma dynamic. Starting from the complete MHD equations, that include the dynamic, it can be made the approximation of a single fluid, obtaining the complete MHD equations for a single fluid. Assuming that the electronic mass is negligible $m_e \to 0$ and that the plasma is quasi-neutral $n_i = n_e = n$, it can be defined a mass density starting from the number density, that is the ion mass density and it is defined as:

$$\rho = m_i n \tag{2.2}$$

In the same way for the conservation of momentum it can be stated that the fluid momentum is transported from the ions for their higher mass, therefore the fluid velocity is defined as the ion velocity:

$$\vec{v} = \vec{u}_i \tag{2.3}$$

The current density is instead defined from the difference in velocity between ions and electrons:

$$\vec{J} = en(\vec{u}_i - \vec{u}_e) \tag{2.4}$$

$$\vec{u}_e = \vec{v} - \frac{\vec{J}}{en} \tag{2.5}$$

The last definitions required are the ones of the total pressure and of the total temperature:

$$p = p_i + p_e = 2nT \tag{2.6}$$

$$T = \frac{(T_i + T_e)}{2} \tag{2.7}$$

In this way the variables of the complete MHD system of equations for a single fluid are defined: ρ, $\vec{v}$, $\vec{J}$, p, T, as function of the variables for the two fluid system of equations: n, $\vec{u}_i$, $\vec{u}_e$, p_i, p_e, T_i, T_e [21]. In the following treatment the MHD system of equations for a single fluid are considered. In ideal equilibrium condition, that is of plasma fluid velocity equal to zero and of the time derivatives equal to zero, the magnetohydrodynamic ideal equilibrium equations are obtained, that are the following:

$$\begin{cases} \nabla p = \vec{J} \times \vec{B} \\ \nabla \times \vec{B} = \mu_0 \vec{J} \\ \nabla \cdot \vec{B} = 0 \end{cases} \tag{2.8}$$

It can be noted that, while the complete MHD equations that include the dynamics are valid for times comparable to the MHD characteristic times, the equilibrium equations are valid on transport

longer time scale. This is because for static systems or that move very slowly, the problems of $E_{\parallel}$, of the collisions and of the viscosity are negligible or they are deleted when the ion and electron momentum equations are summed to obtain the momentum equation for a single fluid. MHD equilibrium purely static are simpler to study, they don't have big mathematical complexities as the dynamic equilibiums and they provide useful descriptions of the magnetic configurations. The aim of the MHD equilibrium theory is to discover the magnetic geometries that confine and isolate hot plasmas from material walls and that are macroscopically stables with β values (where β is the plasma pressure/magnetic pressure) sufficiently high to be attractive as potential fusion reactors [21]. These equations allow to describe the equilibrium distribution that a plasma can reach inside of a magnetic field, as function of the magnetic field distribution $\vec{B}$, of the current density $\vec{J}$ and of the plasma pressure p. The result of the magnetohydrodynamic ideal equilibrium is that the plasma inside of a magnetic configuration reaches an equilibrium distribution in which the magnetic surfaces and the current surfaces are isobaric surfaces.

2.2 Plasma magnetic confinement and orbital theory

The equation that describes the motion of a charged particle with charge q and velocity $\vec{v}$, in presence of an electric field $\vec{E}$ and a magnetic field $\vec{B}$ is [22]:

$$m\frac{d\vec{v}}{dt} = q\vec{E} + q\vec{v} \times \vec{B} \tag{2.9}$$

where $d\vec{v}/dt$ is the particle acceleration and the right side of the equation is the total force acting on the charged particle and it is given from the sum of the electric force (Coulomb force) and of the magnetic force (Lorentz force). From this dynamic equation it can be derived the motion of a charged particle immersed in a electro-magnetic field. Let us assume that $\vec{E} = 0$ and $\vec{B} = B\hat{z} = constant$. The previous equation becomes then:

$$\frac{d\vec{v}}{dt} = \omega_c \vec{v} \times \hat{z} \tag{2.10}$$

with $\omega_c = (qB)/m$ that is the cyclotron angular frequency of the charged particle. Multiplying scalarly the previous equation for $\vec{v}$, it is obtained the following equation:

$$\vec{v} \cdot (m\frac{d\vec{v}}{dt}) = \frac{1}{2}m\frac{d(v^2)}{dt} = \vec{v} \cdot (q\vec{v} \times \vec{B}) = 0 \tag{2.11}$$

therefore $v = constant$ and $W = (1/2)mv^2 = constant$, that is the total velocity and the total kinetic energy are conserved in a uniform magnetic field. Multiplying scalarly the dynamic equation for $\hat{z}$, it is obtained the following expression:

$$m\frac{d\vec{v}}{dt} \cdot \hat{z} = m\frac{d(v\hat{z})}{dt} = m\frac{dv_{\parallel}}{dt} = \hat{z} \cdot (q\vec{v} \times B\hat{z}) = 0 \tag{2.12}$$

therefore $v_{\parallel} = constant$ and $W_{\parallel} = (1/2)mv_{\parallel}^2 = constant$, that is the component of the velocity vector parallel to the magnetic field lines and the kinetic energy of the charged particle parallel to the magnetic field lines are constant. From this it is derived that if the total kinetic energy and the parallel kinetic energy are conserved, also the perpendicular kinetic energy is conserved.

Taking the dynamic equation:

$$\frac{d\vec{v}}{dt} = \omega_c \vec{v} \times \hat{z} \tag{2.13}$$

and solving the vector product in a cartesian reference system $(\hat{x}, \hat{y}, \hat{z})$, the components of the dynamic equation in the cartesian reference system are the following:

$$\begin{cases} \dot{v}_x = \omega_c v_y \\ \dot{v}_y = -\omega_c v_x \\ \dot{v}_z = 0 \end{cases} \tag{2.14}$$

Deriving with respect to time the first equation, therefore obtaining the derivative of the acceleration along x and substituting the second equation in the first equation derived, it is obtained an ordinary differential equation of the second order. In an analogous way it can be derived the second equation with respect to time and substituting the first equation in the second derived, the following equations are obtained:

$$\ddot{v}_x + \omega_c^2 v_x = 0 \qquad\qquad \ddot{v}_y + \omega_c^2 v_y = 0 \tag{2.15}$$

these ordinary differential equations of the second order are the equations of an harmonic oscillator, that oscillates at an angular frequency ω_c and that has as solution the harmonic functions sine and cosine. From the integration of the differential equations one obtains the components of the velocity vector for the charged particle in the cartesian reference system:

$$\begin{cases} v_x = v_\perp \cos(\omega_c t + \phi) \\ v_y = -v_\perp \sin(\omega_c t + \phi) \\ v_z = v_{z0} = v_\parallel = constant \end{cases} \tag{2.16}$$

Integrating further the equations of the velocity vector components of the charged particle with respect to time, the trajectory equations of the charged particle immersed in a uniform magnetic field are obtained, that are the following:

$$\begin{cases} x - x_0 = \frac{v_\perp}{\omega_c} \sin(\omega_c t + \phi) \\ y - y_0 = \frac{v_\perp}{\omega_c} \cos(\omega_c t + \phi) \\ z - z_0 = v_\parallel t \end{cases} \tag{2.17}$$

where $v_\perp^2 = v_{x0}^2 + v_{y0}^2$ and $\phi = \arccos(v_{x0}/v_\perp)$ are constants of the motion and they are determined from the initial value of the velocity vector. The quantity $\rho = v_\perp/\omega_c$ is called the Larmor radius and with this definition the trajectory equations of the charged particle in the cartesian reference system can be written as:

$$\begin{cases} x - x_0 = \rho \sin(\omega_c t + \phi) \\ y - y_0 = \rho \cos(\omega_c t + \phi) \\ z - z_0 = v_{\parallel} t \end{cases} \tag{2.18}$$

From the trajectory equations of the charged particle it can be seen that the motion of a charged particle in a constant axial magnetic field is a spiral motion around the magnetic field line, therefore it is a combination of a uniform circular motion around the magnetic field line with constant radius ρ, that is called Larmor rotation and being a uniform circular motion it is a motion with constant rotational velocity, the other motion of which it is composed the motion of a charged particle in a uniform axial magnetic field is a translational motion along the magnetic field line with constant velocity $v_{z0} = v_{\parallel}$. From the definition of the Larmor radius ρ it is evident that the higher is the cyclotron angular frequency ω_c, that increases at increasing of the intensity of the magnetic field, the lower is the Larmor radius of the charged particle orbiting around the magnetic field lines and the more are confined the charged particles from the magnetic field.

2.3 Waves in plasmas and use of helicon waves

Waves in plasmas can propagate when external excitations prime perturbations in the plasma that induce the propagation of plasma oscillation modes, with the subsequent formation of wave electric and magnetic fields in the plasma. The plasma is a conductive medium that can be described from its own electric permittivity, that defines its conductive properties. As for all the transmitting medium, the waves propagation in plasmas can be described from the Maxwell equations for the electric and magnetic field, in which it is considered indeed the electric permittivity of the medium in which the waves propagate, that in this case is the plasma. Maxwell equations in the frequency domain on which it is based the waves propagation in the plasma are the following [23, 24]:

$$\begin{cases} \nabla \cdot \vec{B} = 0 \\ \nabla \times \vec{E} = i\omega \vec{B} \\ \nabla \times \vec{B} = \mu_0 (\vec{J} - i\omega \varepsilon_0 \vec{E}) \end{cases} \tag{2.19}$$

where $\vec{E}$ and $\vec{B}$ are the wave electric field and the wave magnetic field, ω is the excitation angular frequency of the waves in the plasma, ε is the plasma permittivity assigned in tensorial form, while ε_0 and μ_0 are respectively the vacuum electric permittivity and the vacuum magnetic permeability. To this equation it must be added a further equation to describe the state and the dynamic of the plasma, that is the momentum conservation equation. Now supposing that the plasma dynamic can be described from the electrons motion, being the ions characterized from an higher inertia and a lower velocity, supposing also that the plasma is confined in an axial magnetostatic field $\vec{B_0}$, that it is at a density n_{e0} and that the electronic fluid in its motion can collide with ions and neutrals, with collisions that act as a drag to the electron motion, the momentum conservation equation for the electronic fluid in the frequency domain is the following:

$$-i\omega m_e \vec{v} = -e(\vec{E} + \vec{v} \times \vec{B_0}) - m_e \nu \vec{v} \tag{2.20}$$

that can be rewritten making explicit the electric field $\vec{E}$ in the following way:

$$\vec{E} = -\frac{B_0}{en_{e0}}(i\delta\vec{J} + \hat{z} \times \vec{J}) \tag{2.21}$$

where e is the electronic charge, $\vec{J}$ is the plasma current density and the δ parameter is defined as:

$$\delta = \frac{\omega + i\nu}{\omega_c} \tag{2.22}$$

with ν the plasma total collisional frequency, given from the sum of the collisional frequencies between electrons and ions and electrons and neutrals and ω_c the cyclotron angular frequency. For the collisional frequencies between electrons and ions and between electrons and neutrals, the following expressions are considered:

$$\nu_{ei} = 3.9 \cdot 10^{-6} n_i Z_i^2 \frac{ln\Lambda}{T_{e0}^{\frac{3}{2}}} \tag{2.23}$$

$$\nu_{en} = \sigma_n n_n v_{th,e} \tag{2.24}$$

where Z_i is the ionization charge number, $ln\Lambda$ is the Coulomb logarithm, σ_n is the neutral atom cross section and $v_{th,e} = \sqrt{2T_{e0}/m_e}$ is the electronic thermal velocity, with all the unit of measure of the quantities expressed in the international reference system. Considering for the study of the waves in plasmas both the Maxwell equations and the momentum conservation equation for the electronic fluid, the following system of equations is obtained:

$$\begin{cases} \nabla \cdot \vec{B} = 0 \\ \nabla \times \vec{E} = i\omega\vec{B} \\ \nabla \times \vec{B} = \mu_0(\vec{J} - i\omega\varepsilon_0\vec{E}) = -i\omega\varepsilon_0\varepsilon\vec{E} \\ -i\omega m_e\vec{v} = -e(\vec{E} + \vec{v} \times \vec{B_0}) - m_e\nu\vec{v} \end{cases} \tag{2.25}$$

Solving the system of equations 2.25 combining the four equations of the system, one obtains a vector differential equation of the second order, that is:

$$\delta\nabla \times \nabla \times \vec{B} - k\nabla \times \vec{B} + k_w^2\vec{B} = 0 \tag{2.26}$$

where k is the parallel wave number, k_w is the whistler wave number defined as $k_w = k_s\sqrt{\delta}$ with $k_s = \omega_p/c$ ("skin number"). Assuming that the solution of the differential equation is such that the rotor of the wave magnetic field is parallel to the wave magnetic field itself by means of the total wave number β, that is $\nabla \times \vec{B} = \beta\vec{B}$, the differential equation 2.26 can be factorized as follow, resulting in an algebraic equation of the second order:

$$(\beta_1 - \nabla\times)(\beta_2 - \nabla\times)\vec{B} = 0 \tag{2.27}$$

$$\delta\beta^2 - k\beta + k_w^2 = 0 \tag{2.28}$$

A particular solution of this algebraic equation of the second order is obtained if the electronic mass is neglected ($m_e = 0$), that implies that $\delta = 0$ and the solution is only a complex β that is the helicon wave number for a collisional uniform plasma:

$$\beta = \frac{(\omega + i\nu)}{k}\frac{n_{e0}e\mu_0}{B_0} \tag{2.29}$$

If no additional hypotesis is made, the algebraic equation of the second order 2.28 has two different roots that are:

$$\beta_{1,2} = \frac{k \mp \sqrt{k^2 - 4\delta k_w^2}}{2\delta} \tag{2.30}$$

These roots are well separated if $k^2 >> \delta k_w^2$ and with this hypothesis it can be considered the Taylor series expansion at the first order for the polynomial $(1 + x)^\alpha = 1 + \alpha x$, and the roots can be approximated as follow:

$$\beta_1 = \frac{k_w^2}{k} \qquad\qquad \beta_2 = \frac{k}{\delta} \tag{2.31}$$

The first solution is the helicon wave number, obtained also when the electron mass is neglected, while the other is a cyclotron wave strongly damped (i.e. the Trivelpiece-Gould wave, TG wave). These two waves are both propagating in the plasma when the electron inertia is considered in the model and they are coupled at the boundary (for a constant density profile) or in the plasma region (for a radially varying plasma profile). TG waves have typically lower amplitudes in the plasma region, but their amplitude is higher at the plasma boundary where they strongly contribute to the absorption of the wave energy in the plasma.
Helicon waves in magnetized plasmas can be excited with helicon antennas, simple antennas of cylindrical geometry discovered by Boswell in the 1970 [6, 25] that are capable to produce uniform plasma, with low temperature (few eV) and high density (electron density up to $10^{20} particles/m^3$). The helicon waves for such capability have been deeply studied in the successive decades, with studies on the helicon wave theory and the design of the helicon antennas [23, 24, 26, 27] that have been at the basis of the plasma RF sources design for high frequency industrial application [27] and of new plasma space thrusters that have as main component for the plasma generation the helicon antenna: the innovative helicon thrusters without electrodes [7, 28–31].

2.4 Plasma acceleration in a magnetic field

Charged particles that are immersed in a magnetic field, as described in section 2.2 are subjected to a magnetic force called Lorentz force that bounds particles to move along the magnetic field lines and to spiral around them. By definition the Lorentz force is a force perpendicular to the velocity vector (equation 2.9), therefore it is a force that does no work on the charged particles. For the kinetic energy theorem in absence of dissipation and of external forces that make work, the energy of the system is conserved and therefore the particles contained in the plasma conserve their kinetic energy in their motion within the magnetic field. The kinetic energy theorem is one of the principles

on which it is based the plasma acceleration in a magnetic field. Moreover in a magnetic field that does not vary rapidly, it can be assumed that the magnetic moment, defined as the ratio between the perpendicular kinetic energy of the particle and the magnetic field ($\mu = \frac{K_\perp}{B}$) is a constant quantity [32] inside the magnetic field that is also defined as adiabatic invariant. A plasma acceleration model in a magnetic field can be derived putting in a system the kinetic energy conservation equation and the constancy of the magnetic moment [33], obtaining the following system:

$$\begin{cases} K = constant \\ \mu = constant \end{cases} \tag{2.32}$$

Assuming to take two different sections called with the subscripts $_0$ and $_1$, where the first is an inlet section and the second is an exit section, the constancy of the previous relations can be written as:

$$\begin{cases} \frac{1}{2}mv_{\perp_0}^2 + \frac{1}{2}mv_{\parallel_0}^2 = \frac{1}{2}mv_{\perp_1}^2 + \frac{1}{2}mv_{\parallel_1}^2 \\ \frac{W_{\perp_0}}{B_0} = \frac{W_{\perp_1}}{B_1} \end{cases} \tag{2.33}$$

where with the subscripts $_\perp$ and $_\parallel$ are indicated the perpendicular and the parallel direction respectively. Let's compute now the parallel velocity in the exit section $v_{\parallel_1}$ to compute how a charged particle can be accelerated in a magnetic field, the expression is the following:

$$v_{\parallel_1} = \sqrt{v_{\parallel_0}^2 + v_{\perp_0}^2(1 - \frac{B_1}{B_0})} \tag{2.34}$$

The parallel velocity of the charged particle in the exit section will be as high as higher is the axial velocity and the perpendicular velocity in the inlet section and as lower is the ratio B_1/B_0, therefore as lower is the ratio between the magnetic field at the exit section and the magnetic field at the inlet section [33]. To accelerate a charged particle is therefore necessary a gradient of the magnetic field decreasing in the acceleration direction of the charged particle.
This theory finds important applications in the plasma propulsion because from the "Debye sheath" [34], that is the transition region between the plasma and the solid wall therefore the external boundary of the plasma, it has been demonstrated that when a charged particle exits from the plasma region, for example to be accelerated, for the Bohm criterion [34] this has a velocity at least sonic, that in agreement to the previous equation 2.34 corresponds to the inlet velocity of the charged particle $v_{\parallel_0}$. In agreement with this model therefore, a device that can emit charged particles and drive them towards a region with a decreasing magnetic field (a region with a magnetic field gradient), that is a magnetic nozzle, can accelerate the charged particles from sound speed to supersonic speed and it can work as a plasma thruster.

2.5 Equilibrium theory of the screw-pinch

The screw-pinch is a plasma equilibrium magnetic configuration of cylindrical geometry obtained from a plasma column generated between two electrodes that produces an azimuthal magnetic field, to which it is superimposed an axial magnetic field generated from external poloidal coils that is necessary to stabilize the magnetic configuration. The equilibrium magnetic configuration

resulting from the plasma confinement is an axisymmetric configuration with axial and azimuthal field components. The equilibrium equation in radial direction of the screw-pinch, that is the subject in this PhD thesis, is computed from the ideal MHD equilibrium equations system:

$$\begin{cases} \nabla \times \vec{B} = \mu_0 \vec{J} \\ \nabla p = \vec{J} \times \vec{B} + \vec{f_c} \end{cases} \tag{2.35}$$

where to the external Lorentz force it has been added the centrifugal force ($\vec{f_c}$) that acts on the plasma due to its rotation around the symmetry axis. Assuming a cylindrical reference system $(\hat{r}, \hat{\theta}, \hat{z})$, the current density vector and the magnetic field vector have the following components for a screw-pinch: $\vec{J} = (0, J_\theta, J_z)$ with J_z that is the source term and $\vec{B} = (0, B_\theta, B_z)$, while the pressure gradient ∇p and the centrifugal force $\vec{f_c}$ have only radial component. Now taking the IV Ampère-Maxwell equation, assuming an axisymmetric geometry ($\frac{\partial}{\partial \theta} = 0$), the magnetic field components with the current density components can be related with the following expressions:

$$J_z(r) = \frac{1}{\mu_0 r} \frac{d(B_\theta r)}{dr} \tag{2.36}$$

$$J_\theta(r) = -\frac{1}{\mu_0} \frac{dB_z}{dr} \tag{2.37}$$

Substituting these expressions of the current density vector components in the radial equilibrium equation of the screw-pinch:

$$\frac{dp}{dr} = J_\theta B_z - B_\theta J_z + f_c(r) \tag{2.38}$$

the following radial equilibrium equation of the screw-pinch is obtained, which can be written as function of the magnetic field vector components, of the pressure gradient and of the centrifugal force:

$$\frac{d}{dr}\left(\frac{B_z^2}{2\mu_0}\right) = -\frac{d}{dr}\left(p + \frac{B_\theta^2}{2\mu_0}\right) - \frac{B_\theta^2}{\mu_0 r} + f_c(r) = G(r) \tag{2.39}$$

A parameter to evaluate the stability of a 2D axisymmetric magnetic configuration as the tokamak one is the safety factor $\hat{q}$, that is defined from the rotational transform ι, that is the angle that a magnetic field line describes on a fixed poloidal plane after making a toroidal revolution, in agreement with the following relation [21]:

$$\hat{q} = \frac{2\pi}{\iota} = \frac{r B_t}{R B_p} \tag{2.40}$$

where in the last expression it has been approximated the torus with a cylinder and r, R, B_t e B_p are respectively the minor radius, the major radius, the toroidal magnetic field and the poloidal magnetic field of the torus. The safety factor is a qualitative indicator of the stability and a high $\hat{q}$ is indicative of a good stability for the magnetic configuration. The pinch is subjected to instabilities due to inhomogeneities in the plasma distribution that can affect and destroy the magnetic configuration, one of the major is the "kink instability" for which it is defined an appropriate safety factor:

$$\hat{q}_{kink} = \frac{aB_t}{R_0 B_p} \tag{2.41}$$

where B_t and B_p are the magnetic field components defined previously, a is the torus minor radius and R_0 is the torus major radius. Assuming that the torus can be opened and stretched to form a cylinder that is the screw-pinch, it can be assumed that a is the cylinder radius and the torus major radius R_0 is in relation with the height of the cylinder l (that equates the torus circumference) from the following formula: $R_0 = l/(2\pi)$, from which therefore it can be obtained the definition of the safety factor for the kink instability of the screw-pinch:

$$\hat{q}_{kink_{S-P}} = \frac{2\pi a B_t}{l B_p} \tag{2.42}$$

The efficiency of a magnetic confinement reactor can be quantitatively estimated from the non-dimensional pressure β that is given from the ratio between the plasma pressure and the magnetic pressure:

$$\beta = \frac{< p >}{B^2/(2\mu_0)} \tag{2.43}$$

where $< p >$ is the volume average value of the plasma pressure. In a screw-pinch the Bennet relation defines what is the link between the plasma temperature and the axial pinch current, and it is the following [22]:

$$N k_B (T_e + T_i) = \frac{\mu_0}{8\pi} \beta_p I^2 \tag{2.44}$$

where N is the electron linear density computed along the plasma column, that is the number of electrons per unit of length of the plasma column, k_B is the Boltzmann constant, I is the plasma axial current and β_p is the poloidal β computed on a poloidal section of the screw-pinch that is a section perpendicular to the simmetry axis, and it is defined as [21]:

$$\beta_p = \frac{< p >}{\frac{B_\theta^2}{2\mu_0}} \tag{2.45}$$

where B_θ is the azimuthal magnetic field. The Bennet relation for the screw-pinch states that the plasma temperature in a screw-pinch is directly proportional to the β_p and to the square of the plasma axial current and therefore to maximize the plasma temperature it can be increased the axial current or the poloidal β_p. The poloidal β_p is defined with respect to the magnetic field components as:

$$\beta_p = 1 + \frac{B_z^2(a) - B_z^2}{B_\theta^2(a)} \tag{2.46}$$

and from this definition three cases can be distinguished:

- $\beta_p = 1$ if $B_z = B_z(a)$
- $\beta_p < 1$ if $B_z(0) > B_z > B_z(a)$ when B_z is maximum at the center and it is called "paramagnetism" in the plasma (as it happens in the screw-pinch)

- $\beta_p > 1$ if $B_z(0) < B_z < B_z(a)$ when B_z is minimum at the center and it is called "diamagnetism" in the plasma (as it happens in the tokamak).

A maximum limit to the β value reachable from a magnetic configuration is given from the ballooning mode, an explosive instability of the plasma of higher order with respect to the kink instability that can lead to the disruption of the magnetic configuration. The maximum value that can reach β in a toroidal magnetic configuration is given from the Troyon limit that has the following expression:

$$\beta_{max} = \beta_N \frac{I}{aB_0} \tag{2.47}$$

where β_N is the normalized β and its limit is computed as 2.8% from numerical simulations considering a big number of MHD instabilities, I is the plasma current in Mega Ampere, B_0 is the external magnetic field and a is the plasma radius. In magnetic configuration with a high toroidal magnetic field and a high aspect ratio R/a, reactors have typically $\beta \approx 5\% - 10\%$ values that have been reached experimentally, while more compact magnetic configuration with aspect ratio close to 1 can reach higher values $\beta \approx 30\% - 40\%$, also this reached experimentally but not for a higher plasma pressure, but for a lower magnetic field [3, 21].

2.6 Plasma magnetohydrodynamic equilibrium (Grad-Shafranov equation)

The Grad-Shafranov equation is a differential equation that describes the magnetohydrodynamic equilibrium of a plasma that is magnetically confined inside a magnetic field. The equilibrium equation from which it is derived the Grad-Shafranov equation is the momentum conservation equation for a plasma fluid [22]:

$$\rho \frac{\partial \vec{v}}{\partial t} + \rho(\vec{v} \cdot \nabla)\vec{v} = \vec{J} \times \vec{B} - \nabla p \tag{2.48}$$

where on the right side of the equation there is the magnetic force and the pressure force, and in the hypothesis of stationary fluid and of static equilibrium the plasma equilibrium magnetohydrodynamic equation becomes the following:

$$\vec{J} \times \vec{B} = \nabla p \tag{2.49}$$

and this equation states that when a plasma is confined in a closed magnetic geometry the Lorentz force on the left side is perfectly balanced from the pressure gradient, that is also known as MHD equilibrium equation. The equilibrium equation 2.49 states that the pressure gradient, being obtained from the vector product between the plasma current density vector $\vec{J}$ and the magnetic field vector $\vec{B}$, is always perpendicular to the plasma current density and to the magnetic field vector, therefore the following relation is valid:

$$\vec{B} \cdot \nabla p = 0 \tag{2.50}$$

that implies that the magnetic field lines stay on surfaces (magnetic surfaces) that are per-

pendicular to the pressure gradient and therefore the magnetic surfaces are surfaces with constant pressure (isobaric surfaces). Moreover another relation derived from the plasma magnetohydrodynamic equilibrium equation is the following:

$$\vec{J} \cdot \nabla p = 0 \tag{2.51}$$

this equation implies that the current lines stay on surfaces (current surfaces) perpendicular to the pressure gradient and also these are surfaces with constant pressure. The plasma magnetohydrodynamic equilibrium equation states therefore that a plasma, in static equilibrium, confined with a magnetic field is distributed on magnetic surfaces and current surfaces that have constant pressure.
The Grad-Shafranov equation is determined from the plasma magnetohydrodynamic equilibrium equation and it is nothing else that the same equilibrium equation rewritten as function of the variable Ψ, the poloidal flux function that is proportional to the poloidal flux of each magnetic surface and it is defined as:

$$\Psi = \int \vec{B} dA \tag{2.52}$$

where dA is the infinitesimal poloidal section of the magnetic configuration. The poloidal section of the geometry is a section of a toroidal reference system $(\hat{r}, \hat{\phi}, \hat{z})$ that lies on a plane passing through the symmetry axis. By definition the poloidal flux function is a constant associated to a determined poloidal section, therefore the poloidal flux function is a constant on each magnetic surface and therefore on each current surface. It is valid therefore the relation:

$$\vec{B} \cdot \nabla \Psi = 0 \tag{2.53}$$

that is that the magnetic surfaces are surfaces perpendicular to the gradient of the poloidal flux function and they are therefore equipsi surfaces.
Let's find now a relation between the magnetic field vector and the variable Ψ, to do so let's take a toroidal reference system $(\hat{r}, \hat{\phi}, \hat{z})$ and in a given section the magnetic field vector can be written as:

$$\vec{B} = B_r i_r + B_\phi i_\phi + B_z i_z \tag{2.54}$$

From the first Maxwell equation for the magnetic field $\nabla \cdot \vec{B} = 0$ it is known that the magnetic field is a vector field with zero divergence, therefore it is always possible to define the magnetic field vector $\vec{B}$ as function of a magnetic field potential $\vec{A}$ in agreement to the following relation:

$$\vec{B} = \nabla \times \vec{A} \tag{2.55}$$

that satisfies always the first Maxwell equation, because the divergence of a rotor is always equal to zero:

$$\nabla \cdot \vec{B} = \nabla \cdot (\nabla \times \vec{A}) = 0 \tag{2.56}$$

In agreement to the definition given for the magnetic field vector as function of the magnetic potential vector, the magnetic field vector in a toroidal reference system can be written as:

$$\vec{B} = \nabla \times \vec{A} = (\frac{1}{r}\frac{\partial A_z}{\partial \phi} - \frac{\partial A_\phi}{\partial z})i_r + (\frac{\partial A_r}{\partial z} - \frac{\partial A_z}{\partial r})i_\phi + (\frac{1}{r}\frac{\partial}{\partial r}(rA_\phi) - \frac{1}{r}\frac{\partial A_r}{\partial \phi})i_z \tag{2.57}$$

where the rotor operator is expressed in a cylindrical reference system. Assuming now axial simmetry ($\frac{\partial}{\partial \phi} = 0$) of the magnetic configuration, the magnetic field vector components in a toroidal reference system as function of the magnetic potential vector become the following:

$$B_r = -\frac{\partial A_\phi}{\partial z} \tag{2.58}$$

$$B_\phi = \frac{\partial A_r}{\partial z} - \frac{\partial A_z}{\partial r} \tag{2.59}$$

$$B_z = \frac{1}{r}\frac{\partial}{\partial r}(rA_\phi) \tag{2.60}$$

Now, let's write the poloidal flux function gradient in a toroidal reference system:

$$\nabla\Psi = \frac{\partial \Psi}{\partial r}i_r + \frac{1}{r}\frac{\partial \Psi}{\partial \phi}i_\phi + \frac{\partial \Psi}{\partial z}i_z \tag{2.61}$$

recurring again to the rotational simmetry of the problem, the gradient expression can be simplified in the following and the problem can be rewritten from a tridimensional case to a bidimensional case in the (r,z) plane:

$$\nabla\Psi = \frac{\partial \Psi}{\partial r}i_r + \frac{\partial \Psi}{\partial z}i_z \tag{2.62}$$

Now taking again the equation 2.53 that states that the magnetic surfaces are perpendicular to the poloidal flux function gradient, it can be rewritten this relation as function of the magnetic potential vector:

$$(B_r i_r + B_z i_z) \cdot (\frac{\partial \Psi}{\partial r}i_r + \frac{\partial \Psi}{\partial z}i_z) = 0 \tag{2.63}$$

with the components of the magnetic field B_r and B_z given from the equations 2.58 and 2.60 and solving the scalar product between the two vectors it is obtained the following first order homogeneous scalar differential equation:

$$-\frac{\partial A_\phi}{\partial z}\frac{\partial \Psi}{\partial r} + \frac{1}{r}\frac{\partial}{\partial r}(rA_\phi)\frac{\partial \Psi}{\partial z} = 0 \tag{2.64}$$

to satisfy the equation, the azimuthal component of the magnetic potential vector A_ϕ must be function of the poloidal flux function Ψ, that is $A_\phi = A_\phi(\Psi)$. Solving for substitution it is obtained the following solution, that gives also the relation between the magnetic potential vector and the poloidal flux function:

$$A_\phi = \frac{1}{r}\Psi \tag{2.65}$$

from which can be write the poloidal components of the magnetic field vector as function of the

poloidal flux function, in agreement to the following relations:

$$B_r = -\frac{\partial A_\phi}{\partial z} = -\frac{1}{r}\frac{\partial \Psi}{\partial z} \tag{2.66}$$

$$B_z = \frac{1}{r}\frac{\partial}{\partial r}(rA_\phi) = \frac{1}{r}\frac{\partial \Psi}{\partial r} \tag{2.67}$$

We have now a relation between the components of the magnetic field vector in the poloidal plane and the poloidal flux function that was the initial aim of this study. Now the same derivation made for the magnetic field vector can be made for the current density vector $\vec{J}$, remembering that the current surfaces, as the magnetic surfaces, are perpendicular to the pressure gradient. It can be defined therefore a current density flux function f, equivalent to the poloidal flux function Ψ, that is a constant on the current surfaces, therefore it can be written:

$$\vec{J} \cdot \nabla f = 0 \tag{2.68}$$

that is the current density vector is perpendicular to the gradient of the current density flux function. Now from the derivation made for the magnetic field vector, the components of the current density vector can be rewritten in the poloidal plane as function of the current density flux function through the following expressions:

$$J_r = -\frac{1}{r}\frac{\partial f}{\partial z} \tag{2.69}$$

$$J_z = \frac{1}{r}\frac{\partial f}{\partial r} \tag{2.70}$$

It is necessary to find now an expression for the current density flux function f and to do so it can be equated one of the expressions obtained for the components of the current density vector in the poloidal plane with the one obtained from the Ampère-Maxwell equation. The Ampère-Maxwell equation states a relation between the magnetic field vector and the current density vector, and it is the following:

$$\nabla \times B = \mu_0 J \tag{2.71}$$

now rewriting the magnetic field rotor in cylindrical coordinates $(\hat{r}, \hat{\phi}, \hat{z})$ and using the axial simmetry of the problem $(\frac{\partial}{\partial \phi} = 0)$ it is obtained the following relation between the components of the magnetic field vector and the components of the current density vector in the toroidal reference system:

$$(-\frac{\partial B_\phi}{\partial z})i_r + (\frac{\partial B_r}{\partial z} - \frac{\partial B_z}{\partial r})i_\phi + (\frac{1}{r}\frac{\partial}{\partial r}(rB_\phi))i_z = \mu_0(J_r i_r + J_\phi i_\phi + J_z i_z) \tag{2.72}$$

equating the radial component of the magnetic field vector rotor with the radial component of the current density vector, it is obtained the following relation:

$$J_r = -\frac{1}{\mu_0}\frac{\partial B_\phi}{\partial z} \tag{2.73}$$

Comparing now the definition of the component J_r obtained from the Ampère-Maxwell equation

with the one computed as function of the current density flux function f, it is obtained the following equality:

$$J_r = -\frac{1}{\mu_0}\frac{\partial B_\phi}{\partial z} = -\frac{1}{r}\frac{\partial f}{\partial z} \tag{2.74}$$

that can be rewritten in the following way:

$$\frac{\partial}{\partial z}(\frac{B_\phi}{\mu_0}) = \frac{\partial}{\partial z}(\frac{f}{r}) \tag{2.75}$$

from which it is obtained the definition of the current density flux function f that is function of the toroidal magnetic field B_ϕ, and it is the following:

$$f = \frac{rB_\phi}{\mu_0} \tag{2.76}$$

From the magnetohydrodynamic equilibrium equation 2.49 it is proven that the magnetic field vector (equation 2.50) and the current density vector (equation 2.51) are perpendicular to the pressure gradient, therefore there are surfaces called magnetic surfaces or current surfaces in which the plasma pressure is constant. If the pressure gradient is parallel to the gradient of the poloidal flux function $\nabla\Psi$ (equation 2.53) and to the gradient of the current density flux function ∇f (equation 2.68), if each magnetic surface is identified from a constant value of the poloidal flux function, therefore the pressure function and the current density flux function can be written only as function of the variable Ψ. Obtaining therefore the following functional relations:

$$p = p(\Psi) \qquad f = f(\Psi) \tag{2.77}$$

At this point it must be made a clarification on the poloidal flux function Ψ, the definition that is given up to now (equation 2.52) is the one of the variable Ψ computed on the poloidal plane. Actually the poloidal plane is a 2D section of a 3D magnetic geometry. Assuming cylindrical symmetry of the geometry it can be assumed that the function Ψ computed with the equation 2.52 is the poloidal flux function for radiant and that the Ψ_{3D} is obtained multiplying for 2π the poloidal Ψ, as reported in the following relation:

$$\Psi_{3D} = 2\pi\Psi \tag{2.78}$$

The Ψ_{3D} so calculated is the value of the poloidal flux function associated to the tridimensional magnetic surface, while Ψ is the poloidal flux function associated to the bidimensional magnetic surface and therefore it is computed in the poloidal plane.
The equilibrium equation for an axisymmetric system (equation 2.49) as a tokamak can be written as a differential equation of the poloidal flux function Ψ. This equation has two arbitrary functions $p(\Psi)$ and $f(\Psi)$ and it is usually called the Grad-Shafranov equation. The MHD equilibrium equation 2.49 can be rewritten as function of the poloidal and the toroidal components:

$$J_p \times B_\phi i_\phi + J_\phi i_\phi \times B_p = \nabla p \tag{2.79}$$

where the subscript $_p$ indicates the poloidal component and the subscript $_\phi$ indicates the toroidal component. Recalling now the expressions of the magnetic field poloidal components (equations

2.66, 2.67) and of the current density (equations 2.69, 2.70), the magnetic field poloidal component can be written as:

$$B_p = B_r i_r + B_z i_z = -\frac{1}{r}\frac{\partial \Psi}{\partial z} i_r + \frac{1}{r}\frac{\partial \Psi}{\partial r} i_z = \frac{1}{r}(\nabla \Psi \times i_\phi) \tag{2.80}$$

while the current density poloidal component can be written as:

$$J_p = J_r i_r + J_z i_z = -\frac{1}{r}\frac{\partial f}{\partial z} i_r + \frac{1}{r}\frac{\partial f}{\partial r} i_z = \frac{1}{r}(\nabla f \times i_\phi) \tag{2.81}$$

where in both the expressions it has been defined $i_\phi = (0, 1, 0)$ as the toroidal axis versor of the toroidal reference system $(\hat{r}, \hat{\phi}, \hat{z})$. Substituting the poloidal components expressions for the magnetic field vector and for the current density vector in the MHD equilibrium equation written for components (equation 2.79), it is obtained the following relation:

$$\frac{1}{r}(\nabla f \times i_\phi) \times i_\phi B_\phi + \frac{J_\phi}{r} i_\phi \times (\nabla \Psi \times i_\phi) = \nabla p \tag{2.82}$$

and using the vector identity for the mixed vector product:

$$a \times (b \times c) = b(c \cdot a) - c(a \cdot b) \tag{2.83}$$

$$(a \times b) \times c = (a \cdot c)b - (b \cdot c)a \tag{2.84}$$

it is obtained the following expression of the MHD equilibrium equation:

$$-\frac{B_\phi}{r}\nabla f + \frac{J_\phi}{r}\nabla \Psi = \nabla p \tag{2.85}$$

that can be rewritten to obtain an expression for the toroidal current density:

$$J_\phi = r\frac{\nabla p}{\nabla \Psi} + B_\phi \frac{\nabla f}{\nabla \Psi} = r\frac{dp}{d\Psi} + B_\phi \frac{df}{d\Psi} \tag{2.86}$$

where in the last expression it is used the hypothesis that the plasma pressure p and the current density flux function f are functions only of the poloidal flux function Ψ. In addition from the definition of the current density flux function, it can be written the toroidal magnetic field B_ϕ in the following way:

$$B_\phi = \frac{\mu_0}{r} f \tag{2.87}$$

obtaining therefore the following expression for the plasma toroidal current density:

$$J_\phi = r\frac{dp}{d\Psi} + \frac{\mu_0}{r} f \frac{df}{d\Psi} \tag{2.88}$$

It must be rewritten the toroidal current density J_ϕ as function of the magnetic field vector components and therefore of the poloidal flux function Ψ. To do so we take the toroidal component of the Ampère-Maxwell equation 2.72, substituting in it the magnetic field vector poloidal components (equations 2.66, 2.67), obtaining in this way a further definition of the toroidal current density:

$$J_\phi = \frac{1}{\mu_0}(-\frac{1}{r}\frac{\partial^2\Psi}{\partial z^2} - \frac{\partial}{\partial r}(\frac{1}{r}\frac{\partial\Psi}{\partial r})) \tag{2.89}$$

Now equating the two expressions for the toroidal current density 2.88 and 2.89, it is obtained a second order partial differential equation written in a toroidal reference system (r, ϕ, z), known as the Grad-Shafranov equation:

$$\frac{\partial^2\Psi}{\partial r^2} - \frac{1}{r}\frac{\partial\Psi}{\partial r} + \frac{\partial^2\Psi}{\partial z^2} = -\mu_0 r^2\frac{dp}{d\Psi} - \mu_0^2 f\frac{df}{d\Psi} \tag{2.90}$$

This equation describes the axisymmetric magnetohydrodynamic plasma equilibrium that is confined magnetically, with the distribution of the function Ψ in the poloidal plane once assigned the source functions p and f that define the distributions of the plasma pressure and of the toroidal magnetic field in the poloidal plane.

2.6.1 Analytical solution of the Grad-Shafranov equation: Solov'ev solution

The Solov'ev solution is an analytical solution of the Grad-Shafranov equation that has been proposed by Solov'ev in his study in the 1967 [35]. This particular solution allows to define a plasma geometry that satisfy the MHD equilibrium equation for an axisymmetric plasma magnetically confined, of which there are known the fundamental geometric parameters as: the major radius R, the minor radius a and the value of the poloidal flux function at the plasma boundary Ψ_B. The hypotheses at the basis of the Solov'ev solution that allow to compute an analytical solution of the Grad-Shafranov equation are: source functions gradients are constant around the magnetic axis and the poloidal flux function Ψ on the poloidal plane and around the magnetic axis can be described with a power series expansion in the variables r and z.
The first hypothesis is described from the following relations:

$$\frac{dp}{d\Psi} = -\frac{c_1}{\mu_0} \tag{2.91}$$

$$f\frac{df}{d\Psi} = -c_2 R^2 \tag{2.92}$$

where c_1 and c_2 are constants, μ_0 is the vacuum magnetic permeability and R is the major plasma radius. The second hypothesis assumes that the solution of the Grad-Shafranov equation is symmetric with respect to the z = 0 plane and it is given from a power series expansion around the point r = R and z = 0, that is the following:

$$\Psi = \sum_{n=0,1,2\ \ m=0,1} a_n(r^2 - R^2)^n b_m(z^2)^m \tag{2.93}$$

from which expanding the various terms of the summation, it is obtained the following extended expression:

$$\Psi = a_0b_0 + a_0b_1z^2 + a_1b_0(r^2 - R^2) + a_1b_1(r^2 - R^2)z^2 + a_2b_0(r^2 - R^2)^2 + a_2b_1(r^2 - R^2)^2z^2 \tag{2.94}$$

where it has been considered an even exponent for the variable z^2 to have a symmetry of the

solution with respect to the z = 0 plane and the expression is truncated to the power 2 for the variable z because the differential equation is of the II order. The same is for the exponent of the term $(r^2 - R^2)$ that has been considered up to the II power because this power was already sufficient to satisfy the differential equation. In addition it has been added a constant term $a_0 b_0$ to allow that the magnetic axis can be shifted with respect to the geometric axis. Substituting the power serie for the variable Ψ in the Grad-Shafranov equation it is found the following solution of the differential equation that is the one of lowest order that satisfies it:

$$\Psi = a_0 b_0 + a_0 b_1 z^2 + a_1 b_1 (r^2 - R^2) z^2 + a_2 b_0 (r^2 - R^2)^2 \tag{2.95}$$

The same terms of this power series expansion are reported in the Solov'ev article [35], for the solution that he proposed. The Solov'ev solution is taken to validate the MATLAB pdetoolbox numerical solver [36] that has been used to solve the non linear Grad-Shafranov equation. In particular it has been compared the Solov'ev analytical solution with the numerical solution obtained integrating the Grad-Shafranov equation with the Solov'ev hypotheses, that resulted in a perfect superimposition between the two solutions. To do so it has been taken the general differential equation in the scalar variable u, written in a cartesian reference system, solved by MATLAB with the pdetoolbox that is the following:

$$-\nabla \cdot (c \nabla u) + au = f \tag{2.96}$$

that written in a bidimensional cartesian reference system becomes:

$$c\left(\frac{\partial^2 u}{\partial x^2} + \frac{\partial^2 u}{\partial y^2}\right) + \frac{\partial c}{\partial x}\frac{\partial u}{\partial x} + \frac{\partial c}{\partial y}\frac{\partial u}{\partial y} - au + f = 0 \tag{2.97}$$

This second order partial differential equation can be solved in MATLAB given properly the coefficients a,c, f and the boundary conditions. To do so it must be equated the differential equation to the Grad-Shafranov equation putting u = Ψ and assuming that in the poloidal plane the solution of the cylindrical reference system and the one of the cartesian reference system are the same. The Grad-Shafranov equation in cylindrical coordinates is the following:

$$\frac{1}{r}\left(\frac{\partial^2 \Psi}{\partial r^2} + \frac{\partial^2 \Psi}{\partial z^2}\right) - \frac{1}{r^2}\frac{\partial \Psi}{\partial r} + \mu_0 r \frac{dp}{d\Psi} + \frac{g}{r}\frac{dg}{d\Psi} = 0 \tag{2.98}$$

where it has been indicated with g the current density flux function, to not confuse it with the coefficient f of the MATLAB pdetoolbox differential equation. Equating the two differential equations the coefficients of the MATLAB pdetoolbox differential equation are obtained, that are the following:

$$a = 0 \qquad c = \frac{1}{x} \qquad f = \mu_0 x \frac{dp}{dx} + \frac{g}{x}\frac{dg}{d\Psi} \tag{2.99}$$

In the following images is reported a comparison between the Solov'ev analytical solution and the numerical solution computed with the MATLAB pdetoolbox.

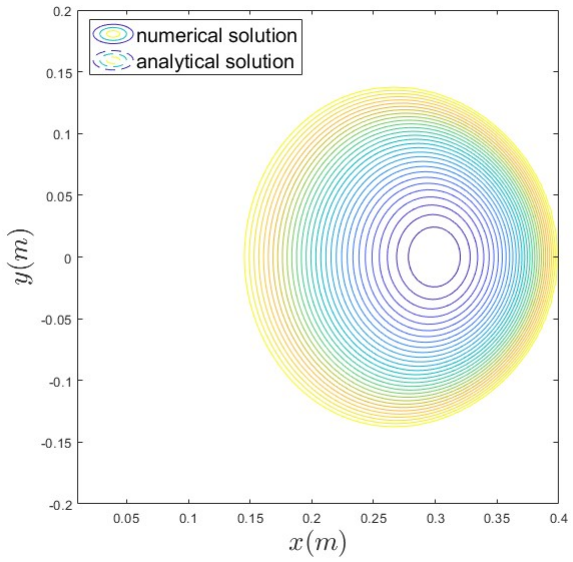


Figure 2.1: Comparison between the analytical solution and the numerical solution

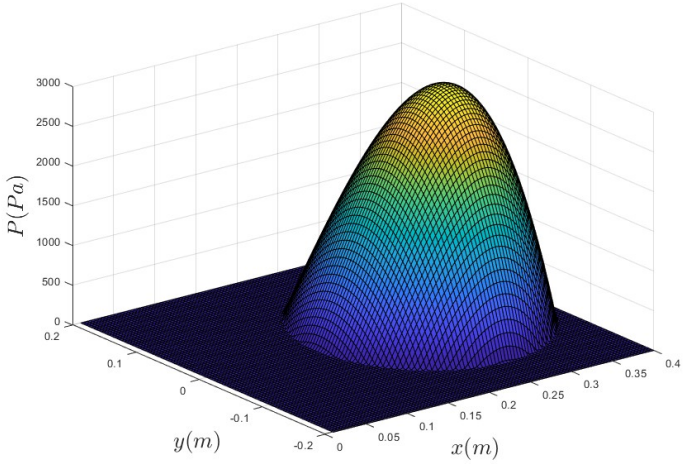


Figure 2.2: Plasma pressure distribution

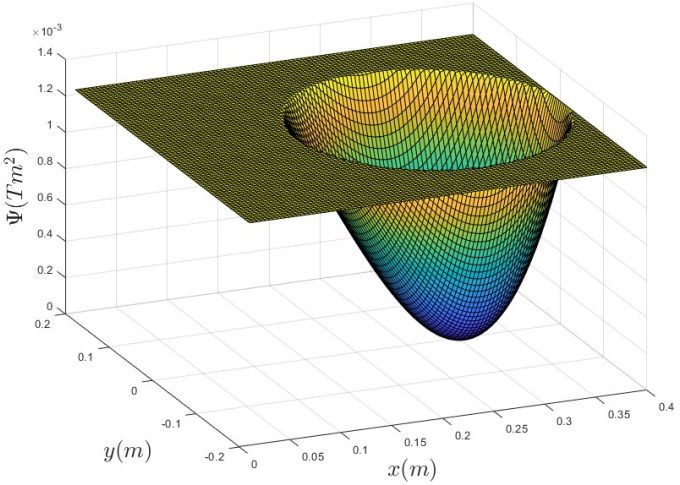


Figure 2.3: Poloidal flux function distribution Ψ

2.7 Thermonuclear fusion physics

Nuclear fusion is a promising energy source to sustain the increasing world energy demand. Fusion reactions feed the Sun and other stars. In the fusion reactions, small masses nuclei are fused to form more massive nuclei. In the Sun a sequence of fusion reactions, called the p-p chain, starts with the protons, nuclei of the ordinary hydrogen, and it ends with the alpha particles, nuclei of the helium atoms. After a fusion reaction the product masses are lower than the reactant masses and the missing mass (the mass defect) is converted in energy as quantified from the well known Einstein equation:

$$E = (m_R - m_P)c^2 \tag{2.100}$$

where E is the energy resulting from the reaction, m_R is the reactant nuclei mass, m_P is the product nuclei mass and c is the speed of light. The thermonuclear fusion is an esoenergetic reaction which reaction products are charged particles, highly energized obtained indeed from the fusion of two atomic species that collide at high temperature. The charged fusion products (ions and electrons) can be magnetically confined in power generation systems (nuclear reactors), while the neutral products (neutrons) can be collected at the edge of the fusion reaction to extract the transported energy. The lighter reactant species that can be used for the nuclear fusion reactions are hydrogen, its isotopes (deuterium and tritium) and helium, and among these the reactant combinations that produce the lowest amount of neutrons is the deuterium-helium3. There are four fusion reactions that are part of the fusion reaction mechanism for deuterium-helium3 [17]. The first one is the deuterium-helium3 reaction itself, that does not produce neutrons (aneutronic reaction). There are also two side reactions deuterium-deuterium that happen in almost equal proportion, one of these produces a moderate neutronic energy and more helium3, while the other produces tritium and a proton. The last reaction, deuterium-tritium, produces neutrons at high energy.

$$D + {}^3He \rightarrow {}^4He(3.6MeV) + p(14.7MeV) \tag{2.101}$$

$$D + D \rightarrow T(1.01MeV) + p(3.02MeV) \tag{2.102}$$

$$D + D \rightarrow {}^3He(0.82MeV) + n(2.45MeV) \tag{2.103}$$

$$D + T \rightarrow {}^4He(3.45MeV) + n(14.1MeV) \tag{2.104}$$

The fusion reaction cross sections as function of the reactant particles energy can be estimated from the Duane 5 parameters formula [37], that is the following:

$$\sigma(E) = \frac{A_5 + [(A_4 - A_3E)^2 + 1]^{-1}A_2}{E[\exp(A_1E^{-\frac{1}{2}})] - 1} \tag{2.105}$$

where σ is the total cross section in barns ($1barn = 10^{-24}\ cm^2$), E is the energy in keV of the incident particle (the first ion on the left side of the fusion reaction), assuming that the target ion

is stopped and A_i are the fitting coefficients which values for the considered fusion reactions are tabulated in [38]. The trend of the cross sections for the previous fusion reactions is reported in the following Figure 2.4.

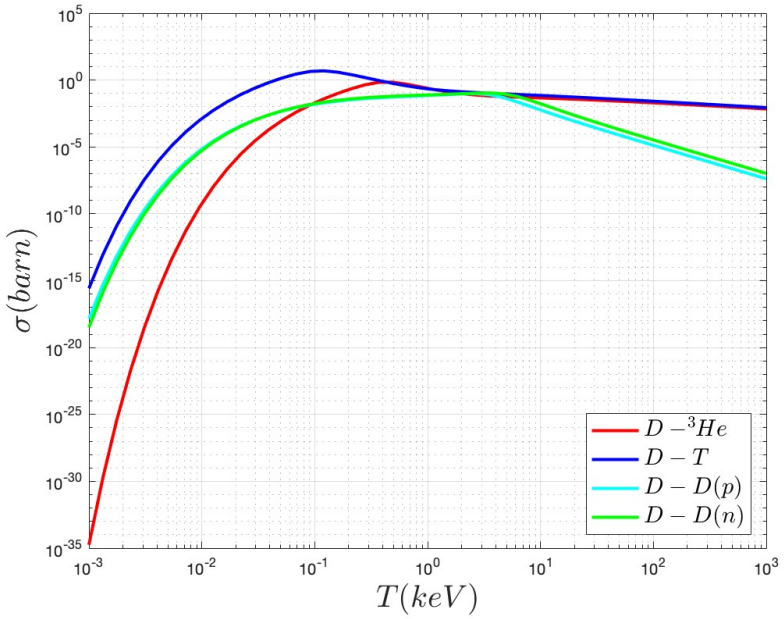


Figure 2.4: Cross sections of the $D-{}^3He$ fusion reaction mechanism

The cross sections obtained are in good agreement with the reported data in [37] and they show a maximization of the fusion reactions cross sections for incident ions temperatures between 100 eV and 10 keV. The main parameter to evaluate the optimal temperature of a fusion reaction is not the cross section but the mean reaction velocity, that is directly proportional to the product between the reaction cross section σ and the nuclei relative velocity v and it determines the fusion power produced from the fusion reaction. Assuming a maxwellian distribution of the reactant species the quantity $<\sigma v>$ is computed as [39]:

$$<\sigma v>=\frac{4}{(2\pi m_1)^{\frac{1}{2}}}(\frac{\mu}{m_1 k_B T})^{\frac{3}{2}}\int_0^{\infty}\sigma(E)E\exp(-\frac{\mu E}{m_1 k_B T}) \tag{2.106}$$

where k_B is the Boltzmann constant, T is the temperature of both species, m_1 is the mass of the ion with energy E and μ is the reduced mass of the two fusing ions. The fusion power density released from the fusion products can be calculated from the following formula:

$$P_{fus}=n_1 n_2 <\sigma v>_{ij} E_{fus} \tag{2.107}$$

where n_1 and n_2 are the densities of the two reactant species, and the product $n_1 n_2 <\sigma v>_{ij}$ is the velocity of the fusion reaction per unit of volume and E_{fus} is the energy released from each fusion reaction.

Taking some tabulated values for the product $<\sigma v>_{ij}$ for the fusion reactions considered up to now [38], in the following images 2.5 and 2.6 are reported the trend of $<\sigma v>_{ij}$ and the produced fusion power.

In the computed graphs it is considered an average density of the reactants of $10^{20} particles/m^3$,

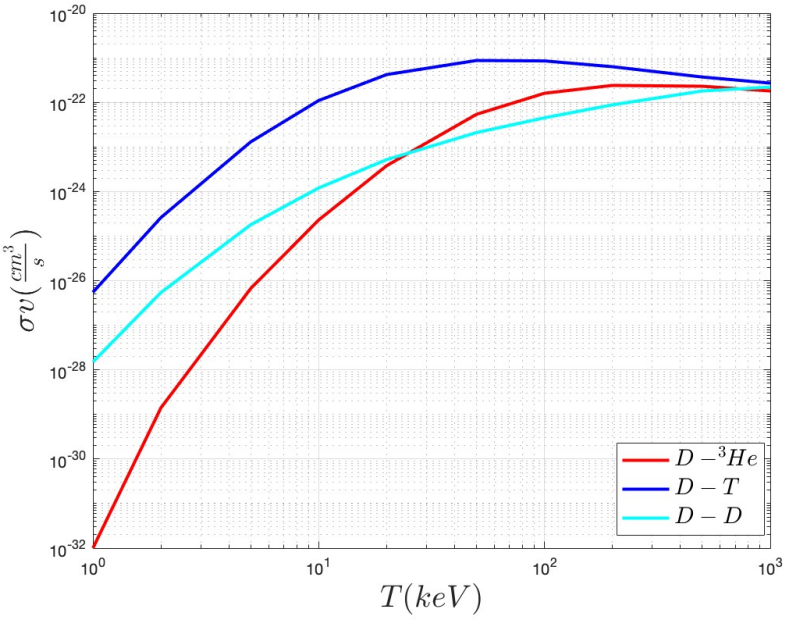


Figure 2.5: Coefficient of the fusion reaction rate for the considered reactions, $< \sigma v >_{ij}$

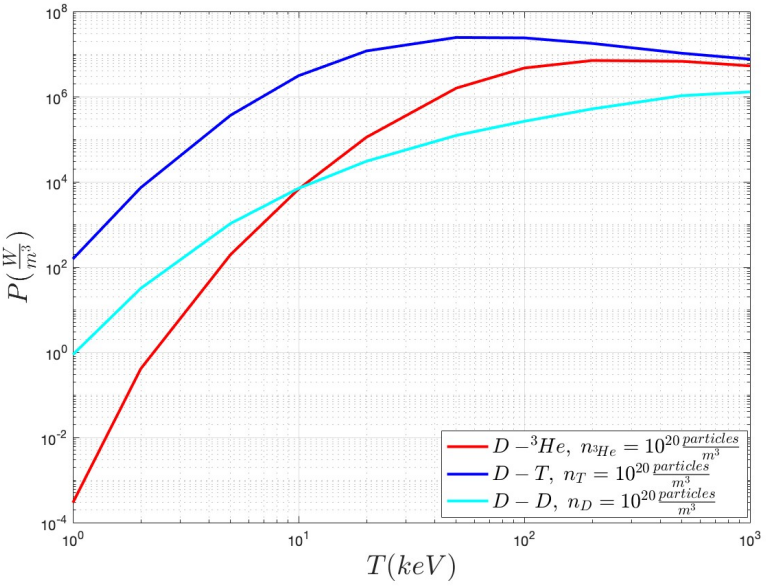


Figure 2.6: Fusion reactions power

from which it is computed the generated fusion power. The reaction rate and the fusion power in the temperature range considered for the reactants ($1keV < T < 1MeV$) are maximized for reactants temperatures between $10keV$ and $100keV$ for the reaction Deuterium-Tritium which has the highest value of the produced power, making this temperature range of interest for the ignition of the fusion reaction. The highest reaction rate of the Deuterium-Tritium reaction makes the Tritium highly reactive inside the reaction mechanism of Deuterium-Helium3 and making less critical the Tritium removal [17] for the Deuterium-Helium3 reaction. The power developed from the fusion reactions, for the considered density level of the reactants, is very high in its peak value that is of the order of fractions of Gigawatts, making these fusion reactions interesting both for the design of nuclear fusion reactors to produce energy and for the design of space vehicles fed by fusion reactors [17]. The power level obtained from the nuclear fusion reactions are reported in figure 2.6. A nuclear fusion propulsion system, given the high power developed from the nuclear fusion reactions and the high temperature of the produced charged particles can be highly efficient and with the specific impulse among the highest under designing currently. The magnetic confinement technology can be applied to the fusion reactor concepts because the fusion reaction products are charged particles and therefore they can be magnetically confined within the closed magnetic configuration [40], allowing the control, feeding and sustainment of the fusion reaction.

2.7.1 The Lawson criterion

The aim of a fusion reactor is the energy net production because a useful reactor must produce more power from the reaction than it is required to heat the plasma and to the operation of the machine. Now the conditions, that must be satisfied to reach this aim, are introduced [1]. Let's analyze the reaction Deuterium-Tritium (D-T). The thermal energy density (i.e. the energy per unit of volume) W in the plasma is given by:

$$W = \frac{3}{2}(n_D + n_T + n_e)T, \tag{2.108}$$

where n_D is the number density of the Deuterium ions (ions per unit of volume), n_T is the number density of the Tritium ions, n_e is the number electron density, and T is the temperature expressed in eV. Assuming that the fuels, for the reaction of Deuterium and Tritium, are in equal quantity and considering that there is an electron for each ion of Tritium and Deuterium, then:

$$n_D = n_T = \frac{n_e}{2} \tag{2.109}$$

Assuming $n = n_e$, is then possible to write:

$$W = 3nT \tag{2.110}$$

A simple power balance in the plasma can be written as:

$$\dot{W} = P'_{fusion} + P_{external} - P_{loss} \tag{2.111}$$

where P'_{fusion} is the power density produced from the nuclear fusion reaction that stays in the plasma and that contributes to the increase of the plasma thermal energy, $P_{external}$ is the power density produced from the additive axternal heating devices and finally P_{loss} is a term that represents

all the power lost.
There are two main mechanisms of power loss in a plasma, the first is due to the fact that the plasma confinement is not perfect, and therefore particles and heat diffuse from the plasma center towards the outside; the second is due to bremsstrahlung, this term indicates the produced radiation when the plasma electrons impact other charged particles, as electrons and ions, that are at a lower temperature and rapidly decelerate. The power density lost for bremsstrahlung is given by:

$$P_{bremsstrahlung} = 1,69 \cdot 10^{-38} n^2 Z_i^2 T^{\frac{1}{2}} \tag{2.112}$$

where Z_i is the ion charge (that for a D-T mixture is equal to 1).
The power density produced from the nuclear fusion reaction is a function of the particles density and of the thermal energy itself. Indeed, high thermal energy of the particles allow the plasma nuclei to overcome the Coulomb repulsive force easily, while the density determines the probability for two ions to interact. The reaction rate per unit of volume is given by:

$$R_{DT} = n_D n_T < \sigma v >= \frac{1}{4} n^2 < \sigma v > \tag{2.113}$$

where $< \sigma v >$ is the reaction rate coefficient and it depends on the plasma temperature, in figure 2.5 is reported the dependence for the D-T reaction. To calculate the fusion power density P_{fusion} the fusion reaction rate is multiplied for the energy E_{fus} obtained from the fuction reaction, that is equal to $17.55 MeV$ (equation 2.104), obtaining in this way:

$$P_{fusion} = R_{DT} E_{fus} = \frac{1}{4} n^2 < \sigma v > E_{fus} \tag{2.114}$$

The part of this power density that stays within the plasma can be evaluated as:

$$P'_{fusion} = R_{DT} E'_{fus} = \frac{1}{4} n^2 < \sigma v > E'_{fus} \tag{2.115}$$

where $E'_{fus} = 3,45 MeV$ is the helium ion energy after the fusion reaction (equation 2.104); the remaining part of the power density is associated with the neutral particles that leave the confined plasma to reach the blanket.
Coming back to the equation 2.111, if the source term $P'_{fusion} + P_{external}$ is greater than the loss term P_{loss}, then the plasma gains energy, otherwise it loses energy. In steady state regime, the source term compensates the losses, and the plasma thermal energy stays constant. In this condition is useful to define the energy confinement time τ_E, and the amplification factor Q. The energy confinement time is defined as:

$$\tau_E = \frac{W}{P_{loss}} \tag{2.116}$$

The time τ_E is the characteristic time of plasma thermal energy decrease; it is related to the time required to dissipate completely the plasma energy if the sources that sustain it would be turned off.
The amplification factor is the ratio between the produced power from the fusion reaction and the power given from the external heating devices:

$$Q = \frac{P_{fusion}}{P_{external}} \tag{2.117}$$

If $Q = 1$ then the produced power by the nuclear fusion reaction is equal to the power given by the external heating devices. This is the so called break-even condition, where the plasma heating is made both from the charged particles and from the additional heating but it is not a situation that allows the energy production. If $Q = \infty$ the condition reached is the ignition, in this case $P_{external} = 0$ and the plasma thermal energy is completely sustained from the nuclear fusion reaction. A nuclear fusion reactor must operate with an amplification factor Q significantly higher than 1. The break-even condition has been reached with D-T in tokamaks JET and JT-60, in particular in JT-60 it has been obtained the world record value of $Q = 1.25$ [1].
The break-even and ignition conditions are generally expressed with the Lawson criterion. Assuming a stationary condition, with $\dot{W} = 0$, the power balance equation 2.111 become:

$$P_{fusion}(\frac{E'_{fus}}{E_{fus}} + \frac{1}{Q}) = \frac{W}{\tau_E} \tag{2.118}$$

where the following relations have been used:

$$P'_{fusion} = \frac{E'_{fus}}{E_{fus}} P_{fusion} \tag{2.119}$$

$$P_{external} = \frac{P_{fusion}}{Q} \tag{2.120}$$

$$P_{loss} = \frac{W}{\tau_E} \tag{2.121}$$

Using the equations 2.110 and 2.114, the equation 2.118 can be written as:

$$n\tau_E = \frac{12}{E_{fus}(\frac{E'_{fus}}{E_{fus}} + \frac{1}{Q})} \frac{T}{< \sigma v >} \tag{2.122}$$

The equation 2.122 is the Lawson criterion and the figure 2.7 shows the Lawson criterion curve for the Deuterium-Tritium reaction, distinguishing between the ignition condition ($Q = \infty$), the break-even condition ($Q = 1$) and the sustained reaction ($Q = 1.5 > 1$). From the figure it can be noted that the Lawson criterion curve corresponding to the sustainment condition of the fusion reaction is always between the ignition curve, that is the maximum value reachable for the amplification factor Q, and the break-even curve, that corresponds to the minimum value reachable for the amplification factor Q. For example the Lawson criterion for ignition in a D-T fusion reactor is:

$$n\tau_E = \frac{12}{E'_{fus}} \frac{T}{< \sigma v >} \tag{2.123}$$

For $T = 25keV$ (that is a temperature close to the minimum of $T/ < \sigma v >$), it is obtained:

$$n\tau_E \approx 1,7 \cdot 10^{20} \frac{particelle}{m^3} s \tag{2.124}$$

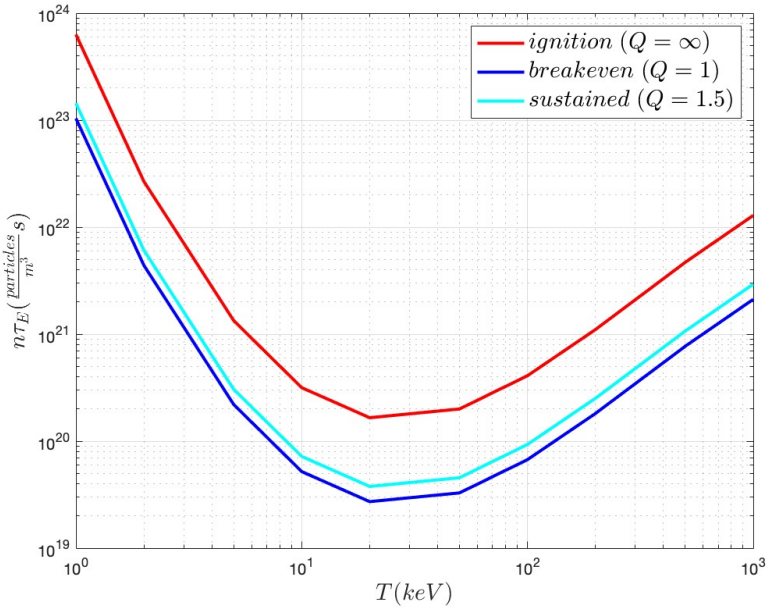


Figure 2.7: Lawson criterion for the fusion reaction Deuterium-Tritium

Once that is fixed the plasma temperature, the Lawson criterion determines the product of the density and the energy confinement time that must be satisfied. A difference between the inertial confinement method and the magnetic confinement method is that in the first the energy confinement time is very low (between 10 and 100ps) and the density is extremely large (of the order of $10^{31} particles/m^3$, orders of magnitude higher than the hydrogen density at solid state); on the contrary, in the magnetic confinement devices densities are smaller (of the order of $10^{20} particles/m^3$, lower than the air density), therefore the energy confinement time must be greater (of the order of $1s$). In this PhD thesis a generalized Lawson criterion will be applied for magnetic fusion application in space that models through a power balance equation both the confinement of the fusion reaction, the recovery of energy to sustain the fusion reaction and the nuclear fusion propulsion system [41].

2.7.2 The nuclear fusion reactor: the tokamak

The tokamak is a concept invented in the Soviet Union at the Institute of Atomic Physics in Moscow by A. Sakharov and I. Tamm in the 1950 and it is now the major and more promising approach to magnetic confinement designed in the world. The tokamak is an acronym of the russian words "TOroidal-naya KAmera i ee MAgnitaya Katushka" that means "toroidal camera with magnetic coils". As stated in the name it is a device for magnetic confinement with toroidal geometry.

The bigger tokamak in the world is the Joint European Torus (JET) in Culham, England. The tokamak DIII-D is one of the dozen of middle size in the world, others tokamak are FTU in Italy and TCV in Switzerland.

The tokamak is nowadays the device most promising for the development of power plants based on nuclear fusion, it can be one of the best approach to the energy generation in the long period and therefore it is under investigation with intensive international research programs, one of the major is the ITER project.

The figure 2.8 shows an image of the ITER tokamak with:

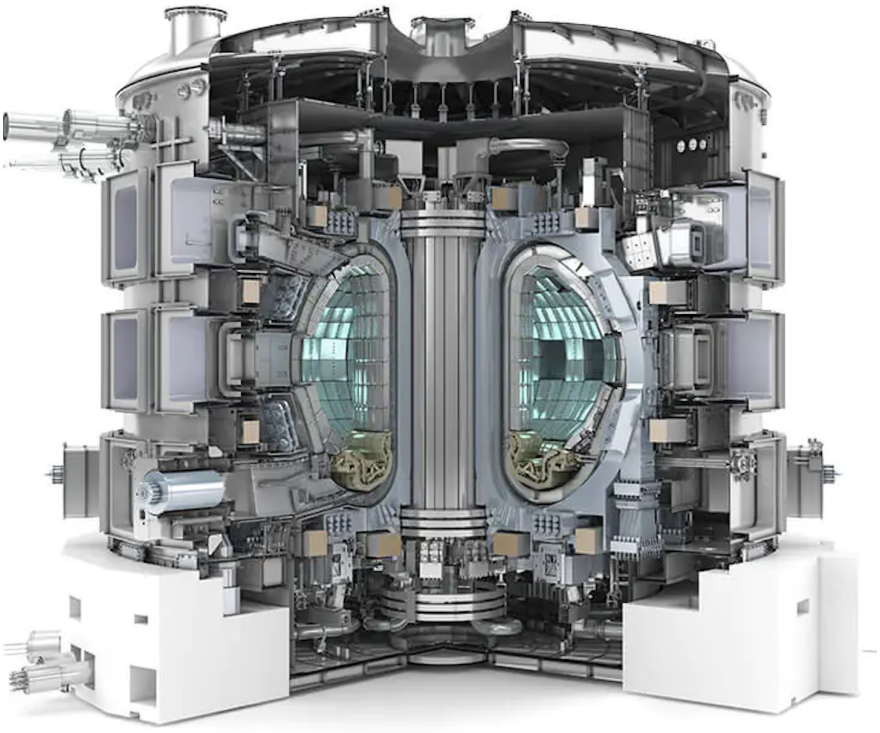


Figure 2.8: Image of the tokamak ITER [1]

- the vacuum chamber (vacuum vessel), the chamber where the plasma is contained;
- the blanket, that has the main role of absorbing the neutrons energy and to feed the plasma with Tritium that is required for the Deuterium-Tritium reaction (equation 2.104). For this reason the blanket is generally made with Litium, so that the following reaction can take place:

$$^6Li + n \rightarrow ^4He + T \ \ (4.8MeV) \tag{2.125}$$

- the toroidal coils. The currents that flow in these coils generate a poloidal field (poloidal field coils, or PF coils). The coils in the middle of the machine are called central solenoid (CS); the plasma current is generated by action of the transformer, with the central solenoid that is the primary transformer and the plasma itself that acts as a secondary transformer;
- the poloidal coils. The currents that flow in these coils generate a toroidal field (toroidal field coils, or TF coils).

In presence of a given magnetic field, a charged particle describes a simple cyclotron gyration around the magnetic field line. The charged particle dynamic is determined from the Lorentz force and when the component of the velocity parallel to the magnetic field lines, that is not affected by the Lorentz force, is different from zero, the charged particle trajectory is a spiral. To mantain the confined particles in their motion around the magnetic field lines, the tokamak uses field lines that are wrapped in a torus and closed on themself. In a tokamak, the toroidal magnetic field is produced from the poloidal coils (TF coils). The addition of a poloidal field generated from the toroidal plasma current, that is required for the magnetohydrodynamic equilibrium (MHD), produces a combined magnetic field in which the magnetic field lines are twisted around the tokamak forming a

helical structure. This topology of the magnetic field is fundamental for the stability of the plasma confinement, because the charged particles trapped in the magnetic geometry are subjected to drift motions that are caused by plasma inhomogeneity, curvature of the field line, interaction between electric field and magnetic field and these drift motions can lead to the lost of the confinement for the charged particles. Therefore introducing a rotational transform, that is a small angle of rotation of the magnetic field lines around the toroidal axis, these drift motions are compensated in the orbit of the charged particles around the symmetry axis and this lead to a spiral geometry of the magnetic field lines that increases the confinement of the charged particles. The stability of the magnetic configuration due to the introduction of a rotational transform is measured by the safety factor.
The tokamak reactors are pulsed machines; in each pulse the plasma is created ("start-up" phase), then its current is increased up to a constant reference value, called "flat-top" current, that is mantained for a certain time, and then the current is decreased ("ramp-down") and the plasma is terminated. The evolution in time of the currents in the toroidal coils (PF coils) and in the poloidal coils (TF coils) and of the main plasma parameters that guarantee this sequence define a "scenario".
To increase significantly the fusion reactions, the temperature must be increased to over 100 million of Kelvins (equation 2.5), that is six times the Sun temperature. This heating is reached with particles injection (injecting energetic atoms) or with radiofrequencies or microwaves (ion or electron heating).

Chapter 3

Helicon thruster design

3.1 Helicon thruster design for cislunar cargo missions

In this chapter is introduced the HELICARGO project that is a research project on the design of a helicon thruster for a cislunar mission. This project along with the experimental research on plasmas conducted in ENEA have been the starting point for the study of the helicon thruster. In the chapter the design of the helicon thruster is treated in a first part focusing on the design of the helicon antenna, a main component of the helicon thruster required for the plasma ionization, for which different design methods have been proposed. Then in the successive paragraphs a global design model for the helicon thruster is proposed that combines the design method of the helicon antenna, to which are applied also electromagnetic simulations of the plasma, and PIC simulations of the magnetic nozzle. The design methods are enterily developed in this PhD study and they constitute a new methodology for the design and development of a helicon thruster. The aim of this research part is to design and test a helicon antenna to be integrated in a helicon thruster, fed by Iodine a green solid propellant that can make more compact, light and environmental friendly the propulsive system of the helicon thruster.
The helicon thruster is a plasma electromagnetic thruster that can operate in space vacuum, its working principle is based on a gas ionization made by a radiofrequency source (RF) and on a magnetic nozzle that accelerates and expels the generated plasma. The plasma source of the helicon thruster is a helicon antenna, a device that couples RF power with the plasma, ionizing it and sustaining the propagation of helicon waves. The magnetic nozzle is instead designed typically with a series of electromagnets and/or permanent magnets that are positioned around the helicon antenna and that have the function both of generating the axial confinement magnetic field of the plasma and of generating the divergent magnetic field for the plasma acceleration. The variation of the magnetic field intensity and direction allows to control the thrust intensity and direction of the helicon thruster and therefore to orient it in space.
The helicon thrusters are thrusters relatively simple and compact with respect to others plasma thrusters, because they require only few components for the design and can scaled in size. They are devices capable to produce high particles velocity in the plasma jet and therefore high specific impulses and so they have a high efficiency propellant consumption. They are currently under study to be used in a variety of space missions for satellite propulsion and for deep space exploration missions. One of the missions in which they can be employed also are the ones inside the cislunar

space. The cislunar space is defined as the space between Earth and the Moon or the space within the Moon orbit around the Earth. It includes the earth orbit that are currently occupied by satellites beyond geosynchronous orbits (GSO) as the moon transit orbit, the moon orbits and the Lagrange points. Space vehicles can operate in a variety of trajectories in the cislunar space, among which moon orbits, translunar orbits and in orbits family in the big regions around the Earth-Moon Lagrange points. A region included in the cislunar space is the Moon surface itself.
As known the Moon show always the same side of its surface to the Earth, allowing to have direct telecommunication and continuous from the Earth to the Moon. The Moon polar regions are rich of resources, there are regions that are exposed to the sun light almost continuously and regions extremely cold and permanently in shadow that can conservate significantly deposits of ancient ice and other chemical compounds. In the next future the Moon and asteroids close to the Earth will be explored to research and to exploit mineral resources, metals and rare materials. The cislunar space beyond being of interest for the exploration and the research of resources is the door to the rest of the solar system, it is precious to test our systems and to create new settlements in preparation of future robotic and human missions towards other planets and the deep space. The helicon thruster design is for realizing a future mission capable to respond to the needs of materials/goods transportation from the low Earth orbit to the Moon orbit. The project foresees the use of innovative electric technology, based on a thruster fed by iodine as "green propellant", that uses an efficient RF system to ionize the propellant that is made by an helicon antenna and a confinement magnetic field that is generated by permanent magnets and/or high efficient electromagnets.
The helicon antennas of the helicon thrusters have the capability to generate plasmas with high ionization efficiency at low temperature (1-3 eV) and at high density ($10^{19} particles/m^3$ or even higher) and the helicon thruster offers the following advantages:

- high plasma density with respect to inductive systems
- it is electrodeless
- longer engine life
- simplicity of the manufacturing
- high specific impulse
- easily to ignite and to shutdown

These features of the helicon thruster make it very attractive for the high propellant ionization efficiency and the lower deterioration of the thrust chamber walls. The iodine choise is compatible with the constraints of volume and costs for the space vehicles. Iodine is a green propellant, safe and with low environment impact, it does not require a pressurizing system, it has a low cost and it is therefore suitable both for accademic and commercial applications. With respect to Xenon, Iodine has a storage density that is three times higher, moreover it is storable in solid state with a low vapor pressure, meaning that the propellant tank can be designed with light materials, reducing the space vehicle structural mass.

3.2 The HELICARGO project

The HELICARGO project proposed to ASI (the Italian Space Agency) from SIA (School of Aerospace Engineering) and ENEA (National Agency for new technologies, energy and sustainable development) is to develop a helicon thruster for cislunar missions with the aim to verify its feasibility. Such proposal responds to the need for Europe and in particular for Italy to fill the technological gap with respect to other nations such as the United States of America, the Russian Federation and the Chinese Popular Republic. Indeed, while the United States and the Russia have a strong lunar exploration history and the China has currently the biggest support point in the cislunar space, Europe and Italy don't have now a notable role, but only marginal to support the collaboration. The cislunar space offers strategic resources, among which water, helium-3, rare metals and regolith, in addition the cislunar space is a unique opportunity to extrapolate technology made for future missions such as Mars exploration.
Despite the remarkable development in electric propulsion for such future applications, the TRL (Technology Readiness Level) of the helicon thruster has not reached a mature technological level. In this framework, HELICARGO proposes to meet this need with innovative technological solutions that can make Italy leader, at european level, in the development of a electric thruster for cislunar missions.
The interest for the cislunar space is not recent, from always, in fact, the Moon has been an engine of scientific progress and it could bring also to a potential economic growth. The opportunities for the research and the development in the cislunar space go from the new discoveries in the space science up to the development of new cislunar technologies and to new discoveries in the comprehension of the space environment effects on human being. The HELICARGO project team proposes the development of an innovative helicon thruster fed by Iodine that implements an innovative plasma acceleration configuration with the coupling of a radiofrequency ionization system, coils and permanent magnets to increase the propellant ionization efficiency and to allow to have higher thrust and specific impulse. The advantage in the use of Iodine as propellant, with respect to propellants more common for the electric thrusters as Xenon, are many: it is abundant, it is economic, it is storable at solid state (it is therefore less bulky and more safe) and it sublimates at low temperatures. The challenges remain: at the moment iodine engines are not so fast reactive as their counterpart with Xenon. There are some difficulties with Iodine that must be overcome. For example, Iodine reacts with most metals, therefore ceramics and polymers must be used to protect parts of the propulsion system. It has been proven that solid Iodine takes almost ten minutes to become a plasma, this could not provide propellant sufficiently rapidly to emergency maneuvers to avoid orbit collisions, however the improving sublimation and ionization times will also be the subject of the HELICARGO project.
This first feasibility study allows to obtain a design knowledge on the feeding system and Iodine sublimation, on the plasma generation and its confinement, on the propellant acceleration subjected to the interaction with the radiofrequency and on the thruster performance.

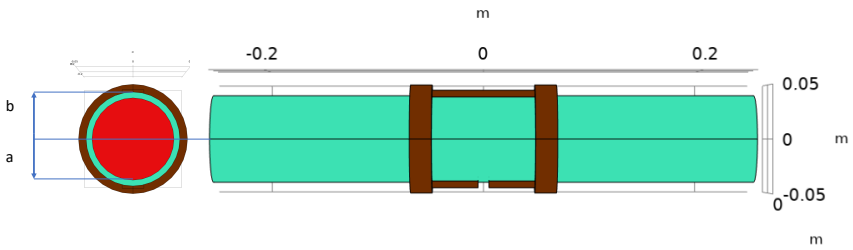


Figure 3.1: Mechanical design of the Nagoya type-III helicon antenna

3.3 Design of a helicon antenna

Helicon waves can be excited in a magnetized plasma with helicon antennas that are designed to couple RF power with the normal modes of magnetized plasma, allowing the helicon waves propagation. The Nagoya type-III antenna [26, 27, 42] is a helicon antenna of cylindrical geometry that is selected in this work [43] for its simplicity of use with respect to other helicon antennas [44, 45] and for the good experimental results obtained in ionizing gas [27]. In this study the antenna is fed with a radiofrequency source (RF) with a power level of 1 kW. Inside the cylindrical ionization chamber, an Argon gas is considered almost completely ionized and it is assumed steady state regime for the antenna. The plasma is considered uniform spatially in order to simplify the analysis, but also because an experimental helicon discharge develops a plasma almost uniform [27, 46]. Therefore this simplification is not far from a realistic situation. A magnetostatic uniform field, generated by external coils, is directed along the axial direction allowing the propagation of helicon waves in the plasma column. In addition in the following design methods it is considered a simple cylindrical geometry (figure 3.1) with inner quartz tube radius a, antenna radius b and antenna length L_a. It is assumed also for simplicity that the plasma radius is approximately equal to the quartz tube inner radius (a).

3.3.1 Design method 1

The first design method is based on the generalized helicon wave theory [23, 24]. This antenna design method takes into account the electron inertia and it is based on the computation of the real part of the antenna-plasma impedance [24] that is a measure of the antenna capacity to couple power in the plasma [2]. For a given discharge quartz tube and fixing the plasma parameters, the deposited power in the plasma can be maximized for a given value of the antenna length, allowing the computation of an optimal antenna length, $L_{optimum}$. It is assumed that the plasma is an electron uniform single specie fluid that can collide with a static ionic background and with a neutral gas (Argon is assumed therefore partially ionized with single ionization charge) and the plasma is in steady state harmonic regime, with waves represented as $\exp i(m\theta + kz - \omega t)$, propagating in a collisional plasma with a magnetostatic field $\vec{B} = B_0\hat{z}$. A cylindrical reference system $(\hat{r}, \hat{\theta}, \hat{z})$ is assumed and

the field perturbations have cylindrical symmetry. Specifically, the helicon wave model is based on the Maxwell equations and on the momentum conservation equation for an electron fluid, as reported in the following equations system:

$$\begin{cases} \nabla \cdot \vec{B} = 0 \\ \nabla \times \vec{E} = i\omega\vec{B} \\ \nabla \times \vec{B} = \mu_0(\vec{J} - i\omega\varepsilon_0\vec{E}) = -i\omega\varepsilon_0\varepsilon\vec{E} \\ -i\omega m_e\vec{v} = -e(\vec{E} + \vec{v} \times \vec{B_0}) - m_e\nu\vec{v} \end{cases} \tag{3.1}$$

with the quantities already defined in section 2.3. For the collisional frequency both collisions between electrons and ions, and electrons and neutrals are considered, with the following expressions for the collisional frequencies [47]:

$$\nu_{ei} = 3,9 \cdot 10^{-6} n_i Z_i^2 \frac{ln\Lambda}{T_{e0}^{\frac{3}{2}}} \tag{3.2}$$

$$\nu_{en} = \sigma_n n_n v_{th,e} \tag{3.3}$$

always with all the quantities already defined in section 2.3. Solving the equations system 3.1, it is obtained a II order vector differential equation that is:

$$\delta\nabla \times \nabla \times \vec{B} - k\nabla \times \vec{B} + k_w^2\vec{B} = 0 \tag{3.4}$$

where k is the parallel wave number, k_w is the whistler wave number defined as $k_w = k_s\delta$ with $k_s = \omega_p/c$ ("skin number"), with c the speed of light, and the δ parameter is defined as:

$$\delta = \frac{\omega + i\nu}{\omega_c} \tag{3.5}$$

where ω is the feeding angular frequency, ν is the collisional frequency and ω_c is the cyclotron angular frequency ($\omega_c = 2\pi f_c$ where f_c is the electron cyclotron frequency). Assuming that the solution of this differential equation 3.4 is such that the wave magnetic field rotor is parallel to the magnetic field itself by means of the total wave number β, that is $\nabla \times \vec{B} = \beta\vec{B}$, the differential equation 3.4 can be factorized as follow, resulting in a II order algebric equation:

$$(\beta_1 - \nabla\times)(\beta_2 - \nabla\times)\vec{B} = 0 \tag{3.6}$$

$$\delta\beta^2 - k\beta + k_w^2 = 0 \tag{3.7}$$

This equation has the solutions already computed in section 2.3 that are:

$$\beta_1 = \frac{k_w^2}{k} \qquad \beta_2 = \frac{k}{\delta} \tag{3.8}$$

These two waves are both propagating in the plasma when the electron inertia is mantained in the model and they are coupled at the edge (for a constant density profile) or in the plasma region (for a radial non uniform density profile). Relative amplitudes of the waves can be calculated considering the boundary conditions for both the waves. TG waves have typically lower amplitudes

in the plasma center, but their amplitude is higher at the plasma boundary where they contribute strongly to the absorption of the wave energy from the plasma. The previous II order algebraic equation 3.7 for propagating waves in a collisional magnetized plasma can be rewritten as:

$$k = \frac{\delta}{\beta}(\beta^2 + k_s^2) \tag{3.9}$$

From this equation 3.9 and considering that k is a real number as made in [23, 24], a maximum value k_{max} for the parallel wave number is obtained assuming that the parallel wave number k is equal to the total wave number β and also a minimum value k_{min} is obtained differentiating the previous relation with respect to the total wave number β, and they are:

$$k_{min} = 2\delta k_s \qquad k_{\max} = \beta \tag{3.10}$$

This interval for k is considered for the computation of the optimal antenna length. In agreement to [24], the plasma-antenna resistance, a measure of how much power is transferred from the antenna to the plasma, is computed as:

$$R_A(m, L_a) = \int_{-\infty}^{+\infty} P_k(k, m, L_a)dk \tag{3.11}$$

where P_k is the spectral plasma-antenna resistance,

$$P_k(k, m, L_a) = S_k(k, m)p_A(k, m, L_a) \tag{3.12}$$

where S_k is the specific power density (independent from the antenna) and p_A is the antenna power density, m is the azimuthal mode number of the helicon wave and L_a is the antenna length. The power transferred from the antenna to the plasma is computed as the plasma Joule heating, in agreement to the following formula [24]:

$$P = \int \frac{1}{2}\vec{E}^* \vec{J}_{plasma} dV = \frac{|I_0|^2}{2}(R_A + iX_A) \tag{3.13}$$

where R_A and X_A are the plasma-antenna resistance and reactance, respectively. The simplified assumption made here with respect to [24] is that the main terms in the S_k expression are the ones strongly linked to the wave dispersion relation and they can be approximated with the following expression, unless scaling factors and terms slowly varying with k:

$$S_k(k, m) \approx |\frac{p_m(a, b, c, k)}{D(a, c, k)}|^2 \tag{3.14}$$

where here a is the plasma radius (assumed here equal to the inner quartz tube radius), b is the antenna radius and c is the external conductive wall radius (chosen equal to ten times the plasma radius to neglect the wall influence [24]), p_m is a geometric function (independent from the plasma properties) and D is the plasma dispersion function (independent from the antenna properties) and they have the following expressions:

$$p_m(r) = \frac{K'_m(Tr)I'_m(Tc) - K'_m(Tc)I'_m(Tr)}{K_m(Ta)I'_m(Tc) - K'_m(Tc)I_m(Ta)} \tag{3.15}$$

$$D(a,c,k) = F_1G_2 - F_2G_1 \tag{3.16}$$

with $F_{1,2}$ and $G_{1,2}$ that are defined as [24]. The first factor S_k in the equation 3.12 is only function of the parallel wave number k, having here selected the propagation mode $m = 1$ that is the expected propagating helicon mode in agreement with the measures [23, 24, 27]. The second factor p_A in the equation 3.12 depends from the product kL_a, being calculated from the Fourier transform of the antenna current density ($K_\phi(k, m, L_a)$) in agreement with the following expression [24]:

$$p_A(k,m,L_a) = \frac{1}{I_0^2}|K_\phi(k,m,L_a)|^2 \tag{3.17}$$

where I_0 is the antenna current. $K_\phi(k, m, L_a)$ depends from the antenna geometry and from the considered azimuthal mode number [24]. For a Nagoya type-III antenna with no windings ($\theta = 0$) and propagating mode $m = 1$, the Fourier transform of the current density has the following expression:

$$K_\phi(k,m,L_a) = -\frac{2}{\pi}I_0 sin(\frac{kL_a}{2}) \tag{3.18}$$

this is a periodic function that is maximized for a periodic value of the product $kL_a = \pi(2h+1)$, wher h is an integer number (with $h = 0$ for the minimum antenna length). Therefore the first optimal antenna length is computed maximizing the plasma-antenna resistance (equation 3.11) where in the integration the parallel wave number k is varied from its minimum to its maximum value (equation 3.10).

3.3.2 Design method 2

A second design method, taken as comparison, is the one considered in a first study on the Nagoya type-III antenna [26]. Assuming the Landau damping hypothesis, in agreement to which the wave phase velocity is almost equal to the velocity of the primary electrons contained in the neutral gas and, being these at velocity slightly lower, it is possible to have an acceleration of the electrons that leads to the gas ionization for electrons-ions collisions. Although the physics of the Landau damping does not have experimental confirmation in the helicon discharge, this design method is considered because it was the first and the well known design method published in literature for the Nagoya type-III antenna [26] and also because it is still used in literature [48]. It is assumed also that the plasma is an electron uniform single specie fluid and the electron inertia is neglected. The Argon gas is considered completely ionized, ions are at rest, the plasma is in steady state harmonic regime with waves represented as $\exp(i(m\theta + kz - \omega t))$ and the magnetic confinement field is in the axial direction ($\vec{B} = B_0\hat{z}$). It is assumed also that the antenna radius is equal to the quartz tube radius ($b = a$). The main assumptions used in this design method are: the parallel phase velocity ω/k is equal to the primary electrons thermal velocity, the dispersion relation for a non collisional uniform plasma is $\alpha = (\omega/k)(\mu_0 e n_{e0}/B_0)$ and the electron energy E_e, measured in eV, of the primary electrons interacting with the helicon wave is fixed from the dispersion relation, assuming given B_0, n_{e0} and a. The first assumption implies that the phase velocity is function of the electron energy E_e, in agreement to the following relation [26]:

$$\frac{\omega}{k} = 5,93\ 10^5 E_e^{\frac{1}{2}} \tag{3.19}$$

In addition, in the dispersion relation it is assumed that the total wave number α is almost equal to the transversal wave number $T = 3,83/a$ (for the propagating mode m = 1) that is determined from the boundary condition $B_r(r = a) = 0$, leading to the following expression for the dispersion relation [26]:

$$\frac{B_0}{n_{e0}} = 31,2 * 10^{-21} E_e^{\frac{1}{2}} a \tag{3.20}$$

In the end, the antenna length is computed assuming that is equal to $\lambda/2$, where λ is the plasma longitudinal helicon wavelength, and it is given from the following relation:

$$L_a = \frac{\pi}{k} = \frac{5,93 * 10^5 \pi E_e^{\frac{1}{2}}}{\omega} \tag{3.21}$$

where the primary electrons energy E_e must satisfy the equation 3.20. This design method, when the electron energy E_e is considered as input, has the disadvantage to assume an arbitrary value for this energy. Unlike the original article [26], where the electron energy was taken close to the peak energy of the gas ionization cross section, here this energy is derived from the dispersion relation of the helicon waves (equation 3.20), having fixed the plasma parameters and the antenna geometry, losing the dependence of the design method from the gas properties. Moreover, from an experimental point of view, this method has less foundation because the existence of the accelerated primary electrons by Landau damping has not been confirmed experimentally [49].

3.3.3 Design method 3

A third method is also considered for comparison. It is assumed also here that the plasma is an electron uniform single specie fluid and it is neglected the electron inertia. The Argon gas is completely ionized, ions are at rest, the plasma is in steady state harmonic regime with waves represented as $\exp(i(m\theta + kz - \omega t))$ and the confinement magnetic field is in the axial direction ($\vec{B} = B_0\hat{z}$). It is assumed also that the antenna radius is equal to the quartz tube radius ($b = a$). The boundary condition $B_r(Ta) = 0$, valid for a conductive and insulating wall, implies the computation of the first zero of the Bessel function of the first type ($J_1(Ta) = 0$ for the mode $m = 1$), and it provides a geometrical relation between the quartz tube radius or the plasma radius (a) and the transversal wave number (T), that is:

$$T = \frac{3,83}{a} \tag{3.22}$$

Therefore, when the quartz tube radius a is given, the transverse wave number is fixed. The antenna length is defined imposing a periodic perturbation on a cylindrical plasma with the same wavelength of the excited plasma mode. In agreement with the explanation given by Chen [26] on the coupling between the antenna and the mode, the Nagoya type-III antenna is capable to induce in the plasma a strong transverse electric field with a phase inversion between the two final antenna rings, allowing the coupling of the plasma mode with the same wavelength. In this physical representation the following general condition is imposed for a forced periodic oscillation in the

plasma:

$$L_a = \frac{(2n+1)}{2}\lambda, \qquad n = 0, 1, 2, 3 \tag{3.23}$$

where λ is the longitudinal helicon wavelength. Considering the quadrature relation for the total wave number (α) and the helicon dispersion relation for a uniform plasma, the following system of equations can be obtained:

$$\begin{cases} \alpha^2 = T^2 + k^2 \\ \alpha = \frac{\omega}{k}\frac{\mu_0 e n_0}{B_0} = \frac{\omega}{k}\frac{\omega_p^2}{\omega_c c^2} \end{cases} \tag{3.24}$$

The resulting equation of this system of equations is a IV order biquadratic algebric equation in α:

$$\alpha^4 - T^2\alpha^2 - \frac{\omega^2\omega_p^4}{\omega_c^2 c^4} = 0 \tag{3.25}$$

this equation can be solved analytically with the following formula:

$$\alpha = \pm\sqrt{\frac{T^2 + \sqrt{T^4 + 4\frac{\omega^2\omega_p^4}{\omega_c^2 c^4}}}{2}} \tag{3.26}$$

Now, considering the dispersion relation for the helicon wave in a non collisional plasma that can be rewritten as follow:

$$k = \frac{\omega}{\alpha}\frac{\omega_p^2}{\omega_c c^2} \tag{3.27}$$

it can be computed, from the general condition (equation 3.23) with $n = 0$ (antenna minimal length), the antenna length as function of the plasma longitudinal helicon wavelength:

$$L_a = \frac{\lambda}{2} = \frac{\pi}{k} \tag{3.28}$$

where it is considered $\lambda = 2\pi/k$. Therefore this method allows to define the cylindrical geometry of the Nagoya type-III antenna using as input the plasma state (n_{e0}, B_0) in which the helicon waves are supposed to be, the feeding angular frequency (ω) and the quartz tube radius (a).

3.3.4 Simulations for the design of the helicon antenna

The three previous sizing methods are compared with numerical results obtained from full-wave 3D electromagnetic simulations made with a finite elements solver (FEM) based on the MATLAB Partial Differential Equation Toolbox [36]. This solver is used to solve the Maxwell equations in an equivalent dielectric medium for a 3D geometry, allowing to simulate the antenna electromagnetic coupling and the helicon waves propagation in the magnetized plasma [31]. In these simulations, the plasma is modeled as an anisotropic conductive medium with complex electrical permittivity assigned in a tensorial form, in agreement to the cold plasma dielectric tensor given by Stix [50] with collisional corrections [2, 51], that has the following expression:

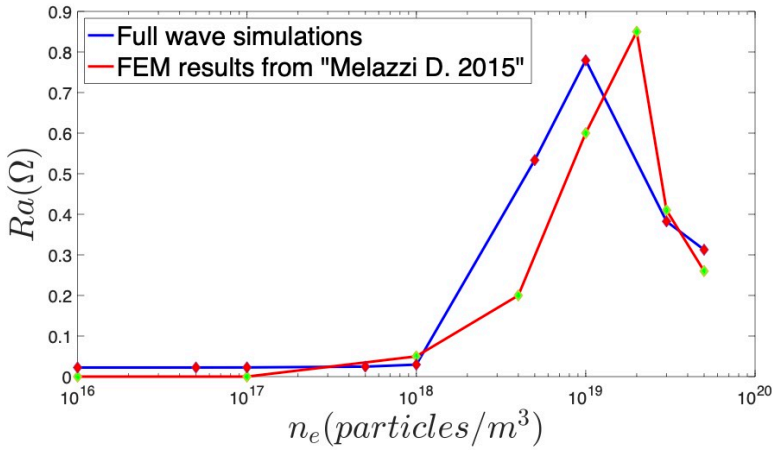


Figure 3.2: Comparison of the antenna resistance values for the validation of the FEM code used in this work. ($B_0 = 100mT$, $p_n = 2Pa$, $b = 3cm$, $L_a = 5cm$, $T_e = 3eV$, $f = 15MHz$,[2])

$$\varepsilon = \begin{bmatrix} S & jD & 0 \\ -jD & S & 0 \\ 0 & 0 & P \end{bmatrix}. \tag{3.29}$$

where the analytical expressions for the tensor elements S, D and P are:

$$\begin{cases} S = 1 - \sum_{a=e,i} \frac{\omega_{p,\alpha}^2(\omega - j\nu_\alpha)}{\omega[(\omega - j\nu_a)^2 - \omega_{c,\alpha}^2]} \\ D = \sum_{a=e,i} \frac{\sigma_\alpha \omega_{c,\alpha}}{\omega} \frac{\omega_{p,\alpha}^2}{(\omega - j\nu_a)^2 - \omega_{c,\alpha}^2} \\ P = 1 - \sum_{a=e,i} \frac{\omega_{p,\alpha}^2}{\omega(\omega - j\nu_\alpha)} \end{cases} \tag{3.30}$$

where the subscript α refers to the species that form the plasma, $\omega_{p,\alpha}$ is the angular plasma frequency, $\omega_{c,\alpha}$ is the angular cyclotron frequency, $\sigma_\alpha = \pm 1$ is the particle charge sign and ν_α is the collisional frequency. The numerical code has been validated comparing the obtained results with the ones from a previous study [2]. In this validation phase, the geometry of the Nagoya type-III antenna and the plasma parameters are selected as in [2], with inner quartz tube radius $a = 2cm$, external quartz tube radius $b = 3cm$ (equal to the antenna radius), tube thickness $t = 1cm$. The antenna length is assumed equal to $L_a = 5cm$, the plasma is confined with a magnetostatic field equal to $B_0 = 100mT$ with an electron temperature $T_{e0} = 3eV$, a neutral pressure $p_n = 2Pa$ and a neutral temperature $T_n = 298K$. The RF feeding power is provided at a frequency equal to $f = 15MHz$ with a feeding voltage of $V = 1V$ under condition of ideal impedance matching (as in [2]). The obtained results are in good agreement with [2] as shown in figure 3.2.

Starting from this 3D simulation model, a full-wave parametric simulation in the antenna length (L_a) has been performed to evaluate the real part of the antenna impedance. There are considered three simulations cases. The first case is the reference case with discharge parameters typical of the helicon wave ($n_{e0} = 1,0 \cdot 10^{18} particles/m^3$,$B_0 = 10mT$), called "Case 1". The second case is a simulation with a higher plasma density ($5 \cdot 10^{18} particlese/m^3$) with respect to the reference case, called "Case 2". The third case, called "Case 3", is a simulation with a higher magnetic field ($15mT$) with respect to the reference case. The considered parameters for the design of the Nagoya type-III antenna in the three simulation cases are reported in table 3.1. The simulation results for

the three simulation cases are reported in figure 3.3, 3.4 and 3.5. These graphs show a clear peak of the antenna-plasma resistance corresponding to the first optimal length of the Nagoya type-III antenna.

Table 3.1: Design parameters of the helicon antenna

	Case 1	Case 2	Case 3
Specie	Argon	Argon	Argon
f	13,56 MHz	13,56 MHz	13,56 MHz
B_0	10 mT	10 mT	15 mT
n_{e0}	$1,0 * 10^{18} \frac{particles}{m^3}$	$5,0 * 10^{18} \frac{particles}{m^3}$	$1,0 * 10^{18} \frac{particles}{m^3}$
T_{e0}	3 eV	3 eV	3 eV
p_n	2 Pa	2 Pa	2 Pa
b	4,5 cm (antenna)	4,5 cm (antenna)	4,5 cm (antenna)
a	4 cm (quartz tube)	4 cm (quartz tube)	4 cm (quartz tube)

For each simulation case, the optimal antenna length computed from full-wave simulations is compared with the one computed with the three design methods mentioned and the corresponding values are reported with vertical lines in figure 3.3, 3.4 and 3.5. In table 3.2 are reported all the comparisons between the antenna lengths, and also the relative error (in percentage) with respect to the reference antenna length from full-wave simulations and the mean relative error among the three cases for each method. Relatively to the design method 1, in figure 3.6, it is reported the contour plot of the S_k function in the Gauss plane, showing different peaks of the S_k function, each one corresponding to different propagating helicon modes. Therefore it is possible to observe that more than one propagating helicon mode is allowed for each simulation case. The design method 1 seems the more accurate in the evaluation of the optimal length, indeed it has the lowest mean relative error among the three simulation cases. In addition it is observed that in the second simulation case, the simpler method design method 3 is capable of predicting the optimal length with the least error. This good prediction capability of the last method is linked to the high electron density of the Case 2 for which it is known that [23, 24] the simple uniform plasma model, without taking into account of the coupling with the TG wave, is a quite accurate description for the helicon waves.

Table 3.2: Comparison of the three design methods

-	*Case* 1	*Case* 2	*Case* 3	Mean error
Method 1	13,50 cm (27,36%)	4,20 cm (-12,5%)	17,40 cm (-15,53%)	18,46 %
Method 2	17,52 cm (65,28%)	3,5 cm (-27,08%)	26,28 cm (27,57%)	39,98 %
Method 3	19 cm (79,25%)	4,38 cm (-8,75%)	26,5 cm (28,60%)	38,87 %
Simulated	10,60 cm	4,80 cm	20,60 cm	-

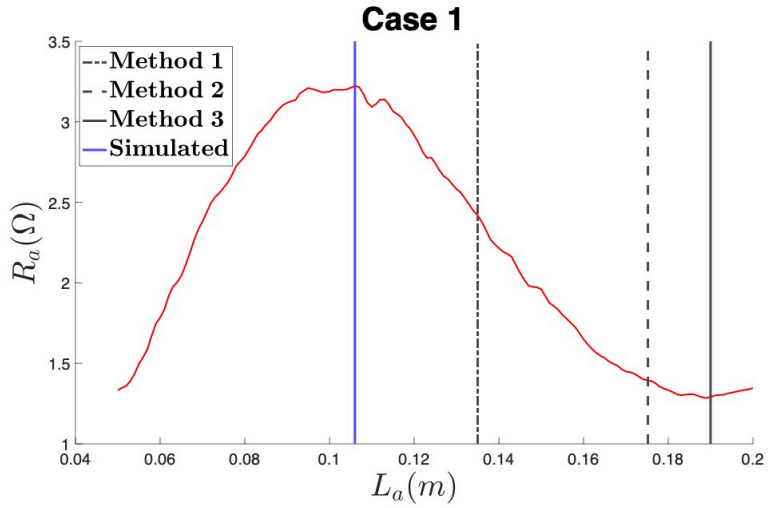


Figure 3.3: The antenna-plasma resistance (R_a) computed as function of the antenna length (L_a) (Case 1)

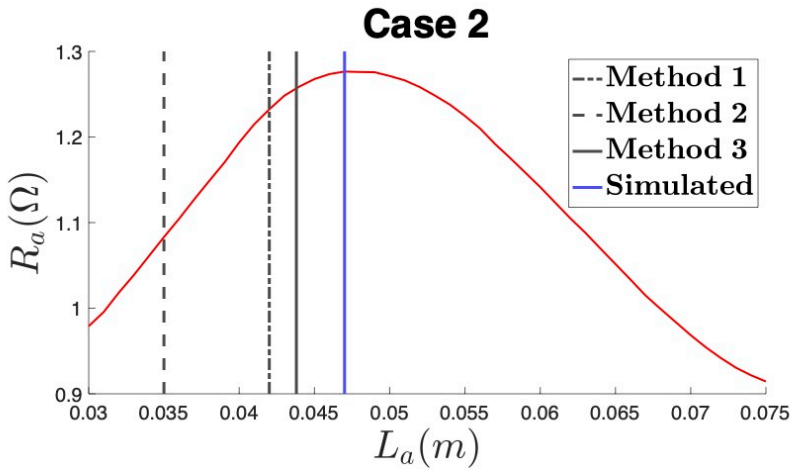


Figure 3.4: The antenna-plasma resistance (R_a) computed as function of the antenna length (L_a) (Case 2)

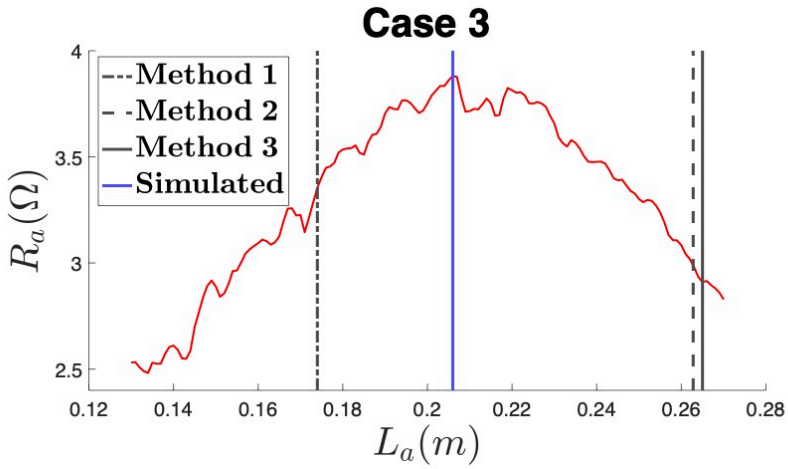


Figure 3.5: The antenna-plasma resistance (R_a) computed as function of the antenna length (L_a) (Case 3)

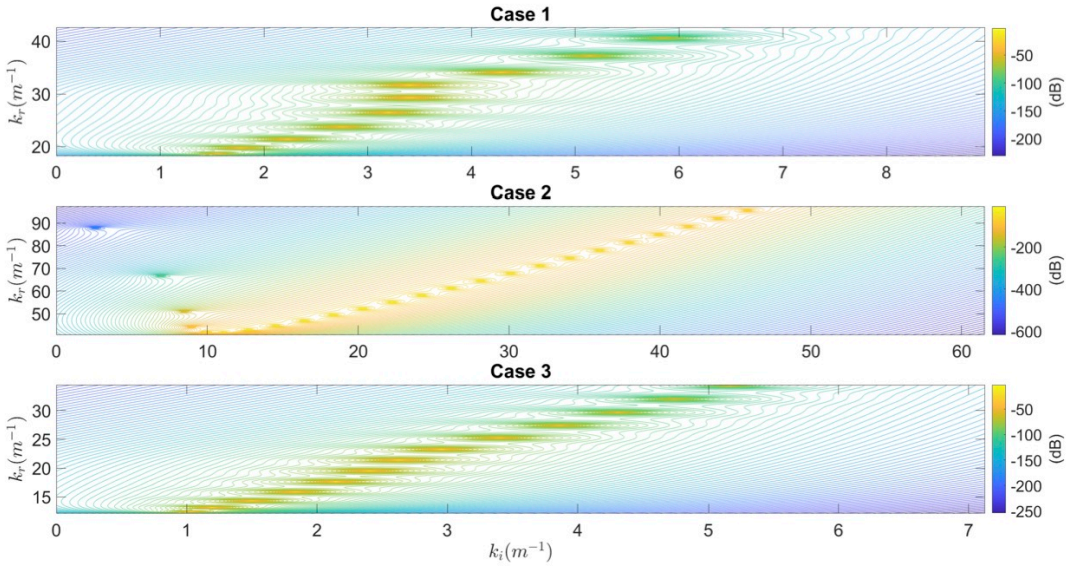


Figure 3.6: Modulus (in dB) of the S_k function in the Gauss plane, for the three simulation cases

3.4 Design, FEM and PIC simulations of the helicon thruster

It is proposed in this paragraph a 0-D global design model of the helicon thruster to find the main operative conditions of the thruster, starting from a reference propulsive performance defined in terms of specific impulse and thrust. These operative conditions are tested with dedicated simulations on the electromagnetic plasma-wave interaction inside the ionization chamber, and on the electrostatic plasma acceleration inside the magnetic nozzle. The first are made with a finite elements electromagnetic code that confirms the technical feasibility of the identified operational RF power with a predefined chamber geometry. The last are performed with a particel-in-cell electrostatic code that allows to estimate more precisely the performance reached by the thruster. The simulated thruster has a sub-optimal design, with an absorbed plasma power of almost 1 kW, a thrust of almost 10 mN and a specific impulse higher than 1000 s. The design and simulation model of the thruster conceived will be the basis for a successive optimization of the thruster geometry and of its operational conditions, with the final aim to design and test a prototype of a new helicon thruster.

The helicon thruster is an electric thruster relatively new in which the thrust is produced by accelerating a propulsive plasma with a magnetic nozzle. The plasma is obtained by coupling radiofrequency power (RF) through helicon waves inside an ionization chamber (an isolating tube where the propellant is injected) using a special type of antenna, known as helicon antenna [26], that is wrapped around the tube. The helicon thruster is an electrodeless thruster that ionizes the propellant without electrodes and it does not require an external cathode to neutralize the emitted jet, that is already globally ambipolar. This simplify the design and it allows to have a lighter thruster that is not exposed to cathodic polverization (sputtering) and therefore it is characterized by a longer lifetime. The ionization mechanism is already tested experimentally and the helicon thrusters are designed to be mounted on small satellites with feeding powers from some hundreds of Watts up to kiloWatts and thrust levels from some milliNewtons up to Newton. The main objective of this paragraph is to model the entire thruster, simulating the plasma both inside the ionization

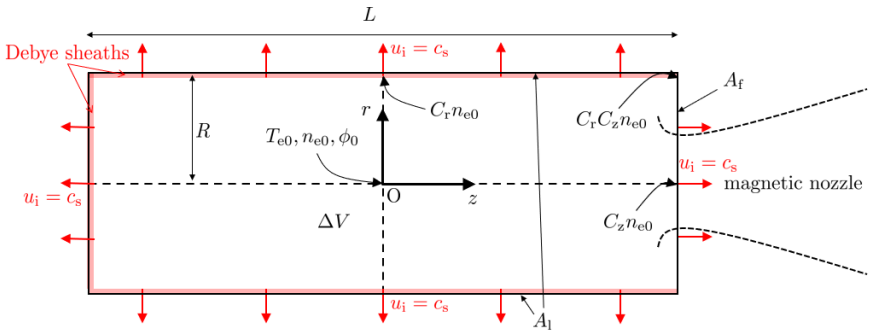


Figure 3.7: Geometry of the ionization chamber, with highlighted the considered plasma parameters and the quasi-neutral plasma density values in the relevant positions

chamber of the helicon thruster and inside the magnetic nozzle, to estimate the global propulsive performance of the device.

First of all, a 0-D global performance model is introduced to determine a first solution of the sub-optimal operative conditions (electron temperature, mass flow rate, plasma mean density and neutral mean density), as function of the thruster objective performance (mainly thrust, specific impulse and total operative RF power). Once the mean plasma density and the source electron temperature are known, the electromagnetic antenna-plasma interaction is modeled with a full-wave approach, with the aim to design in a realistic geometry the necessary antenna to couple the corrected power with the plasma. In particular, the coupling between the helicon antenna with the plasma is solved using an electromagnetic code based on a 3D finite elements method (FEM), taking into account for a realistic geometry both of the antenna structure and of the ionization chamber. The plasma is modeled as a anisotropic and homogeneous conductor with electrical permittivity given by the Stix dielectric tensor [50] with collision corrections. The electron-ion and electron-neutral collisions in the plasma electric tensor are considered using corrective terms proportional to the collisional frequency [2, 51]. This is equivalent to consider the plasma as a conductive fluid, anisotropic, locally inhomogeneous and collisional, magnetized by an external magnetostatic field. The cold plasma approximation is considered valid in the description of the fast waves propagation (helicon waves) in the cold plasma of the helicon thruster [2, 51]. While it is shown that a non uniform magnetic field can be relevant to an accurate estimate of the wave absorption [51], in these full-wave simulations a constant and uniform axial field is considered, due to its negligible space variation inside the ionization chamber (with a low aspect ratio R/L).

Performed the electromagnetic simulations, the plasma properties in the exit section of the thruster are given to the particle-in-cell code (PIC), called PICCOLO (PIC Code of LOw temperature plasma discharges), that simulates the entire magnetic expansion in the nozzle, therefore estimating the produced thrust force. PICCOLO is based on a electrostatic PIC technique, in which ions and electrons are simulated as macro particles subjected to the Newton equation and their charge is weighted in the nodes of a dedicated mesh (from here the name particle-in-cell) to obtain the space distribution of the electric charge density [52]). This is solved by a Poisson equation solver to obtain the consistent electric field used to advance the charged particles to the next time step.

3.4.1 0-D global design model

To have a first sizing of the helicon plasma thruster, a 0-D equilibrium model is used to compute the operative parameters as the electron density n_{e0}, the electron temperature T_{e0} inside the plasma source, and the total mass flow rate $\dot{m}$. This 0-D model assumes:

- a given thrust force F of the thruster, as design parameter
- a given specific impulse Isp of the thruster, as design parameter
- a given geometry of the ionization chamber, defined in terms of its radius R and of its length L. Such geometrical parameters can be changed in an iterative computation for the global optimization of the thruster. However this procedure is not followed here, until there is a good correspondence between sizing and simulation, and it is postponed to a successive work.

The total mass flow rate of the thruster can be directly estimated from the objective parameters as:

$$\dot{m} = \frac{F}{g_0 Isp} = \frac{F}{\eta_m u_{z,i}} \tag{3.31}$$

where Isp is the specific impulse in unit of time, g_0 is the standard gravity acceleration, $u_{z,i}$ is the ion axial velocity (at infinity) and $\eta_m = \dot{m}_i/\dot{m}$ is the propellant utilization efficiency. In this equation it is assumed a neutrals exit velocity negligible (compared to the ions that are typically 10-20 times faster).
From the energy conservation of a charged particle through the expansion in the magnetic nozzle, the final exit velocity of the ions from the predicted electric potential drop $\Delta\phi_{MN}$ can be computed. Indeed, in a magnetic nozzle, the thermal electron energy is transformed directly in ion kinetic energy:

$$\frac{1}{2} m_i u_{z,i}^2 = e\Delta\phi_{MN} \tag{3.32}$$

$$\Delta\phi_{MN} = \frac{T_{e0}}{e}(-\ln\sqrt{\frac{2\pi m_e}{m_i}} + 0.5) = \frac{C_{shd} T_{e0}}{e} \tag{3.33}$$

where T_{e0} is the electron temperature (in unit of energy), $C_{shd} \approx 5$ is a dimensionless constant dependent from the electron over ion mass ratio, and the factor 0.5 models the ion acceleration in the pre-sheath inside the ionization chamber (where ions are still subsonic). The equation 3.33 represents the electric potential drop on a classical Debye sheath, that is actually a conservative approach, as shown in recent studies that suggest higher potential drops [53]. Combining the equations 3.32 and 3.33, and knowing that $g_0 Isp \approx \eta_m u_{z,i}$,is possible to obtain a conservative estimation of the electron temperature required to reach the objective specific impulse:

$$T_{\mathrm{e0}} = \frac{1}{2}\frac{m_{\mathrm{i}}}{\eta_{\mathrm{m}}^2 C_{\mathrm{shd}}}(g_0 Isp)^2. \tag{3.34}$$

Referring to the figure 3.7, and assuming that the plasma is singularly ionized, quasi-neutral everywhere (exception made at the Debye sheath close to the walls), and that ions exit from the

ionization chamber with the Bohm velocity (or sonic velocity), the mean plasma density at the exit section $\bar{n}_{ef}$ can be estimated [31]:

$$\dot{m}_{\mathrm{i}} = m_{\mathrm{i}} \bar{n}_{\mathrm{ef}} c_{\mathrm{s}} A_{\mathrm{f}} = m_{\mathrm{i}} \bar{n}_{\mathrm{ef}} A_{\mathrm{f}} \sqrt{\frac{T_{\mathrm{e0}}}{m_{\mathrm{i}}}}, \tag{3.35}$$

where $c_s = \sqrt{T_{e0}/m_i}$ is the sonic ion velocity and $A_f = \pi R^2$ is the exit cross section. This 0-D model assumes symmetric and quadratic decay along z and r of the plasma density n_e from the center of the chamber. This means that [31]:

$$\begin{aligned} n_{\mathrm{e}}(r,z) &= n_{\mathrm{e0}} \left[\left(\frac{1}{(1-C_{\mathrm{r}})} - \frac{r^2}{R^2} \right) (1-C_{\mathrm{r}}) \right] \left[\frac{4}{L^2} (C_{\mathrm{z}}-1) z^2 + 1 \right] = \\ &= n_{\mathrm{e0}} \left[\frac{4}{L^2} \frac{(C_{\mathrm{z}}-1)(C_{\mathrm{r}}-1)}{R^2} r^2 z^2 + \frac{(C_{\mathrm{r}}-1)}{R^2} r^2 + \frac{4}{L^2} (C_{\mathrm{z}}-1) z^2 + 1 \right], \end{aligned} \tag{3.36}$$

where n_{e0} is the plasma density in the center of the ionization chamber ($r = 0, z = 0$), and C_r, C_z are constants that can be obtained from 1D PIC simulations of the plasma-wall interaction. In particular, for Argon ions and a non collisional plasma without electron emission from the walls, the ratio between the density at the plasma edge and the peak density at the symmetry point (cylinder axis) are assumed as $C_z = 0.5$ (that corresponds to a non magnetized case) and $C_r = 0.35$.
The following mean plasma densities are introduced: the mean plasma density in the chamber $\bar{n}_e$, the mean lateral density $\bar{n}_{e,l}$ at $r = R$, and the mean density over the exit section $\bar{n}_{e,f}$ at $z = L/2$, computed as:

$$\bar{n}_{\mathrm{e}} = \frac{1}{V} \iint_{r,z} n_{\mathrm{e}}(r,z) 2\pi r dr dz = 2 n_{\mathrm{e0}} \left[\frac{(C_{\mathrm{z}}-1)(C_{\mathrm{r}}-1)}{12} + \frac{(C_{\mathrm{r}}-1)}{4} + \frac{(C_{\mathrm{z}}-1)}{6} + \frac{1}{2} \right], \tag{3.37}$$

$$\bar{n}_{\mathrm{e,l}} = \frac{1}{A_{\mathrm{l}}} \int_{z=-L/2}^{L/2} n_{\mathrm{e}}(r=R,z) 2\pi R dz = C_{\mathrm{r}} \left[(C_{\mathrm{z}}-1) \frac{1}{3} + 1 \right] n_{\mathrm{e0}}, \tag{3.38}$$

$$\bar{n}_{\mathrm{e,f}} = \frac{1}{A_f} \int_{r=0}^{R} n_{\mathrm{e}}(r, z=L/2) 2\pi r dr = C_{\mathrm{z}} \left[(C_{\mathrm{r}}-1) \frac{1}{2} + 1 \right] n_{\mathrm{e0}}, \tag{3.39}$$

where ΔV is the ionization chamber volume, and $A_l = 2\pi RL$ is the total lateral surface. Therefore, combining the equations 3.35 and 3.39, the peak plasma density n_{e0} can be obtained as function of the required mass flow rate:

$$n_{\mathrm{e0}} = \frac{1}{C_{\mathrm{z}} \left[(C_{\mathrm{r}}-1) \frac{1}{2} + 1 \right]} \sqrt{\frac{m_{\mathrm{i}}}{T_{\mathrm{e0}}}} \frac{\dot{m}_{\mathrm{i}}}{m_{\mathrm{i}} A_{\mathrm{f}}}. \tag{3.40}$$

A mean neutral density can be obtained equating the ion production rate in the volume with the ion lost rate through the lateral and frontal surfaces of the ionization chamber. Such equilibrium requires:

$$\bar{n}_{\mathrm{e}} \bar{n}_{\mathrm{n}} R_{\mathrm{ion}}(T_{\mathrm{e0}}) \Delta V = c_{\mathrm{s}} \left(\bar{n}_{\mathrm{e,l}} A_{\mathrm{l}} + 2 \bar{n}_{\mathrm{e,f}} A_{\mathrm{f}} \right) \tag{3.41}$$

where $R_{ion} =< \sigma_{ion} v_e >$ is the ionization velocity, it depends on the electron temperature,

that can be find integrating the ionization cross section over a maxwellian electron distribution. In particular, the ionization cross sections are obtained interpolating the data from the reference [54] for a given value of the electron temperature.
The electron temperature inside the chamber is estimated solving a power balance equation in which the source power is the deposited ohmic power in the plasma by the helicon waves, and the dissipated power is the power lost from the plasma through the three main dissipation mechanisms: particles lost towards the walls, gas ionization and neutral excitation. The first term is dominant and it can be estimated with a fitting law obtained from 1D PIC simultations of the plasma walls interaction in a partially magnetized scenario as this (where electrons are magnetized but ions not). In particular, knowing the mean plasma density at the plasma edge $\bar{n}_{e,l}$, $\bar{n}_{e,f}$ (depending from the considered surface), it is possible to estimate this power as [31]:

$$P_{\mathrm{wall}} = 2A_{\mathrm{f}} n_{\mathrm{e,f}} c_{\mathrm{s}} \gamma_{tot,f} T_{e0} + A_{\mathrm{l}} n_{\mathrm{e,l}} c_{\mathrm{s}} \gamma_{tot,l} T_{e0} \tag{3.42}$$

where γ_{tot} represents a total transfer coefficient of the energy (summing the contribution of electrons and ions) that depends from the considered surface and more precisely from the angle ψ between the magnetic field lines and the normal to the considered surface. In particular, $\psi = 0^o$ for the two frontal surfaces and $\psi \approx 89^o$ for the lateral surfaces (with an almost parallel incidence). In general, for cold ions ($T_{i0} = 0$), the following fitting can be used:

$$\gamma_{\mathrm{tot}} = \frac{5}{2} - \ln\left(\frac{\sqrt{\frac{2\pi m_{\mathrm{e}}}{m_{\mathrm{i}}}} C_\gamma(\psi, r_{\mathrm{Le}}/\lambda_{\mathrm{De}}, m_{\mathrm{e}}/m_{\mathrm{i}})}{\cos\psi} \right) \tag{3.43}$$

where C_γ is a parameter that, in general, depends from the magnetic field angle , from the ratio between the electron Larmor radius and the electron Debye length λ_{De} and from the ratio between the electron mass and the ion mass. In a plasma with Argon ions and an electron Larmor radius comparable with the Debye length ($\lambda_{De}/r_{Le} = O(1)$), it is obtained $C_{\gamma,f} = 1$ for the frontal surfaces ($\psi = 0$), and $C_{\gamma,l} = 0.4$ for the lateral surface ($\psi \approx 89^o$). Again, the previous fitting and the coefficients are obtained from 1D PIC simulations of a non emitting wall, interacting with a non collisional plasma, so that the effects of the secondary electrons and of the charged particles collisions with neutrals are neglected.
On the others two loss mechanisms, the ionization and excitation power expressions are the following:

$$P_{\mathrm{exc}} = \bar{n}_n \bar{n}_e R_{\mathrm{exc}}(T_{\mathrm{e0}}) E_{\mathrm{exc}} \Delta V, \tag{3.44}$$

$$P_{\mathrm{ion}} = \bar{n}_n \bar{n}_e R_{\mathrm{ion}}(T_{\mathrm{e0}}) E_{\mathrm{ion}} \Delta V, \tag{3.45}$$

where the reaction rates are obtained integrating on a electron maxwellian distribution the available cross section in [54, 55] for respectively ionization and excitation. The energy levels for ionization and excitation are respectively 15,76 eV and 11,5 eV for Argon.
The equilibrium temperature T_{e0} of the helicon thruster is then computed assuming a given absorbed power and equating it to the total power lost. This means that:

$$P_\Omega = P_{\mathrm{wall}}(T_{\mathrm{e0}}) + P_{\mathrm{ion}}(T_{\mathrm{e0}}) + P_{\mathrm{exc}}(T_{\mathrm{e0}}), \tag{3.46}$$

where the terms on the right side depend on the electron temperature. The objective absorbed power is then the necessary input for the full-wave finite elements model (described in the following paragraph), that has the aim to validate the design of a helicon antenna capable to give such plasma power.
The antenna helicon is designed in agreement to the helicon wave theory [26] and the design model presented in the previous paragraph: design method 3 of the helicon antennas. The helicon antenna is a Nagoya type-III antenna that ionizes a neutral gas immersed in a magnetostatic field through energy deposition. It is assumed, as stated from the previous equation 3.46, that the deposited energy in the plasma by the helicon waves is a fraction of the input RF power and it heats the plasma through Joule heating. The helicon antenna size is determined combining the quadrature relation of the total helicon wave number α and the plasma dispersion relation for the helicon waves in a magnetized plasma, as follow:

$$\begin{cases} \alpha^2 = k_\perp^2 + k_\parallel^2, \\ k_\parallel = \dfrac{\omega}{k} \dfrac{\omega_{\mathrm{p,e}}^2}{\omega_{\mathrm{c,e}} c^2}, \end{cases} \tag{3.47}$$

where $\omega_{c,e}$ is the electron angular cyclotron frequency, c is the speed of light and $\omega_{p,e}$ is the electron plasma angular frequency. From this linear system, the helicon wave number and its components are computed, that is the wave number α, the parallel wave number $k_\parallel$ and the transverse wave number $k_\perp$. Then, the antenna size is determined assuming that the antenna excites a propagating helicon mode in the magnetized plasma. The antenna is assumed of cylindrical shape and therefore it is determined from the antenna radius a and the antenna length L_a. The antenna radius a, is computed from the radius R of the ionization chamber, assuming a thickness of the ionization chamber equal to $5mm$. The design conditions for the Nagoya type-III antenna are:

$$\begin{cases} k_\perp = \dfrac{3.83}{R}, \\ L_{\mathrm{a}} = \dfrac{\lambda}{2}. \end{cases} \tag{3.48}$$

Therefore, once that the antenna shape (a, L_a) is chosen and the mean plasma density in the chamber $\bar{n}_e$ (equation 3.37) is known, the required magnetostatic field can be computed from the plasma dispersion relation in agreement to the following equation:

$$B_0 = \frac{\omega}{k_\parallel} \frac{\mu_0 e \bar{n}_{\mathrm{e}}}{\alpha} \tag{3.49}$$

and therefore the main output parameters of the 0-D model are completely determined.

3.4.2 Full-wave simulation model for the ionization chamber

The plasma in the ionization chamber is simulated with an in-house 3D FEM code that solves the Maxwell equations for a 3D realistic geometry in a cartesian reference system. The obtained full-wave solutions allow to compute the electromagnetic field coupled by the helicon antenna with the plasma and to estimate the power transferred from the helicon antenna to the plasma. The simulation model assumes that a feeding power (as computed in the 0-D model) is provided to the helicon antenna and a fraction of this power is absorbed by the plasma through collisional damping.

The plasma parameters (plasma density, neutral density, electron temperature) and the geometrical parameters (helicon antenna size and ionization chamber size) are selected in agreement with the 0-D model of the thruster already described in 3.4.1. The magnetostatic field, necessary to the propagation of the helicon wave, is derived from the dispersion relation of the helicon waves [26] 3.49.
The plasma, already ionized, is modeled as an anisotropic homogeneous conductor with electric permittivity given by the Stix electric tensor [50] with collisional corrections. Electron-ion and electron-neutral collisions are computed in agreement to the formula 3.2 and 3.3. For the considered case, $\nu_{ei} \approx 3.9MHz$ and $\nu_{en} \approx 4.2MHz$. Such frequencies are considered in the plasma electric tensor using corrective terms proportional to the collisional frequencies [2, 51]. The helicon electric field and the current density induced in the plasma are obtained from full-wave simulation results and they allow the computation of the deposited power in the plasma:

$$P_\Omega(T_e) = \frac{1}{2}\int_V Re(\vec{J}\cdot\vec{E}^*)dV \tag{3.50}$$

where $\vec{J}$ and $\vec{E}^*$ are complex vectors representing the current density vector and the conjugate complex of the helicon electric field vector and V is the volume of the ionization chamber. The deposited power P_Ω is the source power in the power balance equation used in the 0-D model for the evaluation of the electron temperature 3.46.
The main results obtained from the full-wave simulation are the verification of the helicon antenna design for the absorbed design power (as required by the 0-D model) and the computation of the exact input RF power level required for the desired antenna operative point. In the end the verification of the RF coupling with a propagating helicon mode in the magnetized plasma.

3.4.3 Particle-in-cell expansion model in the magnetic nozzle

The non collisional expansion within the magnetic nozzle is simulated with an electrostatic particle-in-cell code called PICCOLO. This choice is justified from the fact that much of the wave electromagnetic absorption takes place inside the ionization chamber because the helicon wave becomes evanescent in the nozzle, not far from the exit surface of the chamber. Ions and electrons macroparticles (each one representing a big number of elementary particles) are moved in agreement to the Newton equation and to the local electric and magnetic field $\vec{E}$ and $\vec{B}$:

$$m\frac{d\vec{v}}{dt} = q\left(\vec{E} + \vec{v}\times\vec{B}\right), \tag{3.51}$$

where m and q are the mass and the elementary particle charge. A classic leap-frog algorithm is used to advance the particles in time.
While the magnetic induction field is given as an input map (from the 0-D global model and from the antenna design costraints) and it is fixed in the simulation, the electrostatic field $\vec{E} = -\nabla\phi$ is obtained from the differentiation of the consistent electric potential ϕ, that is the solution of the Poisson equation in the considered cylindrical coordinates r and z:

$$\frac{1}{r}\frac{\partial\phi}{\partial r} + \frac{\partial^2\phi}{\partial r^2} + \frac{\partial^2\phi}{\partial z^2} = -\frac{e}{\epsilon_0}\left(n_\mathrm{i} - n_\mathrm{e}\right), \tag{3.52}$$

where n_i represents the Argon ion density singularly charged, and ϵ_0 is the vacuum electric

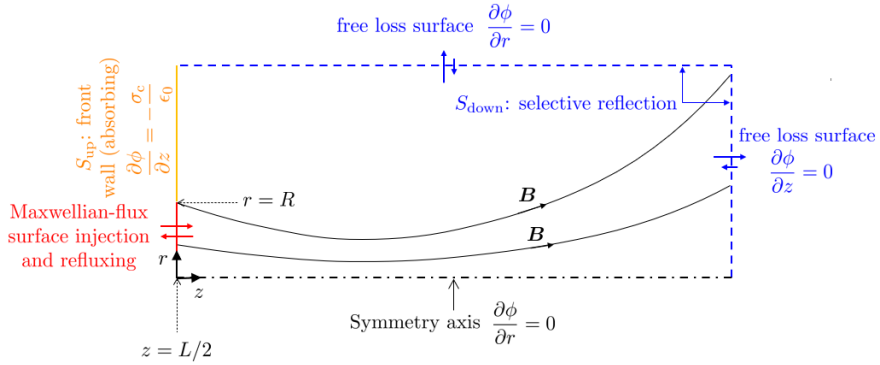


Figure 3.8: Particle-In-Cell simulation scheme for the magnetic nozzle, indicating the boundary conditions for the particles and the electric potential. The injection region is extended from $r = 0$ up to $r = R$. Notes that the graphed magnetic field is only qualitative and the simulations consider only the region where it is completey divergent.

permittivity. In the simulation collisions are not included neither with neutrals neither with charged particles (non collisional plasma model). The boundary conditions for macro-particles ions and electrons are shown in figure 3.8.

In particular, the domain starts at the exit section of the ionization chamber (with a radius R), and an ambipolar flux of ions and electrons is injected from the region that extends from $r = 0$ up to $r = R$ with a maxwellian velocity distribution [56], and a space distribution given from the parabolic radial profile of the equation 3.36. In $z = L/2$ and for $r > R$, it is assumed a dielectric material surface, with ions and electrons that are lost on that surface and they contribute to the local surface charge density σ_c. While the quasi-neutrality is automatically satisfied at the injection surface repelling all the particles that cross the injection surface ($z = L/2$, $r < R$) towards the source, at the open loss boundaries (dotted blu lines) all the ions are lost and the electrons are or reflected or not, depending on their mechanical energy E_{tot} (relative to infinity),

$$E_{\mathrm{tot}} = \frac{1}{2} m_{\mathrm{e}} v_{\mathrm{e}}^2 - e\left(\phi_{\mathrm{exit}} - \phi_{\infty}\right), \tag{3.53}$$

where v_e is the electron velocity, ϕ_{exit} is the local electric potential at the exit position, and ϕ_∞ is the potential at infinity. All the electrons with $E_{tot} < 0$ are specularly reflected back towards the simulation domain, while all the electrons with $E_{tot} > 0$ are lost and they charge a virtual capacitor at infinity, in agreement to:

$$\frac{\mathrm{d}\phi_{\infty}}{\mathrm{d}t} = \frac{I_{\mathrm{i}\infty} + I_{\mathrm{e}\infty}}{C_{\infty}}, \tag{3.54}$$

where $I_{i\infty}$, $I_{e\infty}$ are the ion and electron current that leave the domain at infinity, and C_∞ is an equivalent electric capacity.

3.4.4 Simulation results

Sizing results of the 0-D model

The global design model assumes an objective propulsive performance of the helicon plasma thruster, with a thrust of 12 mN and a specific impulse of 1200 s, with an absorbed plasma power of almost 1 kW. The main parameters of the 0-D global sizing model are reported in table 3.3. The reported data

are divided in input and output of the model. The antenna and the ionization chamber geometry are chosen to obtain the objective absorbed power. The 0-D model results are the inputs required for the full-wave and PIC simulations. Indeed, the thermodynamic state in terms of pressure, density and temperature of the plasma and neutrals, and also the size of the helicon plasma thruster and the magnetostatic field are provided as input to the electromagnetic simulation software to define the thruster geometry and to compute the solution of the helicon mode and the power transfer between the helicon antenna and the plasma. In particular, a magnetostatic field around 90 G is required and in this case it is generated with two coils of radius 12 cm positioned at the extremes of the ionization chamber and concentric with the ionization chamber axis ($z = \pm L/2$). The efficiency of the designed thruster is quite low ($4,3\%$), even if in line with literature values and considering that the 0-D model provides a conservative estimation of this figure, and higher values can be obtained through optimization. The thruster efficiency is computed as:

$$\eta_{\mathrm{t}} = \frac{F g_0 I_{\mathrm{sp}}}{2 P_{\mathrm{RF}}} \tag{3.55}$$

where P_{RF} is the total RF power provided in input to the helicon antenna, that is function of the plasma power absorbed in agreement to $P_\Omega = \eta_{RF} P_{RF}$ where η_{RF} is the transmission efficiency of the RF power (from the RF amplifier to the plasma). Here a conservative estimation equal to 70% is assumed. Note that η_t is the total efficiency of the thruster, considering the input power to the RF amplifier, while in some cases the thrust efficiency is referred only to the thrust chamber (with the plasma absorbed power at the denominator).

Input parameters	units	values
Chemical species	(-)	Argon
Feeding RF frequency	MHz	13,56
Thrust, F	mN	12
Specific impulse, I_{sp}	s	1200
Propellant utilization efficiency, η_m	(-)	0,85
RF power transmission efficiency, η_{RF}	(-)	0,70
Ionization chamber radius, R	cm	3
Helicon antenna radius, a	cm	3,5
Helicon antenna length, L_{a}	cm	12
Ionization chamber length, L	cm	12
Neutrals temperature	K	300
Output parameters	**units**	**values**
Electron temperature, T_{e0}	eV	7,667
Ion mass flow rate, $\dot{m}_{\mathrm{i}}$	mg/s	0,866
Peak electron density, n_{e0}	m^{-3}	$3,181 \cdot 10^{18}$
Mean electron density, $\bar{n}_{\mathrm{e}}$	m^{-3}	$1,790 \cdot 10^{18}$
Mean neutral density, $\bar{n}_{\mathrm{n}}$	m^{-3}	$2,256 \cdot 10^{19}$
Magnetostatic field, B_0	G	90
Deposited power in the plasma, P_Ω	W	1147,2
Total thrust efficiency, η_{t}	(-)	4,3 %

Table 3.3: Parameters considered in the global model for sizing the helicon thruster.

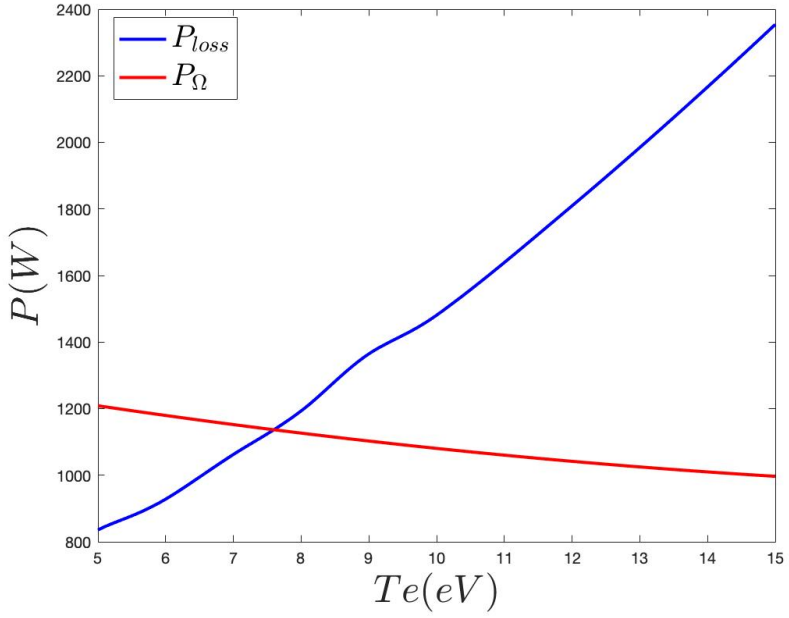


Figure 3.9: Graphical solution of the plasma power balance equation for the helicon thruster with an input RF power of almost 2kW

Full-wave simulation of the plasma-wave interaction

Full-wave simulations are made with a 3D electromagnetic in-house FEM code that, for a given geometry, is capable to simulate the electromagnetic wave field excited in the plasma by a helicon antenna. The considered geometry here is a Nagoya type-III antenna that is fed by a coaxial cable that connects the RF generator with the antenna feeding port, that is an aperture in one of the two antenna legs. When it is fed by a RF source, the Nagoya type-III antenna can excite a electromagnetic mode in the plasma that corresponds to a helicon wave propagating with poloidal number m = 1 [26] (as reported in figure 3.10). While helicon wave propagates, the wave deposits its power in the plasma through collisional damping and the plasma temperature is determined from the Joule heating. As stated previously, the ohmic power is computed from the volume integral of the scalar product between the current density vector and the conjugate complex of the electric field vector.
The operational point of the thruster is obtained adapting the input RF power of almost 2 kW to the objective electron temperature and this corresponds to the intersection between the deposited RF power and the total power lost when they are computed as function of the electron temperature, as shown in figure 3.9. Indeed, the intersection of the two curves is the steady state operational point of the helicon plasma thruster at the objective electron temperature (as computed from the 0-D model), i.e. where the deposited power in the plasma is equal to the total power lost.

Full Particle-In-Cell simulation of the magnetic nozzle

The PIC simulation of the magnetic nozzle considers the parameters summarized in table 3.4. The time step and the size of the cell are chosen to respect the PIC constraints on the Debye length, the plasma frequency and the cyclotron frequency [52]. Ions are injected with sonic velocity with a fluid velocity completely axial, and a temperature of 0,5 eV, representing a realistic velocity dispersion for

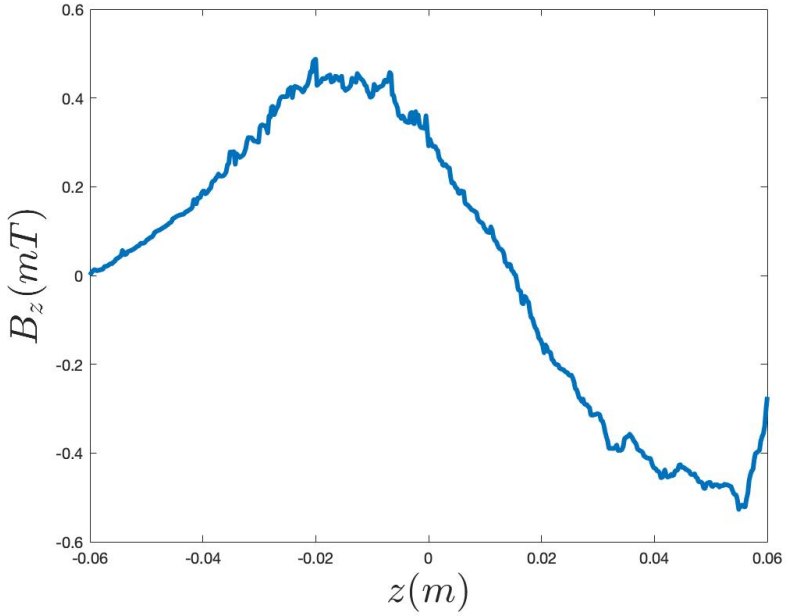


Figure 3.10: Longitudinal oscillation of the axial component of the helicon magnetic field (Bz)

the fact that they are created at different positions inside the ionization chamber. In the simulations an artificially augmented electric permittivity of a factor 9 is used to reduce the simulation cost, that corresponds to simulate a Debye length 3 times higher than the real one. However this should not impact the obtained results significantly, because the plasma is quasi-neutral everywhere and the total potential drop of the magnetic nozzle is not influenced from the value of ϵ_0, as shown in the equation 3.33.
The magnetic field intensity and the current lines are shown in figure 3.11. At the exit surface, the intensity is slightly lower than 90 G, and it decreases to some G downstream. The intensity peaks at the exit surface $r = 12cm$ is located there, because that is the radius of one of the two coils that generate this magneto-static field (the other coil is positioned at $z = -L/2$, i.e. at the other extreme of the ionization chamber).
The evolution in time of the potential at infinity is shown in figure 3.12. In particular, this represents the potential at infinity (equation 3.54) relative to the throat of the nozzle ($r = 0, z = L/2$) and its oscillations are mainly due to the PIC noise at the nozzle throat (the axisymmetric simulations axis is always affected by a large PIC noise [57]).

Neverthless, the absolute potential drop from the nozzle throat to infinity should tend asymptotically to the one predicted from the equation 3.33, that is around 40 V in this case. In this case, the predicted potential drop is slightly higher (approximately 50 V), because the equation 3.33 underestimates the total potential drop across the magnetic nozzle, as confirmed in other studies [53].

The 2D maps of different variables of interest are reported in figure 3.13. The electrostatic potential and the electric field (reported in subplot (a,b)) show clearly the magnetic nozzle effect, that is to reduce the divergence of the emitted jet focusing the ions axially.
The figure 3.13 (c,d) show the electron density and the electron temperature in the plane. Clearly,

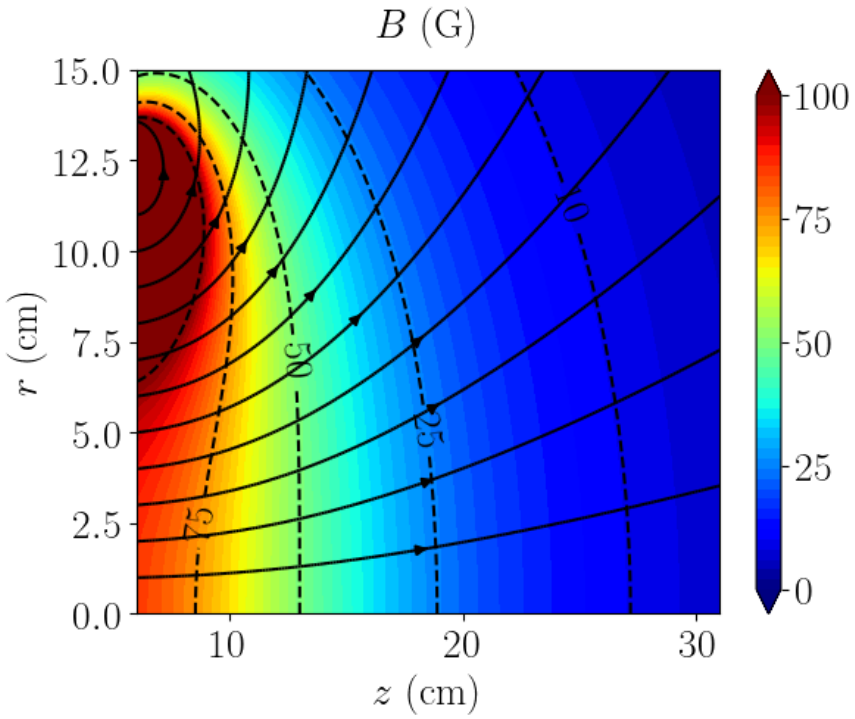


Figure 3.11: Magnetic induction field intensity and current lines

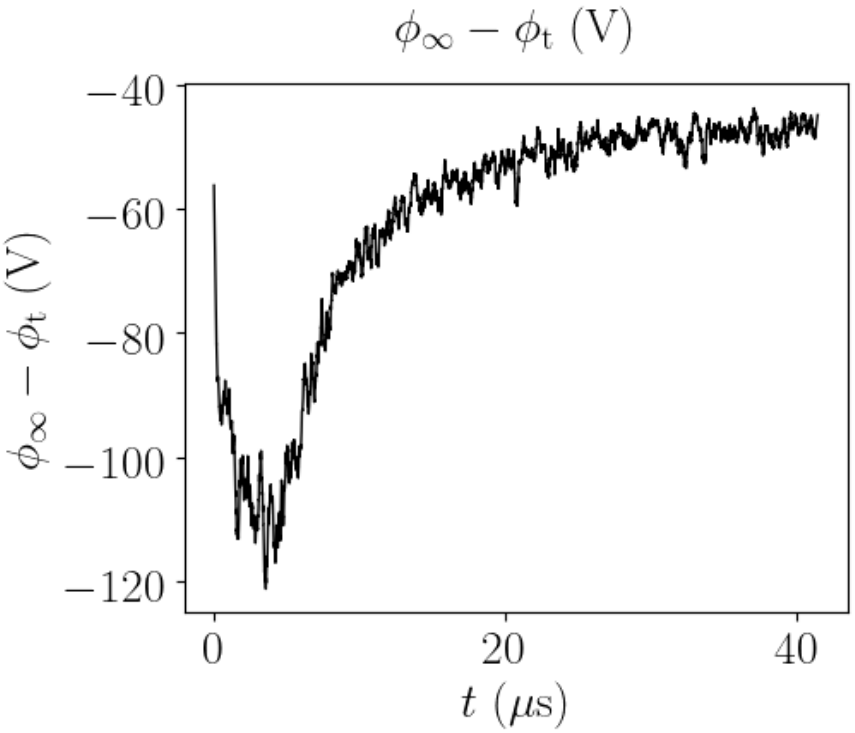


Figure 3.12: Evolution of the potential at infinity relative to the nozzle throat (positioned at z = 6 cm, r = 0). This potential difference is mediated in time on a window of 0,25 μs

Parameter	units	values
Injected ion mass flow	mg/s	0,866
Dielectric constant scaling factor	(-)	9
PIC time step	s	$5 \cdot 10^{-12}$
Elementary electron mass	kg	$9{,}109 \cdot 10^{-31}$
Elementary ion mass	kg	$6{,}633 \cdot 10^{-26}$
Macro-particle weight	(-)	$4{,}68 \cdot 10^{6}$
Virtual infinity capacity C_∞	nF	0,25
Radial extension of domain	cm	15
Axial extension of domain	cm	25
Cell size along z and r	μm	50
Injection ion axial fluid velocity	m/s	4303
Injection electron temperature	eV	7,667
Injection ion temperature	eV	0,5

Table 3.4: Parameters considered for the PIC simulation of the magnetic nozzle expansion.

since the electrons are magnetized and the plasma is non collisional, they can not cross radially the magnetic field, therefore their density goes to zero beyond the more external magnetic field line indicated with a solid black line. The electron temperature, on the other side, presents a minimum close to the jet boundary (similarly to what happen in a classic Debye sheath) and it decreases slowly within the magnetic nozzle expansion, consistently with the expectation that electron thermal energy is converted in ion direct kinetic energy.

The figure 3.13 (e) show the relative charge density, highlighting the non neutral region of the expansion. A region positively charged can be observed close to the boundary of the jet due to the fact that ions are essentially non magnetized and they can easily cross the magnetic field lines, while electrons can not. In the quasi totality of the plasma, however, the quasi-neutrality holds, including at the injection boundary $z = L/2$, therefore validating the simulated injected approach.

In the end, the figure 3.13 (f) show the axial magnetic thrust density $(j \times B)_z$, i.e. the magnetic thrust per unit of volume. Since the magnetic induction field has no azimuthal component, this is given by $f_{z,mag} = -j_\theta B_r$, and it is mainly generated in the peripheral region of the jet. Peak values close to $30N/m^3$ can be observed. Since the plasma jet is essentially quasi-neutral everywhere (see figure 3.13 (e)), this volumetric force is the only direct contribution to the thrust of the magnetic nozzle.

The total intensity of the thrust is obtained integrating the total axial momentum flux across the open simulation boundaries (the dotted blu lines, S_{down}, in figure 3.8) as:

$$F = \iint_{S_{down}} [(n_i u_i \cdot 1_\perp) m_i u_{z,i} + (n_e u_e \cdot 1_\perp) m_e u_{z,e} + (p_i + p_e) 1_\perp \cdot 1_z] dS \tag{3.56}$$

where $1_\perp$ is the perpendicular unit vector at the boundary and it is directed towards the external (outside of the simulation domain), and 1_z is the unit vector along the axial direction z. After a simulation time of $44\mu s$, the total thrust is of 11,1 mN and it is almost completely steady state. This can be divided in 7,7 mN of momentum flux injected (from the ionization chamber), 0,1 mN of pressure force on the frontal walls of the thruster (yellow surface, S_{up} in figure 3.8), 3,4 mN of axial magnetic force density integrated on the simulated volume ($\iiint_V -j_\theta B_r dV$) and a small negative contribution of -0,1 mN due to the electric force integrated ($\iiint_V \rho_c E_z dV$). This thrust value is

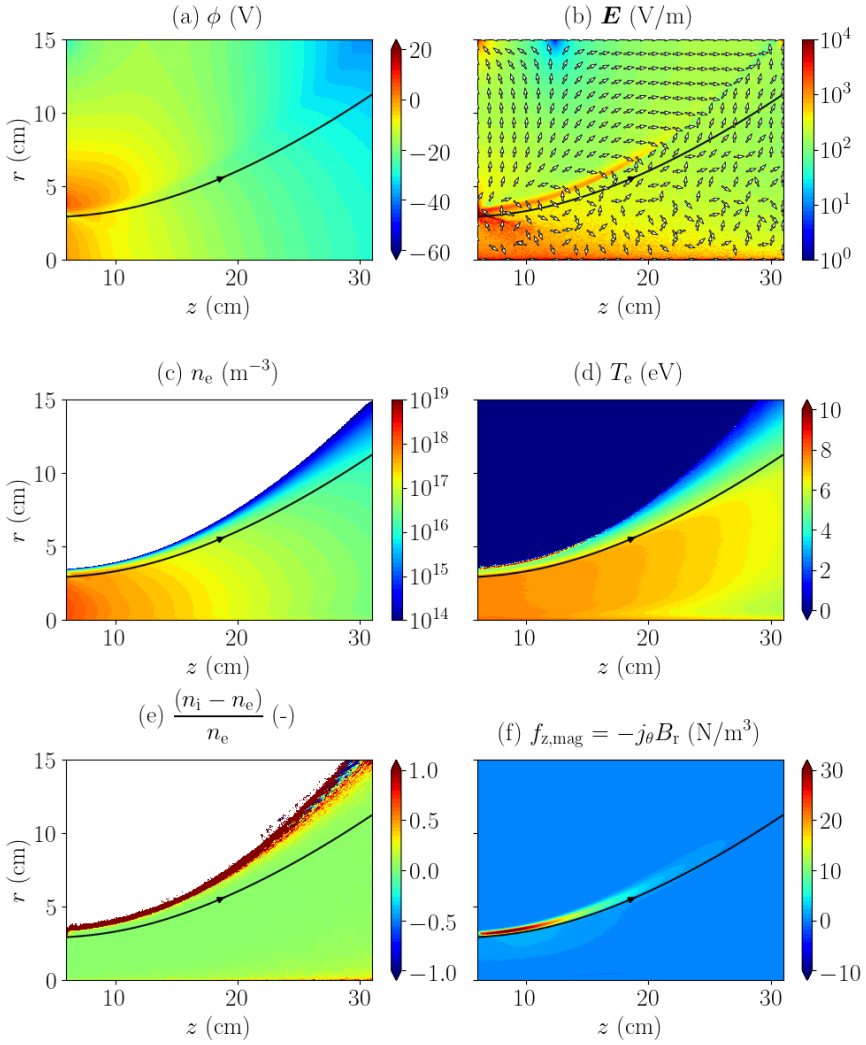


Figure 3.13: 2D plasma properties maps, that show (a) the electric potential, (b) electric field intensity with direction, (c) electron density, (d) electron temperature, (e) relative charge density $(n_i - n_e)/n_e$, and (f) axial magnetic force density. The electric potential is assumed equal to 0 at the nozzle throat ($z = L/2, r = 0$). The more external magnetic field line that starts within the ionization chamber is shown as a black line. Results are time averaged on a window of $0,25\mu s$ and they are computed at a simulation time of $44\mu s$

close to the one predicted from the global 0-D model (12 mN), that does not take into account losses for jet divergence. These can be estimated as the ratio between the energy flux in z direction and the total energy flux (in any direction) across the S_{down} surface. Neglecting pressure effects and heat flux at the downstream section (where the plasma density is decreased significantly), this divergence efficiency of the jet can be approximately estimated from the ion fluid properties as:

$$\eta_{div} \approx \frac{\iint_{S_{down}} n_i u_i \cdot 1_\perp m_i u_{z,i} |u_{z,i}| dS}{\iint_{S_{down}} n_i u_i \cdot 1_\perp m_i u_i^2 dS} \tag{3.57}$$

i.e. as the ratio between the ion kinetic energy flux in z direction (with sign) and the total ion kinetic energy flux across the open surfaces. At the last computed time, this divergence efficiency is almost steady state and equal approximately to 88%. Clearly such high value can depend on the magnetic field topology and on the ion-electron collisions with a neutrals background that have not been modeled, that should reduce it slightly.

Chapter 4

Conceptual study of a nuclear fusion plasma thruster

4.1 The PROTO-SPHERA experiment of the ENEA Research Center in Frascati



Figure 4.1: Composed image of the Crab Nebula built with the data collected in time from three space telescopes: Chandra represented in blu and white, Hubble in violet and Spitzer in dark pink.

The PROTO-SPHERA experiment (Spherical Plasma for HElicity Relaxation Assessment) was built from the Italian National Agency for the New Technologies, Energy and Sustainable Economic Development (ENEA), in the Frascati Research Center to study an innovative plasma magnetic confinement configuration, the first plasma experiment with a simply connected configuration and closed flux surfaces, with the aim of studying an alternative magnetic configuration to tokamaks in the exploitation of the nuclear fusion energy. PROTO-SPHERA is an experiment that is analogous to the jet+torus plasma configuration of the Crab Nebula figure 4.1; discovered in the 1731 and cataloged in the 1774 it is a pulsar, a neutrons star with rapid rotation and highly magnetized. The combination of rapid rotation and the strong magnetic field generate an intense electromagnetic field, with jets of matter and antimatter that move away from the north and south poles of the

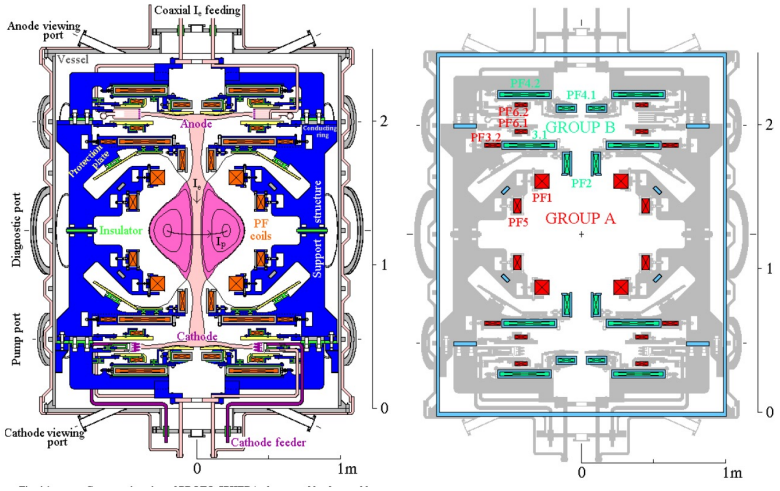


Figure 4.2: Pinch+torus magnetic configuration of the PROTO-SPHERA experiment and distribution of the poloidal coils divided in Group A and Group B [3].

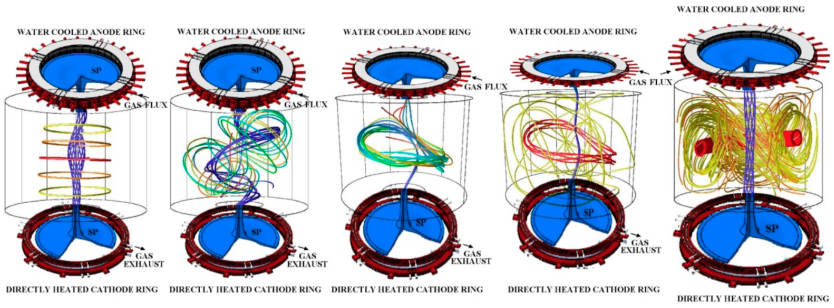


Figure 4.3: Formation and evolution of the plasma central column and of the spherical torus [4, 5]

pulsar and an intense wind that blows towards the equatorial plane, from which the shape of the nebula made by a jet of matter surrounded by matter of toroidal shape [58].

The PROTO-SPHERA experiment is made by a central column of a magnetized plasma (screw-pinch) surrounded by a torus, as shown in figure 4.2. The geometry of the confined plasma is simply connected that is a closed geometry with no holes, and it is obtained from an electric discharge brought to an unstable state, generated between two electrodes: an anode and a cathode, no metallic conductor is connected to the plasma torus and the vacuum chamber that contains the experiment is a cylinder made by a non metallic material. The central plasma column (screw-pinch) is sustained by a voltage in continuous current (DC) applied indeed between the internal electrodes of the vacuum chamber, and the plasma torus is formed by auto-organization around the central plasma discharge [59] (figure 4.3): force lines that surround the central plasma discharge are broken and they reconnect in force lines that surround the torus. The auto-organization phenomenon is based on the magnetic reconnection, that is associated to dissipative effects of the MHD plasma (such as finite resistivity) and they are everywhere in astrophysical plasma, from earth magnetosphere, up to the solar corona, the Crab Nebula and jets of active galactic nuclei in order of increasing size, in figure 4.3 is reported a simulation [4, 5] that describes the formation and the evolution of the PROTO-SPHERA plasma from the central column up to the spherical torus.

The magnetic reconnection phenomenon can be summarized as follow: close to a point, or a curve, where two magnetic field lines almost touch, but they have opposite direction of the field

(the so called X point) a rupture of these magnetic field lines happens that is followed by a new reconjunction between them. The resulting magnetic field configuration from the reconnection has a lower energy, that leads to plasma thermal heating and to super thermal particles acceleration. Magnetic reconnections redistribute magnetic helicity (defined as $K = \int \vec{A} \cdot \vec{B} dV$, where $\vec{A}$ is the magnetic potential vector and $\vec{B}$ is the magnetic field vector) without destroying it in a plasma not perfectly conductive in which resistive effects are relevant, while this is a integral quantity that is conserved in a perfectly conductive magnetized plasma. A fundamental equation of the magnetic helicity is the helicity transport equation that describes as helicity can vary in time in a resistive plasma and it is the following:

$$\frac{dK}{dt} = 2[V_e \Phi - \int \eta \vec{J} \cdot \vec{B} dV] \tag{4.1}$$

where V_e is the feeding voltge of the experiment, for PROTO-SPHERA it is the anode feeding voltage, Φ is the magnetic field flux across the feeding surface, in the case of PROTO-SPHERA it is the magnetic flux injected at the anode, η, $\vec{J}$, $\vec{B}$ are the resistivity, the current density vector and the magnetic field vector of the plasma respectively and V is the plasma volume. The product $W = V_e \Phi$ is defined as the injected helicity and it is the product of the feeding voltage and the magnetic field vector flux across the feeding surface and in steady state condition, when there is no more variation in time of helicity K, helicity K is a constant quantity, as obtained from the equation 4.1. Assuming a steady state for the PROTO-SPHERA experiment in its spherical configuration, it is obtained for the helicity conservation that the helicity injection at electrodes W_e is equal to the helicity injection in the torus W_t, that is in the equilibrium magnetic configuration helicity is transferred from electrodes (and therefore from the screw-pinch) to the plasma torus, in agreement to the following equality:

$$W_e = W_t \tag{4.2}$$

$$B_e S_e V_e = B_t S_t V_t \tag{4.3}$$

where B_e, S_e and V_e are the magnetic field, the surface and the feeding voltage at the electrodes respectively and B_t, S_t and V_t are the magnetic field, the surface and the plasma voltage respectively of the torus. From this relation between the screw-pinch and the spherical part that are united in a unique magnetic configuration by means of the magnetic reconnections, it is obtained that the magnetic flux and the electric current are transferred between magnetic field regions that in the ideal magnetohydrodynamic (MHD) would have been disconnected. The magnetic reconnection points are therefore known also as magnetic helicity injection points that is at the basis of the formation and of the sustainment of the PROTO-SPHERA experiment spherical configuration [60]. This conservation model of the magnetic helicity, obtained from the magnetic helicity transport equation, applied to the PROTO-SPHERA experiment allows to compute the plasma toroidal voltage V_t, assuming that is known the spherical magnetic configuration geometry (S_t) and the toroidal magnetic field (B_t), in agreement to the following expression:

$$V_t = \frac{B_e S_e V_e}{B_t S_t} \tag{4.4}$$

and dividing the plasma toroidal voltage for the length of the spherical torus circumference, it is obtained the toroidal electric field of the spherical magnetic configuration E_t:

$$E_t = \frac{V_t}{2\pi R} \tag{4.5}$$

and applying the plasma Ohm law, from the toroidal electric field it can be determined the toroidal plasma current J_t, with the following relation:

$$J_t = \frac{E_t}{\eta} \tag{4.6}$$

this is a plasma fundamental parameter of the spherical magnetic configuration, that allows to compute how much toroidal current is generated from an axial current discharge (in PROTO-SPHERA this ratio is $\frac{I_t}{I_e} \approx 4$) and how much ohmic energy is transferred and confined in the torus region. With this model of helicity conservation it is explained how the plasma current can be generated in the torus by helicity injection, a phenomenon that is known in literature as helicity current drive [61] and that is applied also in the PROTO-SPHERA spherical magnetic configuration. An inevitable difference between PROTO-SPHERA and its analogous cosmic (figure 4.1) is that in astrophysics the matter containment force is the gravitational force, while in the case of the laboratory experiment the plasma containment is made by the poloidal magnetic field produced by coils (figura 4.2 and 4.4), externals to the plasma configuration, that are responsible for the compression, shape and elongation of the magnetic configuration. Another difference, in the non relativistic approximation, is that in astrophysics the plasma solenoidal condition on the current density $\nabla \cdot \vec{J} = 0$ is automatically satisfied everywhere being the magnetic configuration surrounded by vacuum, while in the laboratory experiment there are metallic conductors that the plasma can electrically charge and on which can flow secondary currents that can lead to a finite divergence of the plasma current density. An effect of this conductors charging that surround the plasma is that it can induce the spontaneous plasma rotation around the symmetry axis, that makes the laboratory configuration more similar to the astrophysics one. To avoid the formation of secondary currents that can deform the magnetic configuration, the initial containment cylinder of the PROTO-SPHERA experiment, made in aluminum, has been substituted with a containment cylinder made in PMMA insulating and transparent to allow a better control and visibility of the plasma from the ouside [60]. Poloidal coils of the PROTO-SPHERA experiment are divided in Group A coils and Group B coils (figure 4.2 and 4.4) [59], the Goup B coils, in which a constant current flows during the experiment, are shape coils of the central plasma column (screw-pinch), and they divide the plasma discharge in three parts: up the anode plasma, in the middle the principal equatorial plasma (that extends for a length of $0,87m$ in height between the two poloidal coils PF2) and down the cathode plasma. The poloidal coils PF2 are of annular shape and since the screw-pinch discharge cross them internally, they are protected internally by additional cylindrical shells made by copper and tungsten. The poloidal magnetic field reaches in the middle of the poloidal coils PF2 its maximum value: around $0,5T$. The Group A coils instead are compression coils in which flow a variable current during the experiment, that are necessary to contain the plasma torus. In addition there are external poloidal coils in the machine assembly of the PROTO-SPHERA experiment that allow the formation of the spherical magnetic configuration and therefore the toroidal part of the experiment.
These coils of the PROTO-SPHERA experiment have been positioned in various construction phases

of the machine. In 2001 it was ended the machine design and in the next year in a international Workshop that took place in Frascati held by Martin Peng, it was decided to build the machine in different phases and between the 2006 and 2009 the construction started. The construction phases of the machine are summarized below:

- **Phase 1.0 (May 2015 - January 2018)**: the aim of the first phase was to demonstrate the feasibility of the central plasma column between the two electrodes. In **Phase 1.0** the START (Small Tight Aspect Ratio Tokamak) vacuum chamber was used, the first tokamak machine with a spherical design operative at the Culham Science Centre in United Kingdom from 1990 to 1998, that was donated by the Culham Science Center for fusion energy. The vacuum chamber was completely emptied from internal metallic conductors, with the external part made by 4 cm of alluminum, with diameter and height of 2 m. The vacuum chamber is a cylinder with the upper and lower part occupied by electrodes that close it hermetically, reaching inside an internal vacuum of $0,8 \times 10^{-7} bar$. The feeding system of the PROTO-SPHERA machine is illustrated in figure 4.5 and it can be divided in:

  - **Cathode power supply**: the first stage of the cathode power supply is an "active front end" (AFE) that rectifies a three phase voltage with an effective value (rms) of 400 V at 50 Hz. The exit of the AFE is a continuous current signal (DC) and it is provided in input to a three phase inverter that transforms the signal in a three phase signal. The additional three phases required from the cathode power supply are provided by a transformer that converts a three phase signal of 380 V in a hexa phase signal of 30 V. The resulting cathode power supply can reach 25 V and 1,7 kA per phase in the peak point. The alternate hexa phase feeding system introduces a rotating magnetic field with phase shift of 60° between the phases and such field allow to reduce the anchoring of the pinch arch to the cathode, therefore decreasing the thermal loads of the structure.
    The cathode power supply is capable to operate in a continuous way, but its operations must be limited to avoid stresses and deformations to the tungsten filaments. The reference value (10 - 20 V rms) is reached after almost 15 s and it is kept for almost 1 s, when the cathode reaches the reference value ("flat-top") the coils and the anode power supplies are activated, that have a rise time lower than 50 ms, therefore the three systems can operate simultaneously.
    From a structural point of view the cathode feeder is composed by an annular structure positioned in the lower part of the chamber made by 4 copper disks, two externals to dissipate the heat and cooled with water and two centrals in which stay 18 modulus in molibdenum fed with 1,7 kA and 25 V, each one with three tungsten filaments capable to emit 150 A by termoionic effect. Tungsten filaments are designed with a special conical spiral shape to optimize the termoionic effect, they are heated up to 2600 °C, with experiments performed also at 3000 °C, and the emitted electrons from the filaments produce the plasma ionizing the gas emitted from the anode [3].

  - **Anode power supply**: the anode power supply is based on a converter of 12 pulses from alternate current to continuous current (AC/DC) made by a "thyristor bridges" parallels fed by a transformer 20 kV/324 V with two secondary windings (delta and

star). The scope of the anode power supply is to generate and maintain the arch between the electrodes. The current controller is regulated to reach the current reference value ("flat-top") in the minimum time and the current can be generated in less than 25 ms and kept for more than 1 s with 2% of oscillation. The current controller connected to the electrodes perceives an open circuit and it increases the voltage up to the necessary value for the breakdown and the formation of the electric arch. Reached the breakdown the impedance between the electrodes is reduced, leading to a decrease of the voltage between the electrodes. The discharge feeder of the anode provides therefore 10 kA and almost 350 V.
From a structural point of view the anode has an annular structure made 90% with tungsten and 10% with copper from which through an annular tube it is injected directly the gas and it is positioned in the upper part of the chamber. The discharge arc is generated from the potential difference established by the discharge feeder between the two electrodes. The current arch close in an external path to the vacuum chamber, through 8 copper bars that link externally the anode to the cathode (Figure 4.5).

- **Poloidal coils power supply**: the feeding scheme of the poloidal coils is very similar to the anode power supply with a lower current (2 kA of current exiting from the poloidal coils power supply, with respect to the 10 kA of current exiting the anode power supply). In PROTO-SPHERA the Group B poloidal coils and the External poloidal coils are connected in series to the same power supply.
- **External poloidal coils power supply**: since the internal poloidal coils power supply has sufficient margin also to sustain the external poloidal field load, these lasts are connected in series with the internal poloidal coils. However the activation sequence of the discharge is delayed of 0,75 s after the generation of the external poloidal coils current, to allow the diffusion of surface currents on the alluminum vacuum chamber. In the successive phases of the machine the external poloidal coils are fed by a dedicated power supply.

In this phase there are internally in the vacuum chamber only 4 copper magnetic coils, covered in steel: PF2 and PF3.1, with which it is made the vertical or poloidal magnetic field, PF4.1 and PF4.2 that allow to obtain an homogeneous plasma shape close to the electrodes, diffusing on a larger zone the plasma current and therefore also the power, as shown in figure 4.2 and 4.4.
Initially there were uncontrolled plasma discharges that have been improved with a more accurate electric insulation.

- **Phase 1.25 (January 2018 - September 2019)**: in this phase it was verified the stability of the first magnetic confinement configuration in spherical shape, with the aim of studying the formation and manteinment dynamics of the torus. In the machine 4 external coils to the vacuum chamber were added (PFExt), as shown in figure 4.4. The coils are positioned two at the equator and they create an external vertical magnetic field directioned from up to down that shifts the plasma close to the electrode, one is positioned in the upper part and the other on the downer part of the vacuum chamber (with currents that flow in opposite

direction with respect to the equatorial ones) that are necessary to bring back the plasma in the correct position at the electrodes. The new external coils are fed by a super capacitor capable to provide 2 kA at 90 V for few seconds. In the end it was added a divertor to protect and isolate the PF3.1 coil that was exposed to the plasma, before it reaches the electrodes.
The addition of external coils, with the generation of an additional vertical magnetic field creates abrupt discontinuities of the magnetic field with abrupt space variations of polarity that give rise to magnetic reconnections that trap the plasma inside magnetic islands. For the rotational invariance of the created magnetic islands in a plane, these become a torus in the space where the plasma is confined. The intersection points between the magnetic surfaces of the pinch and of the torus correspond to the X points, where the poloidal magnetic field is null.
The major obstacle of this phase was given from the slow penetration of the magnetic field of the external coils inside the metallic vacuum chamber. But the introduction of an external magnetic field brought the immediate steady state confinement of the plasma in the torus.

- **Phase 1.5 (September 2019 - in progress)**: this phase is the test for the final configuration of the experiment, but still with the test coils and feeders. The first vacuum chamber in alluminum has been substituted with one in PMMA (Polymethylmethacrylate, commonly called Plexiglas) 1,7 m in height and 2 m in internal diameter and 9 cm of thickness. The vacuum chamber has 12 windows for observation, with a diameter of 12 cm, in the equatorial zone, other 4 windows of 9,2 cm are positioned in the upper part and symmetrically in the down part. A thin layer of 2 mm polycarbonate has been added internally to avoid a direct contact of the plasma with the PMMA and to filter the UV radiation emitted from the plasma. In this phase are added other 6 internal coils partially-covered (PFint-A, coils of the Group A), 3 in the upper part and 3 in the lower part. The 4 external coils have been substituted, always in the same positions, with 4 new coils wrapped with a larger cable ($240mm^2$ in section) obtaining a resistance lower than the previous and therefore a higher current for the same feeding voltage.
  With the new vacuum chamber in PMMA the stabilization times of the magnetic fields generated by external coils are reduced to few tens of milliseconds. This provides a time interval larger to study the torus formation and a better measure of the experiment.

- **Phase 2.0 (postponed)**: this is the conclusion phase of the experiment that foresees the construction of the all internal covered coils and feeders capable to generate 70 kA of plasma current in the central column, with the aim to obtain spherical torus, that takes 95% of the total volume, with almost 300 kA of toroidal current. This phase has not been realized yet.

- **Beyond phase 2.0**: the constructive phases described previously have the scope to verify the feasibility of the new magnetic confinement configuration, with the aim to build a future machine for controlled thermonuclear fusion if in the spherical torus are reached temperatures close to the ignition one for thermonuclear fusion. The plasma generated and confined in PROTO-SPHERA has temperatures of hundred of thousands of Kelvin (1 eV - 10 eV) and high electron density $10^{19} - 10^{20} particles/m^3$ and therefore of interest for the nuclear fusion research.
  The realization of a reactor for the controlled thermonuclear fusion with this configuration

has different advantages: it has not the problematics related to a toroidal vacuum chamber in designing and maintaining the internal metallic components, making the machine design simpler and lighter, it is easily to access for measurements due to the transparency of the vacuum chamber, in comparison to the tokamak that works in pulsed regime it can work in continuous regime providing a continuous feeding voltage to the electrodes and to the coils. Moreover it does not require complex additional heating systems for the plasma because the natural phenomenon of the magnetic reconnections converts the magnetic energy in thermal energy and in the end it can provide values of the β parameter higher than the tokamak, reducing the cost of a fusion reactor to the 1% of the cost required for a tokamak [3].
A fusion reactor would provide more energy, for a given weight of propellant, than other current enegy sources that use propellant and the more used propellant (Deuterium) is abundant on Earth. In addition the adopted technologies from nuclear fusion are safe and with limited wastes, expecially if compared to nuclear fission and the success of PROTO-SPHERA as a fusion reactor can provide relevant contributions in many plasma applications: fusion reactors, tokamak standards, spherical tokamaks, spheromaks, reversed field configurations, material characterization, propulsion engines and astrophysical phenomena [3].

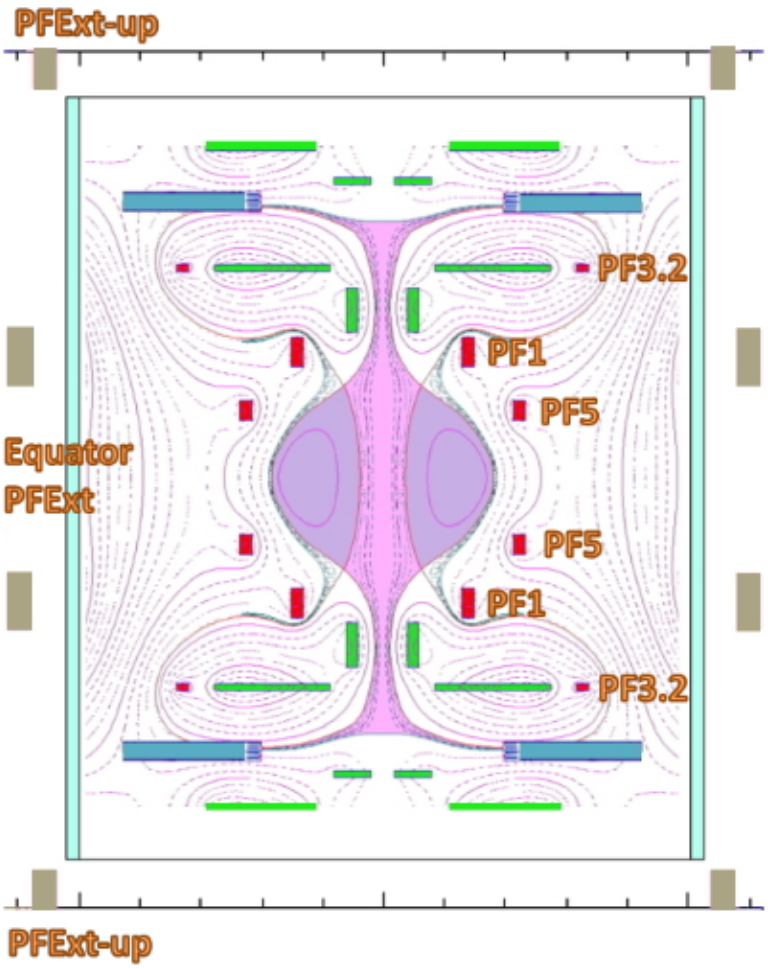


Figure 4.4: Pinch+torus magnetic configuration of the PROTO-SPHERA experiment with the addition of external coils PFExt

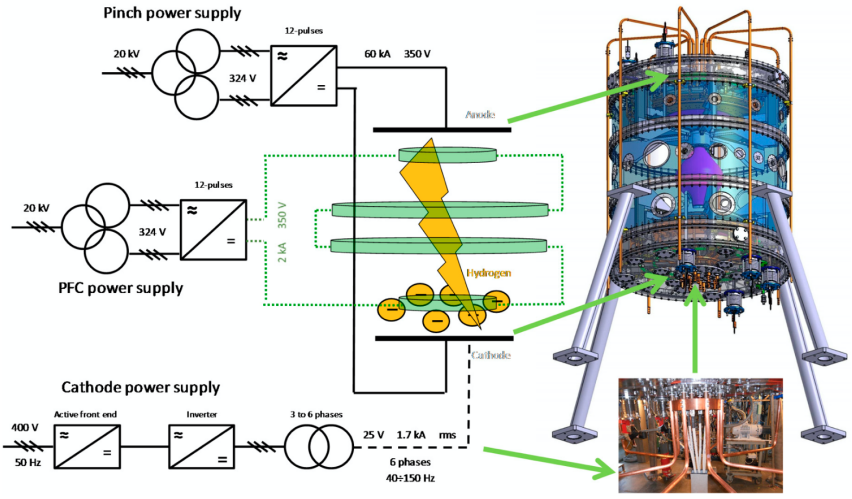


Figure 4.5: Schematic of the PROTO-SPHERA power feeding system and of the vacuum chamber [3].

The PROTO-SPHERA experiment has been designed to sustain a plasma axial current of $70kA$, to produce a spherical torus of $70cm$ in diameter with an aspect ratio $A = 1,2 - 1,3$ and a total toroidal current of $I_T = 280kA$, having therefore a design ratio between the plasma toroidal current and the plasma axial current $I_T/I_z = 4$. The sphericity of the magnetic configuration and the small aspect ratio close to 1 are chosen for the high β obtainable from this configuration of the machine [3].
PROTO-SPHERA is characterized by two main magnetic configurations that can be obtained from the plasma discharge generated between the two electrodes (as shown in figure 4.6): a screw-pinch, that is an axial plasma column confined and stabilized with internal magnetic fields of the plasma and external of the coils and a spherical magnetic configuration that is a spherical torus that surrounds it. In the first phase of the PROTO-SPHERA experiment (**Phase 1.0**) [60] both the screw-pinch and the torus have been obtained in steady state and stably. In particular the formation voltage of the breakdown discharge between anode and cathode for Argon is of $90V$ that reaches a value of $200V$ for an axial steady state current of $10kA$. The mean line electron density for Argon measured at the equator reached values of $< n_e >= 4 \cdot 10^{20} particles/m^3$ at the current of $10kA$, with an equatorial plasma diameter of $55cm$. Measurements at the edge of the anode made with the Langmuir probe have given a temperature that varies from $2eV$ to $8eV$, corresponding to a local plasma electron density that varies from $n_e = 5 \cdot 10^{19} particles/m^3$ to $n_e = 2 \cdot 10^{19} particles/m^3$. The breakdown voltage for hydrogen instead is of $300V$, higher than the one for Argon, and it settles at a value of $200V$ for an axial current discharge of $10kA$. The mean line electron density measured for hydrogen at the equator reached values of $< n_e >= 1,5 \cdot 10^{20} particles/m^3$ at the current of $10kA$, with a plasma equatorial diameter of $75cm$, higher than the Argon plasma. Also hydrogen plasma tori have been obtained in the first experimental phase of the PROTO-SPHERA experiment with toroidal current up to $5kA$. Due to the electrostatic charging of the poloidal field coils PF, in addition, the axial plasma discharge rotates approximately at a frequency of $100Hz$ [59, 60].

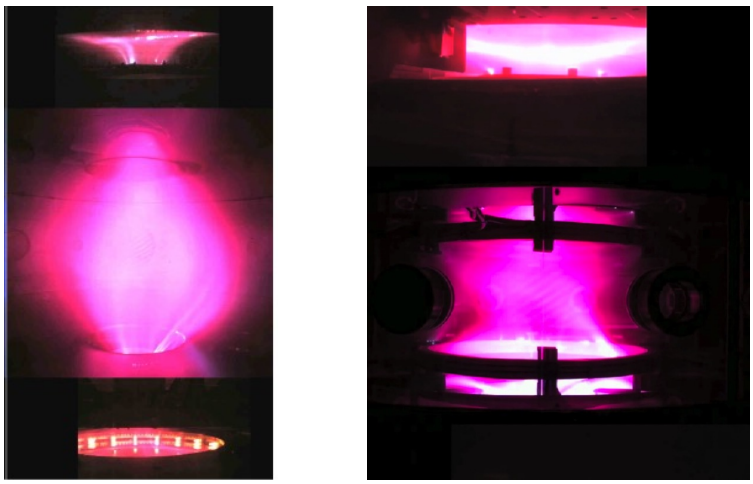


Figure 4.6: Magnetic configurations of the PROTO-SPHERA experiment with hydrogen plasma: (a)screw-pinch, (b)screw-pinch + torus

4.2 Experimental estimate of the PROTO-SPHERA pinch electron temperature

One of the equilibrium magnetic configuration of the PROTO-SPHERA experiment is the screw-pinch, that is a plasma column generated between two electrodes, an anode and a cathode that is stabilized by external magnetic fields. Iannarelli et alia [62] have proposed a model to estimate the plasma state within the PROTO-SPHERA pinch [63, 64], by modeling the thermodynamic state of the plasma column at the equatorial plane of the magnetic configuration where it can be probed with the installed diagnostics and where the plasma column can be better approximated as a screw-pinch with constant cross section.
The pinch is modeled as a cylindrical plasma column with constant cross section and an axial plasma current that is radially inhomogeneous and that flows in it, with an azimuthal magnetic field consistent with the equilibrium profile of the axial current. An external poloidal magnetic field is added to the azimuthal magnetic field to stabilize the central plasma column. Indeed the axial component of the magnetic field wrap the field lines around the discharge arch increasing the central plasma column confinement, that is therefore modeled as a screw-pinch [65]. The plasma is considered as a steady state conductive fluid in MHD equilibrium, in presence of a neutral gas of the same specie and with a constant angular rotation. Assuming an axial symmetry, an ideal radial MHD equilibrium model (1D) is coupled with a scalar power balance equation (0D) of the plasma pinch and the two models are solved in a combined way with an iterative procedure until numerical convergence is reached. Radial profiles of the plasma pressure, of the electron density and of the axial current density are assumed of exponential type: $p(r) = p_0 \exp(-\alpha r^2/a^2)$, $n_e(r) = n_{e0} \exp(-\beta r^2/a^2)$ e $J_z(r) = J_{z0} \exp(-\gamma r^2/a^2)$ where p_0, n_{e0} and J_{z0} are the peak values of the pressure profiles, of the electron density and of the axial current density, α, β and γ are the

shape parameters of the profiles and a is the plasma radius. Instead the temperature radial profile is not fixed but computed from the ratio of the pressure and density profiles, in agreement to the perfect gas state equation:

$$T_e(r) = \frac{p(r)}{2n_e(r)k_B} \tag{4.7}$$

where k_B is the Boltzmann constant and the factor 2 comes from the equality between the ion and electron density for the plasma quasi-neutrality, having assumed that ions and electrons are at the same temperature. The equation 4.7 is valid only for singularly charged plasma. The neutral model is added to the MHD equilibrium model to compute the neutral equilibrium inside the magnetic configuration. Neutrals are present within the plasma or due to no ionization of the chemical specie at low temperatures or due to plasma recombination at low temperatures. A model that takes into account both the dependence on the specie ionization and on the specie recombination is an equilibrium model between ionization and recombination. The continuity equations of the two species state that the density variation of the specie in time is given by the them ionization and recombination rates:

$$\frac{\partial n_i}{\partial t} + \nabla(n_i v_i) = \Gamma_n^{ion} - \Gamma_i^{rec} \tag{4.8}$$

$$\frac{\partial n_n}{\partial t} + \nabla(n_n v_n) = \Gamma_i^{rec} - \Gamma_n^{ion} \tag{4.9}$$

For each specie, ions and neutrals, it is hypothesized that the production rates of ions and neutrals are given by a collision model between the reactant species and electrons:

$$\Gamma_n^{ion} = n_e n_n < \sigma_{ion} v_e > \tag{4.10}$$

$$\Gamma_i^{rec} = n_e n_i < \sigma_{rec} v_e > \tag{4.11}$$

with the ionization and recombination rates computed in agreement with an ionization model by electron impact as made in [66, 67]. In the hypothesis that the plasma is steady state and that therefore the time derivatives are zero and that the plasma fluid velocity is zero, the production rates of the two species can be equated, giving an analytical expression for the neutrals and ions density. The estimate model of the neutrals density for a plasma fluid with two components is obtained.
For singularly ionized plasma, as the hydrogen plasmas, the plasma model assumes that the neutral production rate is equal to the ion production rate in modulus, that is there is equilibrium between recombination and ionization:

$$|\Gamma_i^{rec}| = |\Gamma_n^{ion}| \tag{4.12}$$

$$\not{n}_e n_i < \sigma_{rec} v_e > = \not{n}_e n_n < \sigma_{ion} v_e > \tag{4.13}$$

In the hypothesis that in singularly ionized plasma the electron density is equal to the ion

density, it is obtained an analytical expression for the neutral density:

$$n_n = n_e \frac{< \sigma_{rec} v_e >}{< \sigma_{ion} v_e >}, \quad for\ singularly\ ionized\ particles \tag{4.14}$$

For doubly ionized plasmas, as Helium or Argon, it is assumed that the production rate of ionized species and the production rate of recombined species are equal for all the reaction stages and that each ionization stage is in equilibrium. Applying the equilibrium formula for singularly ionized plasma for each reaction stage, it is obtained:

$$n_n = n_i^{1+} \frac{< \sigma_{rec} v_e >}{< \sigma_{ion} v_e >_{1^+}}, \quad 1^{st}\ ionization\ equilibrium \tag{4.15}$$

$$n_i^{1+} = n_i^{2+} \frac{< \sigma_{rec} v_e >}{< \sigma_{ion} v_e >_{2^+}}, \quad 2^{nd}\ ionization\ equilibrium \tag{4.16}$$

Substituting the second equation in the first, it is obtained an expression for the computation of the ion density of doubly ionized plasmas, that is the following:

$$n_i^{2+} = \frac{n_n}{\frac{<\sigma_{rec} v_e>}{<\sigma_{ion} v_e>_{1^+}} \frac{<\sigma_{rec} v_e>}{<\sigma_{ion} v_e>_{2^+}}} \tag{4.17}$$

Relations just reported are analytical expressions for the computation of the ion densities at each ionization stage. Both expressions require the knowledge of the neutral density that can be estimated assuming known the plasma electron density and that this from the plasma quasi-neutrality is given by the sum of electrons produced by the singularly ionized plasma and the ones produced by the doubly ionized plasma:

$$n_e = n_e^{1+} + n_e^{2+} = n_i^{1+} + 2n_i^{2+} = \frac{n_n}{\frac{<\sigma_{rec} v_e>}{<\sigma_{ion} v_e>_{1^+}}} \left(1 + \frac{2^+}{\frac{<\sigma_{rec} v_e>}{<\sigma_{ion} v_e>_{2^+}}}\right) \tag{4.18}$$

Inverting this relation it is obtained an analytical expression of the neutrals density also for doubly ionized plasmas as function of the electron density:

$$n_n = \left(\frac{n_e \frac{<\sigma_{rec} v_e>}{<\sigma_{ion} v_e>_{1^+}}}{\frac{<\sigma_{rec} v_e>}{<\sigma_{ion} v_e>_{2^+}} + 2}\right)\left(\frac{< \sigma_{rec} v_e >}{< \sigma_{ion} v_e >_{2^+}}\right), \quad doubly\ ionized\ particles \tag{4.19}$$

In agreement to the momentum conservation equation for a plasma fluid the momentum variation is equal to the net external force applied. The external forces acting are: the Lorentz force that is generated from the interaction between charged particles and the magnetic field, the pressure gradient and the centrifugal force, and for a plasma fluid in MHD equilibrium these forces balance each other. The momentum conservation equation in radial direction for the screw-pinch, written as function of the magnetic field components, states that:

$$\frac{d}{dr}\left(\frac{B_z^2}{2\mu_0}\right) = -\frac{d}{dr}\left(p + \frac{B_\theta^2}{2\mu_0}\right) - \frac{B_\theta^2}{\mu_0 r} + f_c(r) = G(r) \tag{4.20}$$

where the expression for the centrifugal force is the following:

$$f_c(r) = m_i \omega^2 r n_i \tag{4.21}$$

with $m_i(kg)$ is the ion mass, $\omega(rad/s)$ the plasma rotational angular frequency, $r(m)$ the distance

of the particle from the rotation axis and $n_i(particles/m^3)$ the ion density. Having assumed a radial current profile of exponential type $J_z(r) = J_{z0}\exp(-\gamma r^2/a^2)$, with a shape parameter γ computed as the ratio between the axial current density at the pinch boundary and the axial current density on the pinch axis:

$$\gamma = -\ln(\frac{J_z(a)}{J_{z_0}}) \tag{4.22}$$

it is defined the azimuthal component of the magnetic field B_θ from the IV Ampère-Maxwell equation, that has the following expression:

$$B_\theta(r) = \frac{\mu_0}{2\pi r}\left[-\frac{\pi a^2}{\gamma}J_{z_0}(e^{-\gamma}-1)\right] \tag{4.23}$$

The equation 4.20 is solved for the field component B_z given the axial current density profile $J_z(r)$, the plasma pressure profile $p(r)$ (derived iteratively from the power balance equation), the azimuthal field component $B_\theta(r)$ (derived from the axial plasma current) and the centrifugal force profile $f_c(r)$ (derived iteratively from the ion profile). Assigned the radial equilibrium profiles of the known terms it is defined the function $G(r)$ that is the right side of the screw-pinch radial equilibrium equation 4.20 that is now possible to integrate directly to obtain the radial profile of the axial magnetic field component $B_z(r)$, for a given value of the axial magnetic field at the pinch boundary $B_z(a)$, that has the following expression:

$$B_z(r) = \sqrt{B_z^2(a) - 2\mu_0\int_r^a G(r)dr} \tag{4.24}$$

Computed the radial equilibrium profile of the magnetic field axial component it is defined the azimuthal component of the current density $J_\theta(r)$, in agreement to the following relation obtained from the IV Ampère-Maxwell equation:

$$J_\theta(r) = -\frac{1}{\mu_0}\frac{dB_z}{dr} \tag{4.25}$$

Computed the radial equilibrium profiles of the electromagnetic quantities, the MHD equilibrium code is reiterated a finite number of times until convergence. In agreement to the energy conservation, the time variation of internal energy in the plasma pinch must be the difference between the heating power and the lost power. In steady state regime an energetic equilibrium is reached when the heating ohmic power (P_Ω) equates the total power lost, modelled as the sum of an anode convective loss ($P_{conv.anode}$) [68], a radiative power loss emitted by the plasma (P_{rad} [22, 69]) and the power loss with the emission of charged particles from the loss cone of the magnetic configuration (P_{jet} [68]), as reported in the research [62]:

$$P_\Omega = P_{conv.anode} + P_{jet} + P_{rad} \tag{4.26}$$

where the previous equation is solved in the mean electron temperature to update iteratively the pressure profile in the MHD equilibrium computation. In the power balance equation 4.26 the P_Ω is defined as the sum of the axial ohmic power P_{Ω_z}, generated by the axial pinch current, and of the azimuthal ohmic power P_{Ω_θ}, generated by the azimuthal pinch current. The expressions of

the single ohmic powers are the following:

$$P_{\Omega_z} = \int_V \eta(< T_e >) J_z^2 dV = \int_r \int_\theta \int_z \eta J_z^2 r dr d\theta dz \tag{4.27}$$

$$P_{\Omega_\theta} = \int_V \eta(< T_e >) J_\theta^2 dV = \int_r \int_\theta \int_z \eta J_\theta^2 r dr d\theta dz \tag{4.28}$$

where the pinch mean electron temperature $< T_e >$, computed as the volume integral of the electron temperature profile made on the pinch plasma volume, has the following expression:

$$< T_e >= T_{e_0}(\frac{\beta}{\alpha})\frac{(e^{-\alpha}-1)}{(e^{-\beta}-1)} \tag{4.29}$$

The pinch resistivity η is computed as the sum of the ionized plasma resistivity and of the partially ionized plasma resistivity, with the neutrals resistivity computed as the partially ionized plasma resistivity. The ionized plasma resistivity is computed in agreement to the Spitzer resistivity model [32], that has the following expression:

$$\eta_{s_\parallel} = 5 \cdot 10^{-5} Z_{eff} \frac{\ln \Lambda}{T_e^{\frac{3}{2}}} \tag{4.30}$$

where Z_{eff} is defined as the plasma effective ion charge, that is the plasma ion charge that takes into account the plasma ion charge and the impurities ion charge within it. The term $\ln \Lambda$ is the Coulomb logarithm and it is defined as the impact plasma parameter, while T_e is the plasma electron temperature expressed in eV. The charged particles motion within a magnetic field region is a spiral motion along the magnetic field lines that is composed of a parallel motion and a perpendicular motion to the direction of the magnetic field lines. Being the instantaneous motion of the charged particles in the perpendicular direction to the magnetic field line, the ionized plasma resistivity is computed as the perpendicular Spitzer resistivity, in agreement to the following expression:

$$\eta_{s_\perp} = \frac{1}{F(Z)}\eta_{s_\parallel}, \qquad F(Z) = \frac{(1 + 1,98Z + 0,222Z^2)}{(1 + 2,966Z + 0,753Z^2)} \tag{4.31}$$

with Z equal to the plasma ion charge.
For partially ionized plasmas instead it is introduced first the general formula of the plasma parallel resistivity that is the following:

$$\eta_\parallel = \frac{m_e \nu_c}{n_e e^2} \tag{4.32}$$

Collisional frequencies for partially ionized plasmas have the following expression:

$$\nu_c = n_n \sigma_n < v_e > \tag{4.33}$$

where n_n is the neutral particles density, σ_n is the neutrals particles cross section and $< v_e >$ is the mean electron thermal velocity. Substituting the collisional frequency expression in the definition of the parallel resistivity, it is obtained the parallel resistivity to the magnetic field direction for partially ionized plasmas:

$$\eta_{n_\parallel} = \left(\frac{m_e \sigma_n}{e^2}\right)\left(\frac{n_n}{n_e}\right) < v_e > \tag{4.34}$$

The ratio between the electrons density and the neutrals density can be expressed from the following relation:

$$\gamma = \frac{n_e}{n_n} = [1 + (5 \cdot 10^{-3} T_e^{\frac{3}{2}})^{-1}]^{-1} \tag{4.35}$$

where the electron temperature is expressed in eV. The other terms of the neutral resistivity are so defined: the neutrals cross section is computed as the transversal section of the neutral particle, assumed of spherical shape, in agreement to the following expression:

$$\sigma_n = \pi r_n^2 \tag{4.36}$$

where r_n is the neutral particle radius. The mean thermal velocity of electrons $< v_e >$ is computed equating the electron kinetic energy with the electron thermal energy associated to a single degree of freedom of the particle, and it has the following expression:

$$< v_e >= (\frac{k_B T_e}{m_e})^{\frac{1}{2}} \tag{4.37}$$

where k_B is the Boltzmann constant expressed in J/K, T_e is the electron temperature expressed in K and m_e is the electron mass expressed in kg. The analytical expression of the parallel neutrals resistivity to the magnetic field direction (resistivity for partially ionized plasmas) is the following:

$$\eta_{n_\parallel} = (\frac{m_e \pi r_n^2}{e^2})[1 + (5 \cdot 10^{-3} T_e^{\frac{3}{2}})^{-1}](\frac{k_B T_e}{m_e})^{\frac{1}{2}} \tag{4.38}$$

The total plasma resistivity is therefore defined with the following expression:

$$\eta = \eta_{s_\perp} + \eta_{n_\parallel} \tag{4.39}$$

Taking back now the power balance equation 4.26, having expressed the ohmic power source term at the first side, at the second side of the power balance equation are instead the dissipative terms of the pinch power, that define the main mechanisms with which the power contained in the pinch is lost. The first term at the right side is the convective power transmitted to the anode $P_{conv.anode}$, the pinch anode is a region with a hot wall from which starts the electric discharge and on which starts current fluxes towards the pinch central column. The thermal exchange in the region in proximity of the anode happens by convection, where due to the thermal gradient between the pinch and the anode and the velocity gradient between the pinch and the wall, a part of the pinch power is dissipated as convective power, leading to a pinch cooling. The convective power term at the anode is computed with the following expression [70]:

$$P_{conv.anode} = \frac{5}{2} < J_{z_0} >< T_e > \pi a^2 \tag{4.40}$$

where the expression of the mean electron temperature $< T_e >$ is the one already introduced and the expression of the mean axial current density $< J_{z_0} >$, computed as the volume average of the axial current density, is the following:

$$< J_{z_0} >= \frac{1}{(\frac{a^2}{2})} \int_r J_z(r) r dr \tag{4.41}$$

The radiative power is the term in the power balance that contributes to the energy dissipation by radiation emission and therefore of plasma energy that is function of the pinch volume. The radiative power from the pinch is computed with different models on the basis of the chemical specie that composes the plasma.

Hydrogen [22], $P_{rad} = P_B + P_C + P_Z$

- Bremsstrahlung power P_B: is the power emitted from the plasma charged particles due to the braking that particles have in coulomb collisions. The expression of the Bremsstrahlung power is the following:

$$P_B = 5,35 \cdot 10^{-37} Z^2 n_i n_e T_e V_P \qquad (W)$$

- Cyclotron power P_C: is the power that is emitted by the plasma due to its gyration motion around the guiding center that lies on the magnetic line, in the rotation the charged particle moves of uniformly accelerated motion and accelerating it loses energy. The expression of the cyclotron power is the following:

$$P_C = 6,2 \cdot 10^{-14} \alpha B^2 n_e T_e V_P \qquad (W)$$

- Line power P_Z: is the radiation that is emitted from the plasma due to the redistribution of the electrons inside the electrons orbitals. To each electron transition is associated a radiation emission, known also as line emission. The expression of the line power is the following:

$$P_Z = 10^{-25}(1 + 0,3T_e) Z^{(3,7-0,33 \ln T_e)} n_e n_i V_P \qquad (W)$$

Helium [69]

- The radiative power for Helium is computed with an experimental fitting model of the emitted plasma power as function of the electron temperature and available for various chemical species. The model is applied for the radiation emission from plasmas made with chemical species with atomic number higher or equal to the Helium atomic number. The model provides also an estimation of the plasma mean charge state (mean ionization charge), computed as function of the plasma electron temperature:

$$P_{rad} = n_i n_e 10^{\sum_{i=0}^{5} A(i) log_{10}[T_e(keV)]^i}$$

$$< Z >= \sum_{i=0}^{5} B(i)[log_{10} T_e(keV)]^i$$

The last dissipative power term contained in the power balance equation 4.26 is the power lost from the pinch due to charged particles emission from the loss cone of the pinch magnetic mirror, P_{jet}. The PROTO-SPHERA pinch is indeed a cylindrical magnetic configuration obtained by an

electric discharge generated between an anode and a cathode aligned along the pinch axis. The magnetic field distribution along the pinch axis is similar to the one of a magnetic mirror with a maximum of the magnetic field in proximity of the anode and of the cathode regions and a minimum of the magnetic field in the equatorial plane. When plasma charged particles pass at high velocity from the anode towards the cathode, due to the high kinetic energy that they have, a fraction of these is lost from the magnetic confinement and is emitted as axial jet of the charged particles. The jet power of the pinch emitted charged particles is computed in agreement to the following expression:

$$P_{jet} = \gamma P_{\Omega} \tag{4.42}$$

The jet power of the charged particles is then computed as a fraction of the source power contained within the pinch that is the heating ohmic power. The proportionality term between the jet power and the source power contained within the pinch is the factor γ that is defined in agreement to the following expression:

$$\gamma = 2\frac{\Omega}{2\pi}H = 2(1-\cos\theta)H \tag{4.43}$$

where the factor 2 is introduced for the symmetry of the magnetic mirror that can produce emission of charged particles in both the axis directions, the factor $\Omega/2\pi$ is defined as the ratio between the solid angle described by the loss cone of the charged particles and the solid angle described by the semisphere, with θ equal to the aperture angle of the charged particles loss cone, defined as function of the magnetic field intensity on the axis, in agreement to the following expression:

$$\theta = asin[(\frac{B_{z_{min}}(r=0)}{B_{z_{max}}(r=0)})^{\frac{1}{2}}] \tag{4.44}$$

The third factor that appears in the expression of the proportionality factor γ is the H term, and it is an amplification factor of the charged particles loss that models the increase of the emitted particles across the jet of the loss cone due to collisions and kinetic microinstabilities of the plasma caused by anisotropy of the velocity distribution function. The power balance equation 4.26 is therefore a non linear equation in the variable $< T_e >$ that can be solved with an iterative method. The chosen iterative method is the Newton-Raphson method that is described next with the Newton-Raphson function (equation 4.45), the derivative of the Newton-Raphson function (equation 4.46) and the updating formula for the volume mean electron temperature (equation 4.47):

$$f(< T_e >) = P_{\Omega}(1-\gamma)_{(<T_e>)} - P_{conv.anode_{(<T_e>)}} = 0 \tag{4.45}$$

$$f^{'}(< T_e >) = P^{'}_{\Omega}(1-\gamma)_{(<T_e>)} - P^{'}_{conv.anode_{(<T_e>)}} = 0 \tag{4.46}$$

$$< T_e >_{n+1} = < T_e >_n - \frac{f(< T_e >)}{f^{'}(< T_e >)} \tag{4.47}$$

This last formula (equation 4.47) is the resolutive formula of the power balance equation 4.26 with which it is computed the equilibrium volume mean electron temperature $< T_e >$ of the plasma in the screw-pinch. On the basis of the models that have been introduced up to now is defined

a monodimensional equilibrium model to describe the MHD pinch equilibrium that provides the equilibrium radial profiles of the magnetic field vector and of the current density vector and a zero dimensional equilibrium model to describe the plasma and neutrals thermodynamic equilibrium inside the screw-pinch. The screw-pinch thermodynamic equilibrium is computed with a power balance that requires as input the equilibrium profiles of the current density and of the magnetic field, therefore the two equilibrium models: MHD and thermodynamic must be coupled in a screw-pinch monodimensional equilibrium model that gives as result the equilibrium profiles of the thermodynamic variables taking into account the electromagnetic equilibrium profiles, solutions of the MHD equilibrium.
Such a structured model requires as inputs the boundary conditions to apply at the equilibrium profiles that can be taken as experimental data if available or as estimated data, the peak values on the pinch axis that are unknown values on which it is applied an iterative method and the axial pinch current. The experimental measurements available for the PROTO-SPHERA experiment that can be integrated inside the equilibrium model are the following:

- the mean line electron density, obtained with interferometric measurements
- the electron density and the electron temperature at the pinch boundary, obtained from measurements of the Langmuir probe
- the axial magnetic field at the plasma boundary, measured with the Hall probe
- the neutrals pressure, measured with the pump that generates the vacuum inside the PROTO-SPHERA chamber
- the pinch axial discharge current, measured with Rogowski coils
- the plasma rotation, measured with camera images
- the pinch radius, measured with camera images
- the electron temperature, measured with spectroscopes
- the radiative power, measured with diamonds detectors

From the available measurements data of the PROTO-SPHERA experiment listed above and from the equilibrium model described, a monodimensional equilibrium model of the PROTO-SPHERA screw-pinch with integrated measurements has been written in a MATLAB code. The flowchart of the mathematical and physical model that was developed in MATLAB to obtain the screw-pinch monodimensional equilibrium, is reported in figure 4.7.

As reported in the flowchart of the monodimensional equilibrium code, at the beginning are assigned as input data an interferometric measurement of the electron density profile, a neutral pressure and a plasma temperature and density measurements at the pinch edge, a measure of the axial magnetic field at the pinch edge, and other experimental measurements available as the pinch radius, the plasma rotation frequency and the axial discharge current. In succesion are then solved the MHD equilibrium code that converges on the axial current density profile assigned as input, the power balance that converges on the volume mean electron temperature, in agreement to the formula 4.47 and the code is reiterated again updating the peak value of the electron temperature

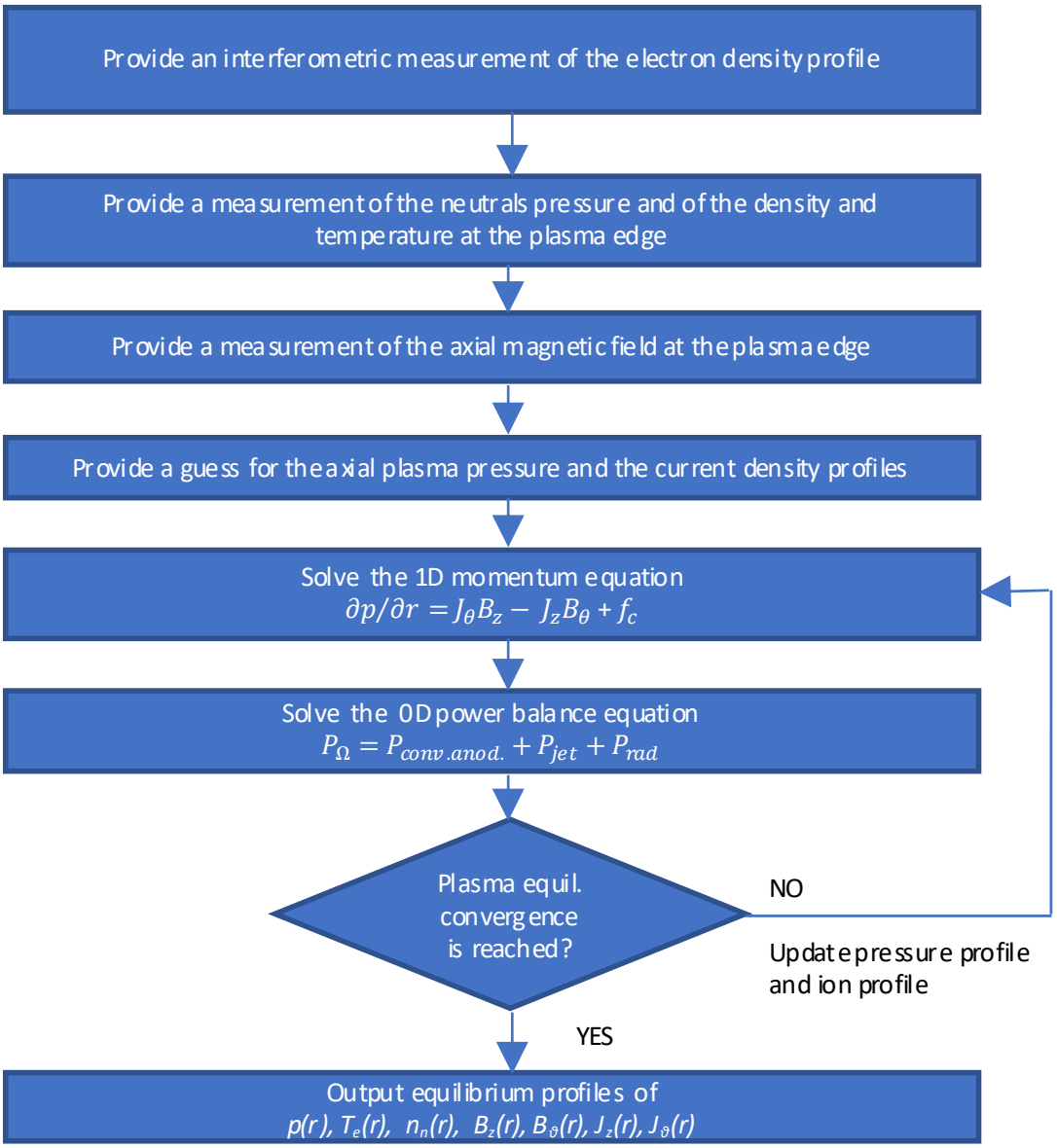


Figure 4.7: Flowchart that describes the iterative procedure theorized for the estimation of the pinch electron temperature

on the screw-pinch axis and therefore also the peak value of the plasma pressure, in agreement to the following relation up to convergence of the peaks thermodynamic variables:

$$T_{e_0}^{n+1} =< T_e >^n (\frac{\alpha}{\beta})^n [\frac{(1-e^{-\gamma})}{(1-e^{-\alpha})}]^n \tag{4.48}$$

where the superscript n and $n+1$ is referred to two successive iterations of the PROTO-SPHERA screw-pinch monodimensional equilibrium code. In figure 4.8 the obtained equilibrium profiles with the screw-pinch equilibrium code for Hydrogen and Helium are reported, where it is considered respectively a pinch axial current of $10,50kA$ and $8,50kA$, a mean line electron density of $4,18 \cdot 10^{19} particles/m^3$ and $1,80 \cdot 10^{19} particeles/m^3$ and a poloidal magnetic field at the edge of $4,69 \cdot 10^{-2}T$ and $5,86 \cdot 10^{-2}T$, an electron density at the edge of $2 \cdot 10^{18} particles/m^3$ and $3 \cdot 10^{17} particles/m^3$ and a small concentration of impurities (Nitrogen and Oxygen) and, for both cases, an electron temperature at the edge of $0,50eV$, a plasma radius of $0,30m$, a rotational frequency of $100Hz$ and a neutrals pressure of $0,10Pa$ considered at a constant ambient temperature of $293,15K$.

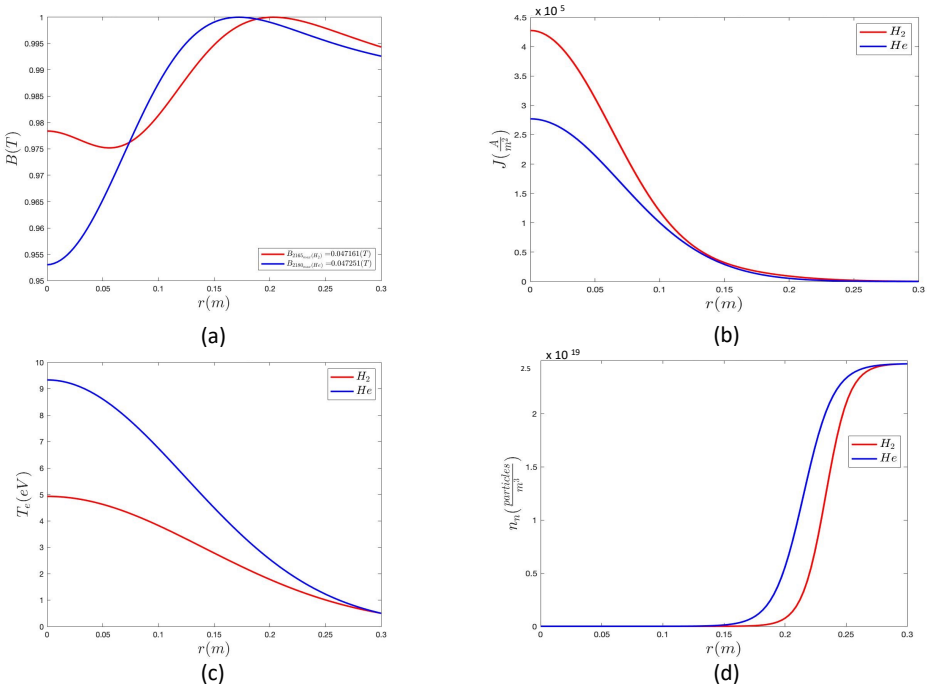


Figure 4.8: Radial equilibrium profiles of the plasma in the screw-pinch computed for two atomic species Hydrogen and Helium, in order: (a) magnetic field modulus, (b) current density modulus, (c) electron temperature, (d) neutrals density.

To evaluate our estimations, a comparison is made with the experimental data as reported in table 4.1. The comparative experimental data are obtained from previous experimental campaings, to which the researcher took part, that have been conducted on the PROTO-SPHERA experiment and the data have been given from the research group that is working on it. Electron temperature measurements are relevant for the plasma characterization and for the evaluation of the PROTO-SPHERA scaling to fusion regime. In PROTO-SPHERA temperature measurements are obtained for Helium only with a spectroscopic technique [71] and radiation measurements are made with a diamond detector that is sensible to UV radiation [72]. The estimations for the mean electron

temperature and the radiated power are in good agreement with measurements.

Specie	Shot	$I_z(kA)$	$T_{e_{num}}(eV)$	$T_{e_{exp}}(eV)$	$P_{rad_{num}}(kW)$	$P_{rad_{exp}}(kW)$
H_2	2165	10,5	2,53	N.A.	41.7	42,7
He	2180	8,5	5,66	5,5*	43,1	43,9

Table 4.1: Comparison between the numerical data (indicated with the subscript *num*) and the experimental data (indicated with the subscript *exp*). The value indicated with the asterisk * is referred to a reference value taken from the shot 1910.

4.3 2D Magnetohydrodynamic equilibrium computation of the PROTO-SPHERA experiment

The PROTO-SPHERA experiment in its magnetic configuration of screw-pinch and spherical torus can confine magnetically a plasma. A continuous plasma expulsion from the inside of the magnetic configurations would make to operate the PROTO-SPHERA experiment as a plasma thruster. The plasma can be generated both by ionization of neutral atoms with ohmic heating and by radiofrequency heating or by nuclear fusion reactions that can be confined within the PROTO-SPHERA experiment in its future fusion configuration. To study this propulsive behaviour of the PROTO-SPHERA experiment it is necessary to compute the magnetohydrodynamic equilibrium both in a fusion and non fusion regime, to compute the plasma state inside the magnetic configuration from which it is determined the propulsive performance obtained from the plasma thruster. The plasma thruster is modelled in a similar way to what made in the paragraph 4.2 [62], with a MHD equilibrium model that describes the plasma electromagnetic equilibrium, a power balance that describes the plasma thermodynamic equilibrium and a model for the charged particles emission that make the propulsive jet that generates the thrust of the plasma thruster. For each of these models that make the global design model of the plasma thruster based on the PROTO-SPHERA experiment will be dedicate a following section.

4.3.1 The MHD equilibrium code (LIBRA v 1.0)

The MHD equilibrium code computes the Grad-Shafrnov equation solution, which derivation is introduced in the paragraph 2.6 and the applied method for the solution computation is based on an approach already introduced in [73]. There are two typologies of the Grad-Shafranov equation solution: free boundary and fixed boundary. The computation of the fixed boundary solution assumes a fixed plasma geometry and the plasma boundary is assigned. The solution is computed in the domain contained inside the plasma boundary, while the free boundary solution does not assume a pre-assigned geometry of the plasma boundary, but given the coils position that make the vacuum magnetic field, with assigned currents, and the plasma peak pressure it is computed the equilibrium magnetic configuration geometry reached by the plasma. The general solution for the computation of the plasma equilibrium is the free boundary solution, because it does not assume a pre-defined plasma boundary but the plasma geometry is computed as function of the confinement magnetic field and of the plasma equilibrium, therefore it is the more general approach that can be treated and is considered in this study.
The differential equation to be solved (equation 2.90) is:

$$\frac{\partial^2\Psi}{\partial r^2} - \frac{1}{r}\frac{\partial\Psi}{\partial r} + \frac{\partial^2\Psi}{\partial z^2} = -\mu_0 r^2 \frac{dp}{d\Psi} - \mu_0^2 f \frac{df}{d\Psi} \tag{4.49}$$

that is the the equilibium MHD equation of the plasma fluid $J \times B = \nabla p$ rewritten with respect to the poloidal flux function Ψ and to the current density flux f. This equation is a second order partial differential equation axisymmetric and non homogeneous, written in a cylindrical reference system and in the international reference system (SI). The source terms of the differential equation, that are the pressure gradient p and the function f gradient, are functions themself of the indipendent variable Ψ of the differential equation and they make the differential equation non linear. The

solution method of the free-boundary Grad-Shafranov equation that is proposed in this study is based on assigning predefined distributions of the source functions and on a linearization of the Grad-Shafranov equation by means of an iterative method applied to the solution computation. It is assumed that the source functions have the following functional analytical expressions [73]:

$$p(\Psi) = p_0 \hat{p}(\tilde{\Psi}) \tag{4.50}$$

$$\frac{1}{2} f^2(\Psi) = \frac{1}{2} f_0^2 [1 + \alpha_g \hat{f}(\tilde{\Psi})] \tag{4.51}$$

where p_0 is the thermodynamic peak pressure of the confined plasma, $f_0 = R_0 B_{\phi 0}$ is the product of the magnetic axis radius and of the toroidal magnetic field on the magnetic axis, α_g is a constant that is updated at each iteration that allows to respect the constraint of total plasma toroidal current I_P assigned and $\tilde{\Psi}$ is the normalized poloidal flux function defined in agreement to the following formula:

$$\tilde{\Psi} = \frac{\Psi - \Psi_0}{\Psi_B - \Psi_0} \tag{4.52}$$

where Ψ_B and Ψ_0 are the values of the poloidal flux function at the plasma boundary and on the magnetic axis. The functions $\hat{p}(\tilde{\Psi})$ and $\hat{f}(\tilde{\Psi})$ are instead defined as polynomials of the function $\tilde{\Psi}$:

$$\hat{p}(\tilde{\Psi}) = \tilde{\Psi}^{n_1} \tag{4.53}$$

$$\hat{f}(\tilde{\Psi}) = \tilde{\Psi}^{n_2} \tag{4.54}$$

with appropriate polynomials exponent n_1 and n_2 that can be chosen also on a fitting of the functions p and f made on a known plasma equilibrium distribution. The equation 2.90 can be rewritten in a compact form introducing the elliptic toroidal operator:

$$\Delta^* \Psi = \frac{\partial^2 \Psi}{\partial r^2} - \frac{1}{r} \frac{\partial \Psi}{\partial r} + \frac{\partial^2 \Psi}{\partial z^2} \tag{4.55}$$

and the toroidal plasma current density 2.88:

$$J_\phi = r \frac{dp}{d\Psi} + \frac{\mu_0}{r} f \frac{df}{d\Psi} \tag{4.56}$$

obtaining therefore the compact expression of the Grad-Shafranov equation:

$$\Delta^* \Psi = -\mu_0 r J_\phi(r, \Psi) \tag{4.57}$$

This differential equation is solved linearizing the source function and iterating on the computation of the differential equation solution obtained with the MATLAB pdetoolbox. The compact expression of the linearized differential equation is the following:

$$\Delta^* \Psi^{n+1} = -\mu_0 r J_\phi(r, \Psi)^n \tag{4.58}$$

where with n and $n+1$ are indicated two successive iterations in which it is computed the

differential equation solution in terms of the distribution of the function Ψ in the computation domain. Assigning the source function of the n iteration to the $n+1$ iteration allows to assume in the solution computation of the differential equation 4.58 a known distribution of the function J_ϕ, computed from a first guess distribution at the initial iteration $n = 1$, eliminating therefore the non linearity of the differential equation. The differential equation 4.58 needs appropriate boundary conditions to be solved, in the case of the free boundary solution of the Grad-Shafranov equation the boundary conditions assigned at the boundary of the computation domain are computed as superpositions of the vacuum magnetic field generated by the coils distribution that surround the plasma and the magnetic field generated by the plasma itself. Since the independent variable with respect to which is solved the differential equation 2.90 is the variable Ψ, the boundary conditions of the computation domain are assigned as distribution of the variable Ψ on the plasma boundary. The variable Ψ at the plasma boundary is computed by means of the Green function [73] that allows to compute the solution of the Grad-Shafranov equation 4.57 and it is defined as:

$$G(r, r') = \frac{\mu_0}{2\pi k}\sqrt{rr'}[(2 - k^2)K(k^2) - 2E(k^2)] \tag{4.59}$$

where $K(k^2)$ and $E(k^2)$ are complete elliptic integrals of the I and II order and k, that in this case is the argument of the elliptic integral, is defined as:

$$k^2 = \frac{4rr'}{[(r + r')^2 + (z - z')^2]} \tag{4.60}$$

where μ_0 is the vacuum magnetic permeability, (r, z) are the coordinates of the generic point at the plasma boundary, (r', z') are the coordinates of the generic point in which flows a current that generates a distribution different from zero of the poloidal flux function Ψ. In agreement to these definitions the distribution of the poloidal flux function at the plasma boundary Ψ_B is computed with the following formula:

$$\Psi_B(r, z) = \int_{V_P} G(r, z, r', z')J_\phi(r', z')dr'dz' + \sum_{i=1}^{N_c} G(r, z, r_i^c, z_i^c)I_i \tag{4.61}$$

where the integral on the second member indicates the contribution to the Ψ_B distribution given from the plasma current contained in the volume V_P, while the summation at the second member indicates the contribution to the Ψ_B distribution given from the current I_i that flows in the i-th coil positioned in the coordinate (r_i^c, z_i^c). In this expression 4.61, while the contribution to the Ψ_B of the vacuum magnetic field coils stays constant during the resolution iterations of the MHD equilibrium, the contribution of the plasma current in the volume V_P changes at each iteration and it is updated as function of the solution computed for the function Ψ. The Ψ function distribution is obtained from the numerical solution of the equation 4.58, computed with the finite elements method of the MATLAB pdetoolbox [36]. Given the distribution of the poloidal flux function Ψ is possible to compute the dimensionless distribution $\tilde{\Psi}$ (equation 4.52) for which it is necessary Ψ_0 and Ψ_B as dimensionless values, that are the values of the poloidal flux function on the magnetic axis and at the plasma boundary respectively. The poloidal flux function Ψ is characterized by a minimum of its value on the magnetic axis, therefore from this condition Ψ_0 is computed. The computation of the Ψ_B value, that is the poloidal flux function at the plasma boundary is more complex and it requires to distinguish between two plasma boundaries: the plasma limiter and the plasma divertor.

In the plasma limiter the plasma boundary is defined from the first contact point between the confined plasma and the solid wall that containes the plasma, while in the divertor plasma the plasma boundary is defined as the last closed line of the poloidal flux function, that is called plasma separatrix because it separates the region of poloidal flux lines closed to the one of poloidal flux lines opened. The plasma separatrix for a plasma divertor is characterized by an X point of null poloidal magnetic field, that for the geometry of the poloidal flux lines is also a saddle point in the poloidal plane of the poloidal flux function. Therefore in the case of plasma limiter the value of the poloidal flux function at the plasma boundary Ψ_B is computed as the minimum value of the function Ψ on the contact line with the solid wall that contains the plasma, that is a method that is applied both for the pinch magnetic configuration and for the tokamak magnetic configuration because the expected trend of the Ψ function is crescent from the magnetic axis towards the plasma boundary. In the case of the divertor plasma instead, that is a typical plasma geometry in a tokamak, the plasma boundary is defined looking for the last closed line of the confined plasma and therefore calculating the position of the X point of null poloidal magnetic field with the condition that this is a saddle point and that therefore $|\nabla\Psi(r_x, z_x)| = 0$ and the hessian matrix $H(\Psi(r_x, z_x)) < 0$ computed in the coordinates of the null point (r_x, z_x), as already made in [74].
The updating parameter of the solution at the successive iteration is the parameter α_g, contained in the definition of the source function f, and it is computed imposing the condition of assigned total toroidal plasma current:

$$I_P = \int_{V_P} J_\phi(r,\Psi)drdz = \int_{V_P} (r\frac{dp}{d\Psi} + \frac{1}{\mu_0 r} f\frac{df}{d\Psi})drdz = \sum_i \sum_j (r_i\frac{dp}{d\Psi} + \frac{1}{\mu_0 r_i} f\frac{df}{d\Psi})drdz \qquad (4.62)$$

where in the previous expression the surface integral is transformed in a double summation made on the computation grid and considering the functional profiles assigned for the sources functions 4.50 and 4.51, it is obtained the following expression of the convergence parameter α_g:

$$\alpha_g = \mu_0 \left[\frac{\frac{I_P}{drdz} - p_0 \sum_i \sum_j r_i \frac{d\hat{p}}{d\Psi}}{\frac{1}{2} f_0^2 \sum_i \sum_j \frac{1}{r_i} \frac{d\hat{f}}{d\Psi}} \right] \qquad (4.63)$$

At each iteration therefore, assigned the source function profiles f and p and therefore the distribution of the source function $J_\phi(r,\Psi)$, it is solved the linearized Grad-Shafranov equation 4.58 with the MATLAB pdetoolbox [36], in a similar way to what already described in the paragraph 2.6.1 where the coefficients of the differential equation are determined (equation 2.96). The MATLAB pdetoolbox [36] solves the differential equation 4.58 with a finite elements method (FEM) that can be summarized in the following points:

- division of the original domain in a series of elements;
- for each element it is substituted the original PDE problem with a set of simple equations that locally approximate the original equations. Boundary conditions are applied for the boundaries of each element. For steady state problem where the coefficients do not depend on the solution or on its gradient, as in this case, the result is a linear system of equations;
- the resulting equations and boundary conditions are assembled in a global system of equations

that models the entire problem;

- it is solved the resulting algebraic system of equations or ODE using linear solver or numerical integration respectively. The toolbox [36] internally calls appropriate MATLAB solvers for this scope.

The iterative method used to compute the linearized Grad-Shafranov equation solution is described in the following flowchart 4.9.

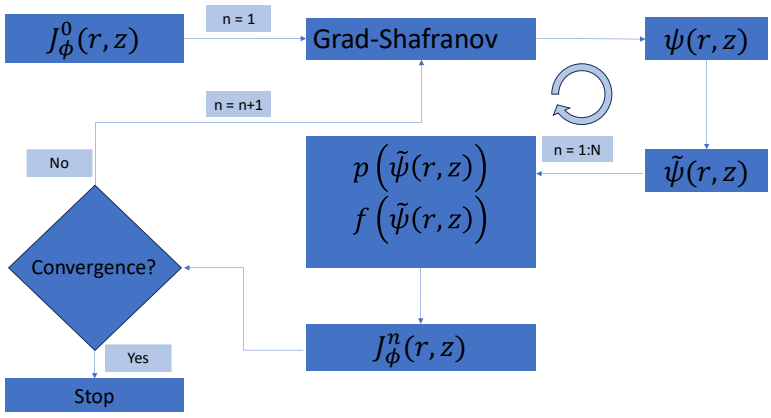


Figure 4.9: Flowchart of the resolutive algorithm of the linearized Grad-Shafranov equation

The results obtained with the MHD equilibrium code (LIBRA) are reported (figures 4.10, 4.11, 4.12, 4.13, 4.14, 4.15), with which the plasma magnetohydrodynamic equilibrium of the DTT (Divertor Tokamak Test) machine is simulated, that is currently under construction at ENEA Research Center of Frascati, using the DTT machine design data reported in table 4.2. The obtained results with the equilibrium code are compared with other results obtained with a reference code at the ENEA Research Center in Frascati that is CREATE-NL [75], obtaining a good superposition of the two solutions.

Parameter	Value
Toroidal magnetic field, B_0	-5,85 T
Toroidal current, I_T	5,5 MA
Plasma major radius, R	2,1952 m
Plasma minor radius, a	0,6947 m
Separatrix elongation, k	1,7908
Separatrix triangularity, δ	0,4395

Table 4.2: Design data table of the DTT tokamak

The images 4.10, 4.11,4.12 show a good convergence of the solution at variation of the iterations with the parameter α_g that reaches a convergence value having imposed the constraint of total toroidal current I_T assigned, that is reached. While the solution converges on these design parameters of the magnetic configuration, also the distribution of the poloidal flux function Ψ reaches a convergence distribution with a relative error computed between successive iterations that tends to zero. Images 4.13 and 4.14 instead show the distribution of the dimensionless and dimensional

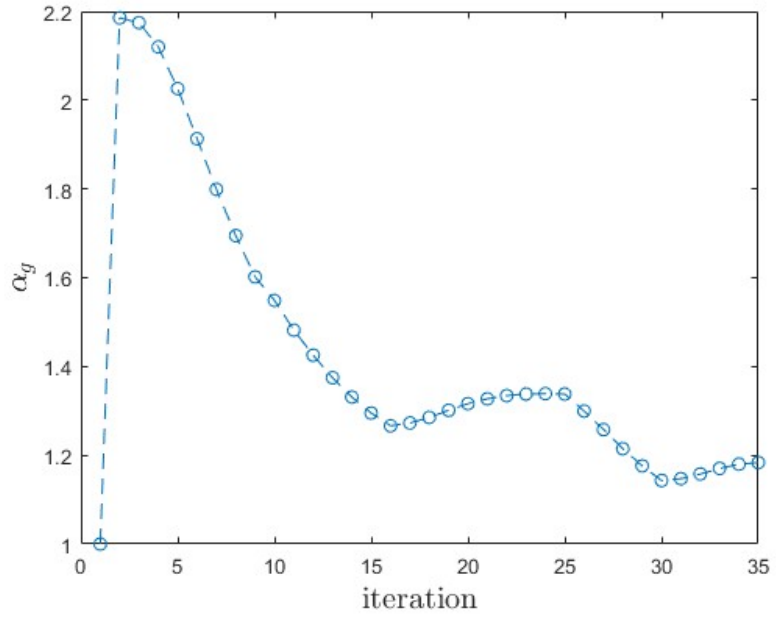


Figure 4.10: Convergence of the α_g parameter

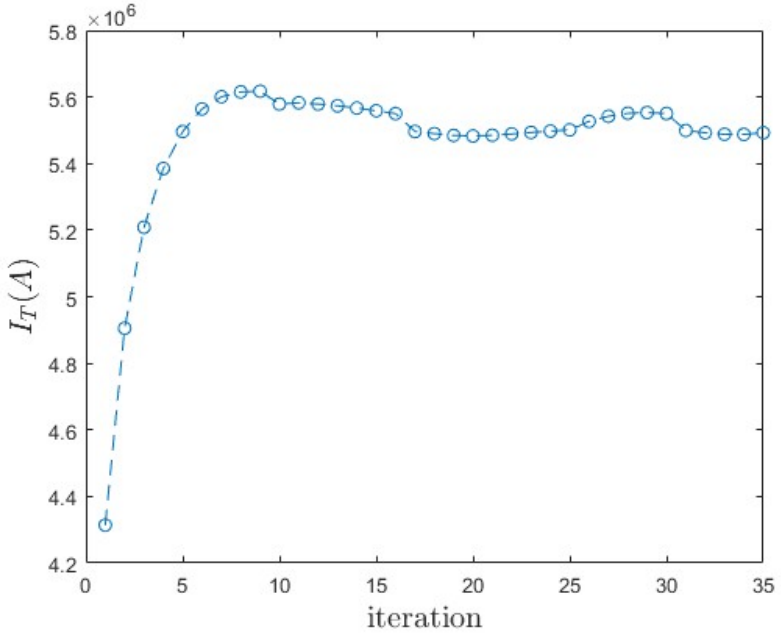


Figure 4.11: Convergence of the total toroidal plasma current I_T

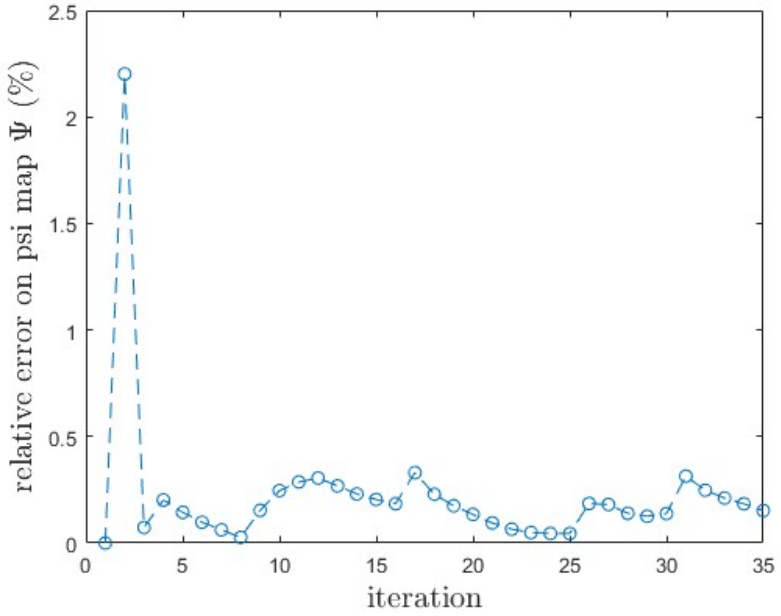


Figure 4.12: Relative error on the Ψ map

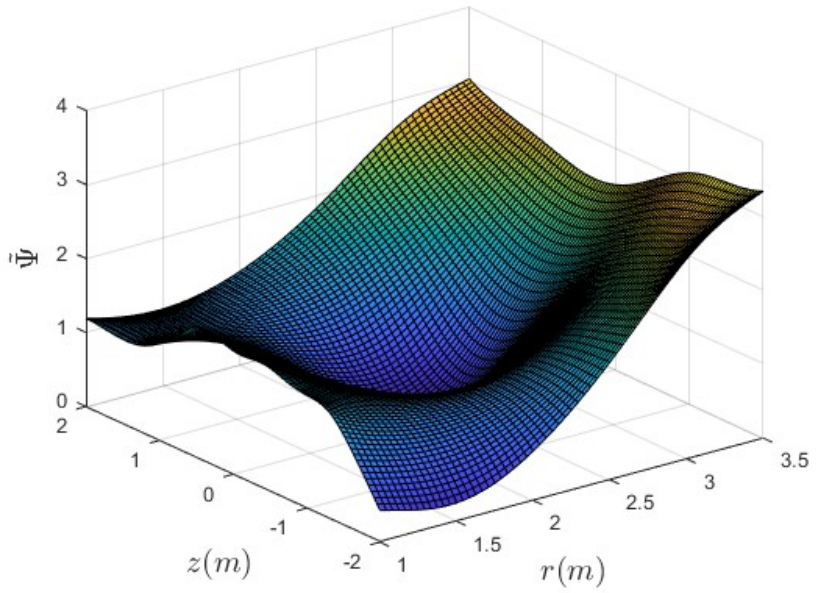


Figure 4.13: Distribution of the dimensionless poloidal flux function $\tilde{\Psi}$

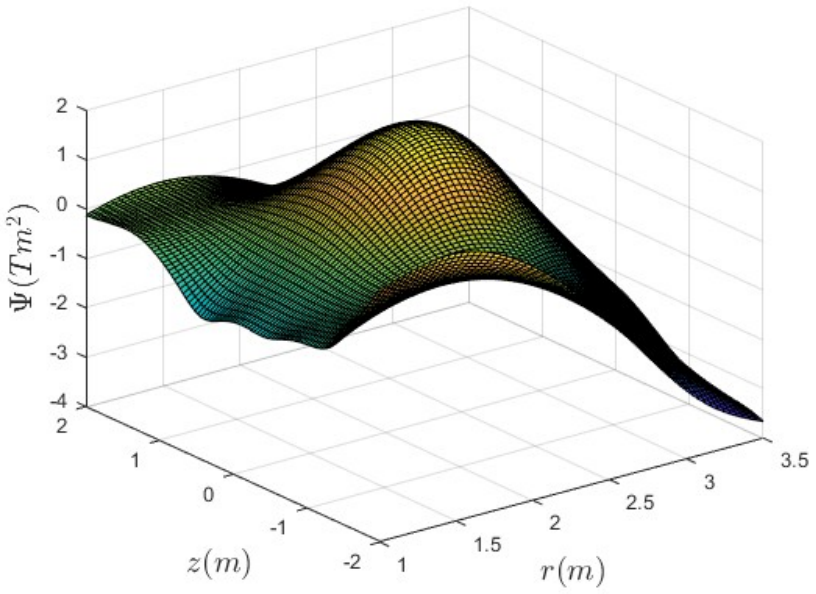


Figure 4.14: Distribution of the poloidal flux function Ψ

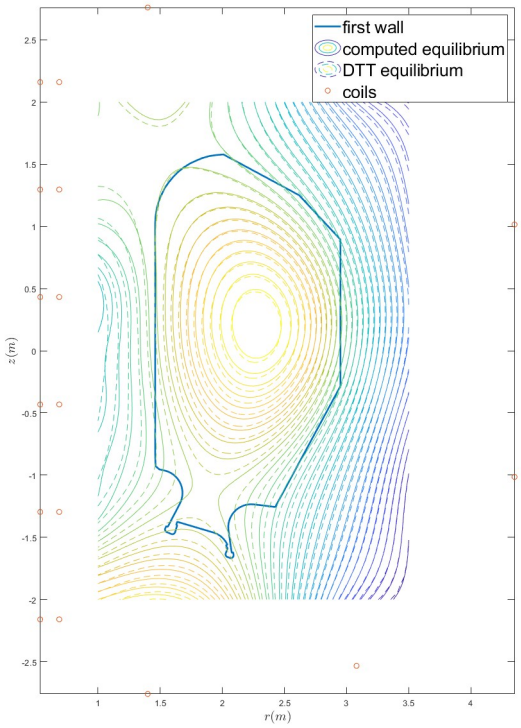


Figure 4.15: Comparison between the computed solutions for DTT with the LIBRA code and with a reference code

poloidal flux function $\tilde{\Psi}$ and Ψ in the plasma region, from which it is observed a maximum of the Ψ function in the point of the tokamak magnetic axis and a minimum in the boundary region of the plasma. The figure 4.15 show finally the comparison between the magnetohydrodynamic equilibrium solution computed with the LIBRA code and the one computed with the reference code for the DTT machine. Contour plots of the two solutions show a good superpositions of the distributions computed for the Ψ function, in particular from the contour plot of the Ψ map it is possible to see the region of confined plasma, as the plasma part contained inside the last closed line internal to the tokamak first wall. The last plasma closed line internal to the tokamak first wall (continuous blu line in figure 4.15) is also called separatrix of the confined plasma and for a divertor plasma, that is a plasma characterized by magnetic field lines partially open that go towards the bottom of the first wall, it is identified by an X point that is a saddle point of the poloidal flux function Ψ and it is a null point of the poloidal magnetic field. Also the comparison of the separatrix computation and therefore of the confined plasma boundary show a good superposition of the two computed solutions and overall the equilibrium code can reproduce the plasma magnetic configuration in a tokamak and can be therefore extended to the study of the confined plasma of the PROTO-SPHERA experiment.

4.4 Conceptual design of a nuclear fusion thruster based on the PROTO-SPHERA experiment for interplanetary missions

One of the characteristic of the PROTO-SPHERA experiment is that it contains two X points degenerates (also called triple X points). Such triple X points have null magnetic field $B = 0$ and they are placed on the symmetry axis, on opposite sides of the machine, in the middle of both annular electrodes (illustrated in Figure 4.4). It was observed that the triple X point at the anode is capable to channel the plasma directly towards the upper side of the machine, as a charged particles jet emitted from the anode [59] and this can make the machine working as a plasma thruster.
In future fusion reactors the charged fusion products, with high energy and big poloidal Larmor radius, are directed towards the magnetic separatrix from the reacting torus towards the open field lines of the central plasma column; their expulsion from the central plasma column will be preferentially from one of the two triple X points, depending on the sign $\vec{J} \cdot \vec{B}$ in the plasma. This preferential triple X point can become the basic component of a magnetic nozzle, allowing for the use of the nuclear fusion reactor as a space thruster, while the other triple X point can be used for direct conversion energy [59]. From the simulations performed in this research on the burning plasma of the PROTO-SPHERA experiment the emission of charged particles from the torus region, in which the fusion reactions take place, towards the anode region is negligible and therefore such jet can not provide sufficiently high thrust. The considered working principle of the nuclear fusion thruster therefore is no more the one proposed in previous studies [59] but it is based on the emission of charged particles from the loss cone of the pinch.
The feasibility study of a nuclear fusion thruster based on the PROTO-SPHERA experiment is based both on the fusion thruster model that estimaes the propulsive performance and on the mission analysis that states its appropriateness for an interplanetary mission. The mission analysis chosen for the space vehicle is for an interplanetary mission from Earth to Mars and it allows to obtain the design mission requirements of the thruster as: propellant mass, total velocity increment and the orbital transfer time for an assigned thrust, specific impulse and total mass of the space

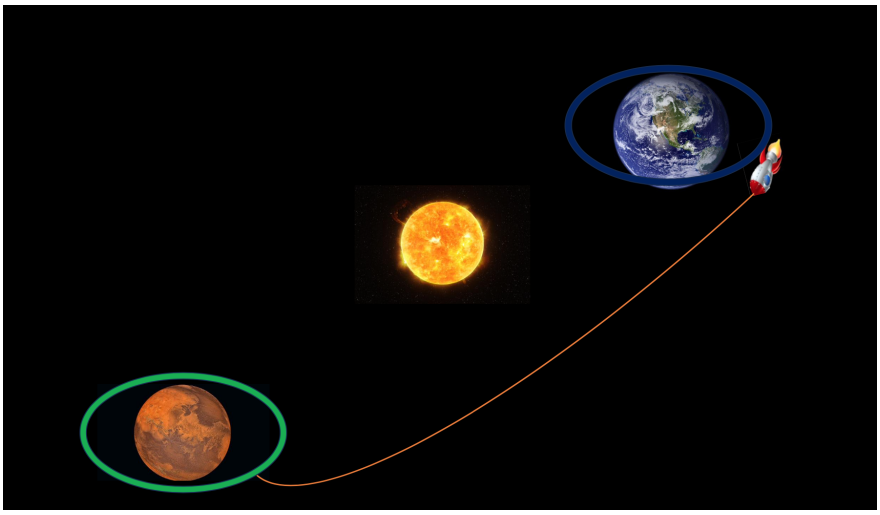


Figure 4.16: Image that shows an interplanetary transfer Earth-Mars

vehicle. From the mission analysis trajectory for an Earth-Mars transfer is obtained the total velocity increment necessary to the mission and the orbital transfer time, while from the Tsiolkovsky equation it is obtained the mass ratio of the space vehicle, for an assigned specific impulse characteristic of the nuclear fusion thruster performance, from which the mass budget can be determined assuming a given initial mass of the space vehicle. The mission analysis is made with the patched conics method that assumes that the space vehicle is under the action of the main gravitational field, and therefore there are three main part of the interplanetary trajectory: the one inside the Earth sphere of influence in which the space vehicle is subjected only to the gravitational attraction of the Earth, the one in the heliocentric reference system in which the space vehicle is subjected only to the gravitational attraction of the Sun, and the described orbit is an ellipse, and the last part inside the Mars sphere of influence in which the space vehicle is subjected only to the gravitational attraction of Mars.

4.4.1 Mission analysis of the nuclear fusion thruster

The mission analysis of the nuclear fusion thruster studies an interplanetary transfer of a space vehicle fed by nuclear fusion propulsion from Earth to Mars. The study evaluates the feasibility of such interplanetary transfer for a given propulsive performance of the fusion thruster (T, I_{sp}), that is taken from the simulation results obtained in this research project, and for an assigned initial mass of the space vehicle (m_0), starting from a low Earth orbit, that can be or the last stage of a launcher or the payload injected in Earth orbit by a launcher. The performance parameters of the nuclear fusion thruster are expressed in terms of thrust (T) and specific impulse (I_{sp}) and they are reported with the other mission design parameters in table 4.3.

The interplanetary transfer trajectory is obtained with the method of the patched conics assuming that the space vehicle is subjected only to the attraction of the gravitational field of the closer celestial body and that it can exert a continuous thrust in the trajectory arch in which it is required. Before describing the resolutive method of the patched conics applied for the interplanetary Earth-Mars transfer, a computation of the Hohmann interplanetary transfer is made that allows a first estimation of the interplanetary transfer velocity that is required by the space vehicle to exit from

Parameter	Value
Input	
Thrust, T	2 kN
Specific impulse, I_{sp}	8000 s
initial mass, m_0	$10^6 kg$
height of the initial orbit from Earth, r_c	200 km
angular position of the probe starting from the Earth, θ_{s_0}	90^o
angular position of the Earth at the departure, θ_{Earth_0}	0^o
velocity excess from the Earth, $v_{\infty_{Earth}}$	2,79 km/s
Output	
flight time, t_v	97,75 days
mass of propellant consumed, m_p	179,478 tons
initial shift Earth-Mars, $\Delta\theta$	17.13^o
mass ratio of the space vehicle, MR	1,219

Table 4.3: Table of the Earth-Mars mission analysis

the Earth gravitational field and to reach the Mars gravitational field. In the Hohmann transfer maneuver it is assumed that the planets orbit on coplanar circular orbits in which the Sun is positioned at the center of the orbit and they turn around the Sun with constant angular velocity and therefore of uniform circular motion. The reference system in which the Homann transfer maneuver is computed is therefore the heliocentric reference system, the Hohmann transfer maneuver is an impulsive maneuver with one firing made at the pericenter of the orbit with the orbit pericenter occupied by the inner planet in the solar system that is the Earth and a second impulsive firing made at the apocenter of the orbit with the apocenter occupied by the target planet in the solar system that is Mars. The interplanetary transfer trajectory in the heliocentric reference system computed with the Hohmann maneuver is an ellipse that has indeed pericenter on the Earth and apocenter on Mars, assuming that the planets are in conjunction with respect to the Sun. The geometry of the transfer orbit is defined assuming indeed that the Earth is at the pericenter at a distance from the Sun $r_{p_H} = R_{Earth}$ of 150 millions of kilometers, Mars is at a distance from the Sun $r_{a_H} = R_{Mars}$ of 228 millions of kilometers and the semi major axis and the eccentricity of the elliptic orbit can be computed from the following formulas:

$$a_H = \frac{R_{Earth} + R_{Mars}}{2} \tag{4.64}$$

$$e_H = 1 - \frac{r_{p_H}}{a_H} \tag{4.65}$$

From the constant keplerian orbital energy of an elliptic orbit:

$$E_H = \frac{v^2}{2} - \frac{\mu}{r} = -\frac{\mu}{2a_H} \tag{4.66}$$

writing the orbital energy at the pericenter and at the apocenter of the heliocentric orbit it is possible to determine the velocity at the pericenter and the velocity at the apocenter of the Hohmann transfer orbit, that are:

$$v_{p_H} = \sqrt{\mu_{Sun}(\frac{r_{a_H}}{r_{p_H} a_H})} \tag{4.67}$$

$$v_{a_H} = \sqrt{\mu_{Sun}(\frac{r_{p_H}}{r_{a_H} a_H})} \tag{4.68}$$

assuming that the Earth and Mars orbit around the Sun in a uniform circular motion with a velocity of $v_{Earth} = 30km/s$ and of $v_{Mars} = 24km/s$, the increment of the velocity at pericenter and apocenter (the impulsive firing) in modulus can be computed as the difference between the planet orbital velocity and the space vehicle orbital velocity on the Hohmann transfer trajectory. These impulsive velocity variations are also called ΔV_1 of acceleration at the pericenter and ΔV_2 of acceleration at the apocenter and they have the following expression:

$$\Delta V_1 = v_{p_H} - v_{Earth} \tag{4.69}$$

$$\Delta V_2 = v_{Mars} - v_{a_H} \tag{4.70}$$

For an interplanetary transfer Earth-Mars the $\Delta V_1 \approx 2,79km/s$ and the $\Delta V_2 \approx 2,64km/s$, these velocity increments correspond to the excess and the defect of velocity that the space vehicle must have, in the heliocentric reference system, with respect to the orbital velocity of the the departure planet and of the arrival planet. Considering therefore that the space vehicle is under the effect of the only solar gravitational field (heliocentric reference system) when it is outside of the Earth and Mars sphere of influence, this excess and defect of velocity can be considered as the velocity that the space vehicle has at the exit of the Earth sphere of influence and at the entrance of the Mars sphere of influence. The ΔV_1 therefore is the minimum velocity that the space vehicle must have at the exit of the Earth sphere of influence to reach inertially Mars from Earth, while ΔV_2 is the maximum velocity that the space vehicle must have at the entrance of the Mars sphere of influence to reach the planet Mars. These velocities that the space vehicle has at the boundary of the sphere of influence are higher than the orbital velocity of a circular orbit or of an elliptic orbit and therefore the described orbits within the sphere of influence of the departure and arrival planet are hyperbolas. Therefore the space vehicle in the interplanetary transfer to reach Mars must leave the Earth sphere of influence with an excess velocity $v_{\infty_{Earth}}$ at least equal to ΔV_1, from which the condition for the inertial interplanetary transfer:

$$v_{\infty_{Earth}} \geq \Delta V_1 \tag{4.71}$$

and it can arrive at the entrance of the Mars sphere of influence with a velocity $v_{\infty_{Mars}}$ at most equal to ΔV_2, from which the condition for the interplanetary transfer:

$$v_{\infty_{Mars}} \leq \Delta V_2 \tag{4.72}$$

This first Hohmann interplanetary transfer computation allows to define the trajectory parts that make the interplanetary transfer Earth-Mars that are a hyperbolic trajectory within the Earth and Mars sphere of influence and an elliptic trajectory in the solar sphere of influence and this first

result is at the basis of the patched conics method for the computation of an interplanetary transfer, and in addition the Hohmann transfer provides a first estimation of the transfer velocity that the space vehicle must reach $v_{\infty_{Earth}}$ and $v_{\infty_{Mars}}$ to arrive at the arrival planet (Mars in this case). The computation method of the interplanetary transfer that is applied in this research project is based on the patched conics but it differs from the keplerian solution of elliptic and hyperbolic orbits because in addition to the gravity acceleration the space vehicle is subjected, in the propulsive phase with constant thrust, also to the acceleration generated from the thrust of the nuclear fusion thruster, where the space vehicle has variable mass. Therefore the interplanetary transfer problem is reconducted to a two body problem, in which the space vehicle is subjected to the only gravitational force of the celestial body closer within its sphere of influence, and the system of equations that describe the motion of the interplanetary transfer is:

$$\begin{cases} \ddot{r} = -\frac{\mu}{r^2} + \frac{T}{m} \\ T = \dot{m} u_e \\ m = m_0 - \dot{m} t \end{cases} \tag{4.73}$$

This system of equations is solved in three different regions of the solar system space: the Earth sphere of influence that is a region that extends for almost 1 million of Km from the center of the Earth and in which it is predominant the Earth gravitational field and in which in the equation 4.73 ($\mu = \mu_{Earth}$), the solar sphere of influence that is the region of the solar system external to the sphere of influences of each single planet and celestial bodies contained in the solar system in which ($\mu = \mu_{Sun}$) and the martian sphere of influence that is a region around the Mars planet, that extends for almost 0.6 million Km in which it is preponderant the Mars gravitational field. Based on the mission data reported in table 4.3, the figures 4.17, 4.18 illustrate the transfer trajectory and the orbital velocity variation in the geocentric reference system. The continuous thrust trajectory in the geocentric reference system is a spiral that the space vehicle make increasing the semi major axis of its orbit and its orbital velocity, the geocentric trajectory differs significantly from an escape hyperbola because the nuclear fusion thruster has an acceleration level at the departure that does not overcome the Earth gravitational attraction, therefore the effect of the applied thrust is to increase the semi major axis of the orbit while the orbital velocity of the space vehicle decreases up to a minimum when the space vehicle acceleration overcomes the gravitational acceleration and the trajectory passes from spiralic to hyperbolic. As shown in figure 4.18 the final velocity that the space vehicle reaches at the exit of the Earth sphere of influence is lower than the velocity excess computed with the Hohmann interplanetary transfer ($v_{\infty_{Earth}}$), but this lower value is compensated with the propulsive phase in the heliocentric sphere of influence that allows anyway to reach the Mars orbit.

In figure 4.19 is illustrated the exit of the space vehicle from the Earth sphere of influence where to the velocity in the geocentric reference system is added the Earth rotational velocity around the Sun, in agreement to the following vector relation:

$$\vec{v}_{probe_{helio}} = \vec{v}_{probe_{geo}} + \vec{v}_{Earth} \tag{4.74}$$

where with the subscript $_{helio}$ and $_{geo}$ it is indicated heliocentric and geocentric respectively, and it is the expression of the absolute velocity ($v_{probe_{helio}}$) defined as the sum of the relative velocity

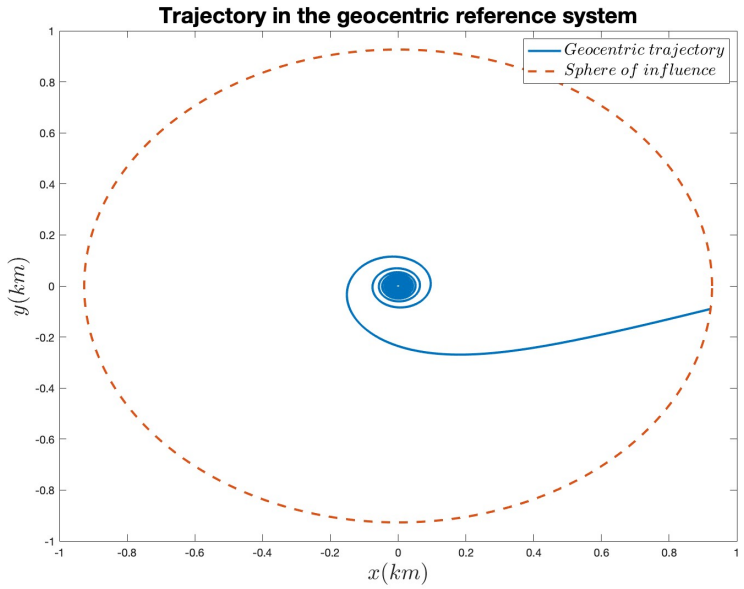


Figure 4.17: Trajectory in the geocentric reference system

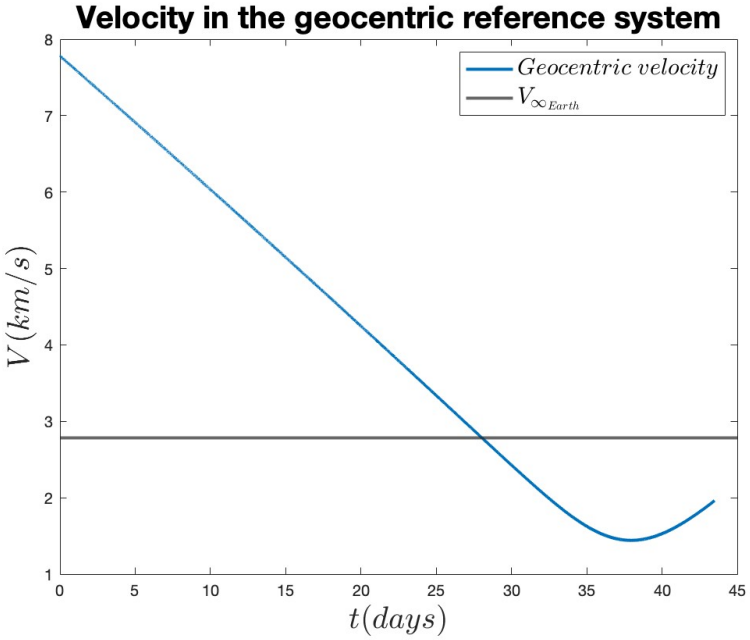


Figure 4.18: Velocity in the geocentric reference system

($v_{probe_{geo}}$) in the non inertial reference system and a dragging velocity (v_{Earth}) that is the rotation velocity of the non inertial reference system around the inertial reference system. Therefore the space vehicle velocity in the heliocentric reference system is obtained and the space vehicle once it exits from the Earth sphere of influence it enters in the solar gravitational field (Sun sphere of influence) until it reaches the Mars sphere of influence.

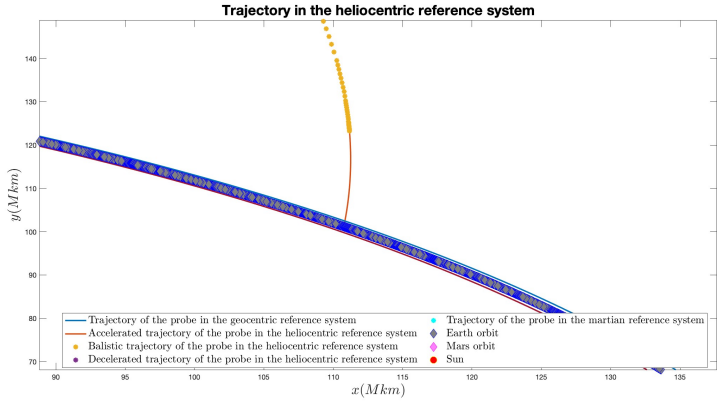


Figure 4.19: Exit trajectory from the Earth sphere of influence

In figure 4.20 is illustrated the interplanetary trajectory of the space vehicle between the Earth and Mars in which there are three distinct phases: a first accelerated phase in which the nuclear fusion thruster propels the space vehicle to reach the martian orbit, a second balistic phase in which the space vehicle is subjected only to the gravitational acceleration of the Sun and a third decelerated phase (here not necessary) that is necessary to reduce the heliocentric velocity of the space vehicle and to bring the difference between the heliocentric space vehicle velocity and the Mars orbital velocity to the velocity defect computed with the Hohmann interplanetary orbital transfer ($v_{\infty_{Mars}}$) that is the inlet velocity of the space vehicle in the Mars sphere of influence to be in Mars orbit.

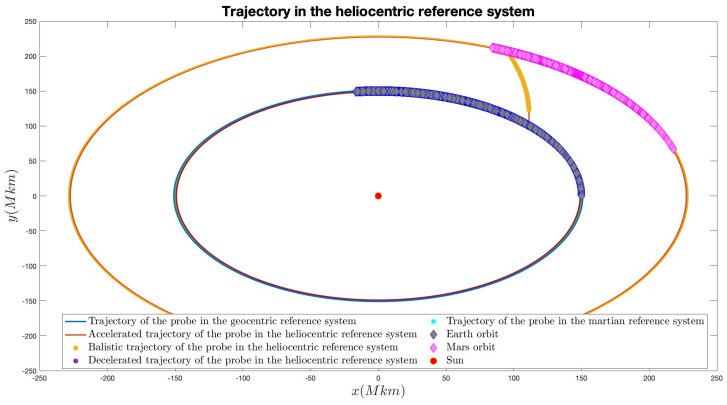


Figure 4.20: Interplanetary trajectory of the space vehicle

Figure 4.21 illustrates the entry of the space vehicle in the Mars sphere of influence that happens with a deceleration of the space vehicle, that continues to decelerate to reach the orbital circular velocity around Mars. The hypothesis made at the entry of the space vehicle in the Mars sphere of influence is that the velocity vector of the space vehicle in the martian reference system is parallel

to the direction of the Mars orbital velocity vector (condition that can be obtained with a further orbital maneuver if it is not reached at the entrance of the sphere of influence), therefore the modulus of the velocity vector at the entrance of the Mars sphere of influence is obtained from the following relation:

$$|\vec{v}_{probe_{Mars}}| = |\vec{v}_{probe_{helio}}| - |\vec{v}_{Mars}| \tag{4.75}$$

The image 4.21 show that there is a trajectory that the space vehicle describes around the Mars planet, decelerating up to the circular orbital velocity in the final point of the trajectory. Figures 4.22 and 4.23 report the orbital radius and the velocity of the space vehicle within the martian sphere of influence, from the entry of the sphere of influence up to reaching the circular orbital velocity, demonstrating that the space vehicle fed by a nuclear fusion thruster with the specified design characteristics (described in table 4.3) is capable to reach and enter in orbit around the planet Mars.

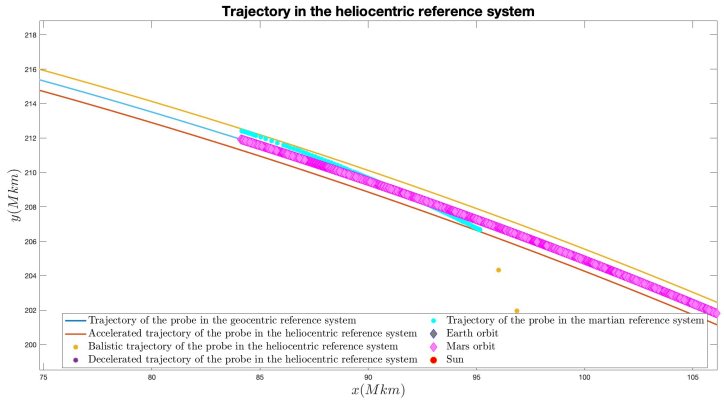


Figure 4.21: Arrival trajectory of the space vehicle in the Mars sphere of influence

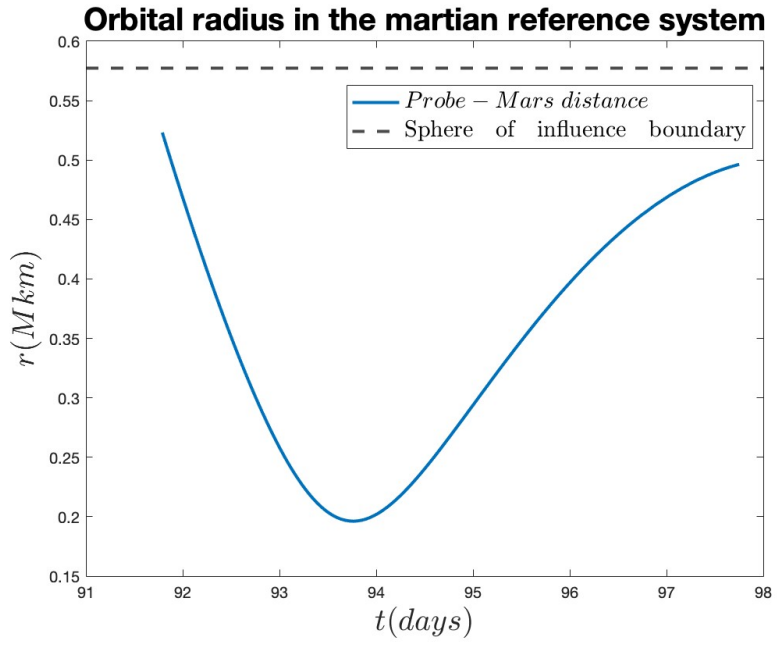


Figure 4.22: Orbital radius variation in the martian reference system

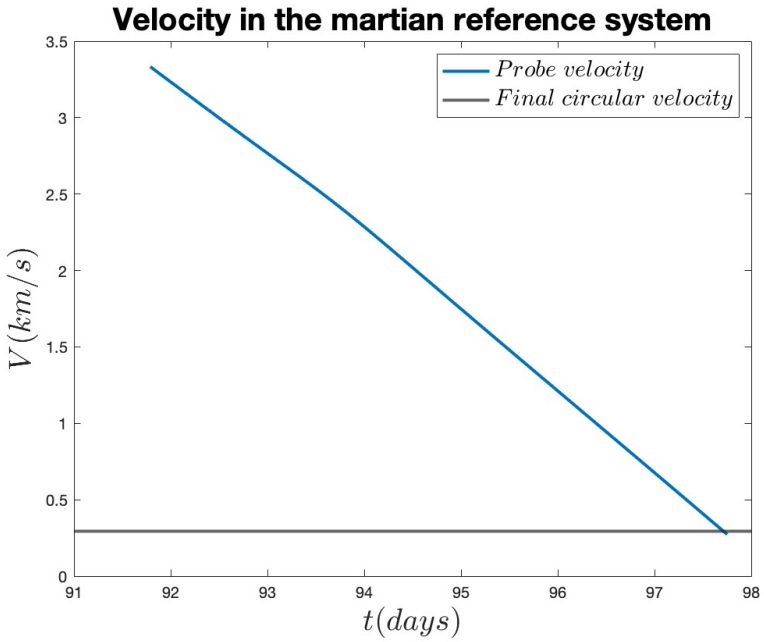


Figure 4.23: Velocity variation in the martian reference system

Figures 4.24 and 4.25 report the profiles in time of the heliocentric orbital velocity and of the total mass of the space vehicle in the interplanetary transfer, showing how the velocity and the mass vary in the various phases of the space mission. For the considered mission scenario the planet Mars can be reached in 97,75 days, with a propellant consumption of 179478 kg and the solution data are reported in table 4.3. From the propellant consumption it can be calculated also the mass ratio of the space vehicle that is a fundamental design parameter of the space vehicle that can be used to integrate it in a space launcher design.

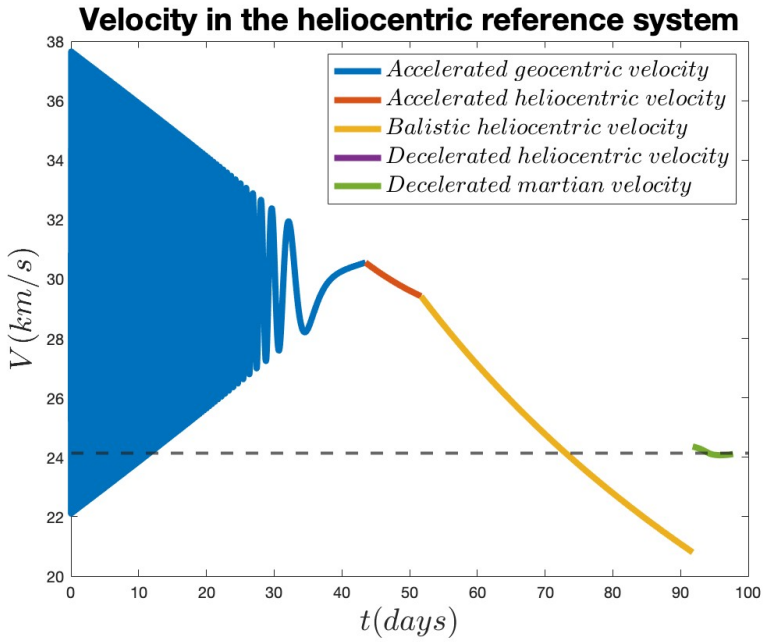


Figure 4.24: Velocity profile of the interplanetary transfer in the heliocentric reference system

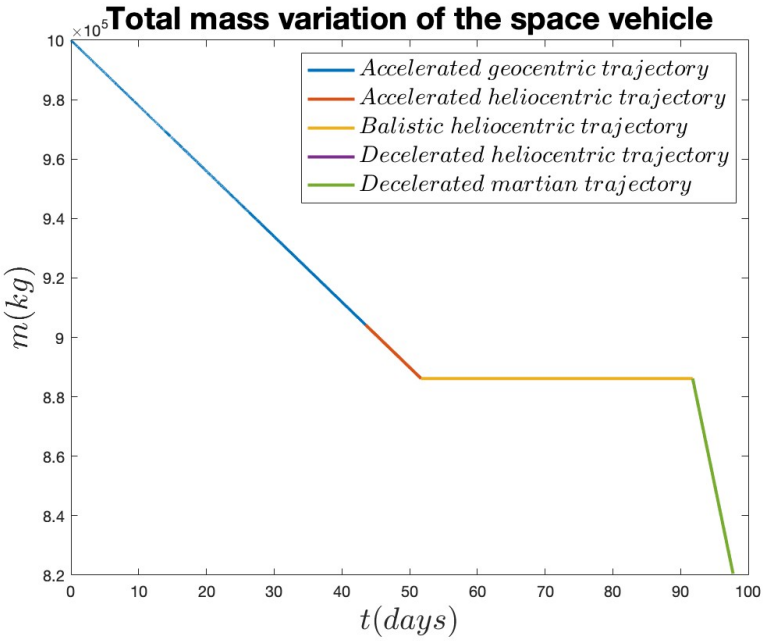


Figure 4.25: Total mass variation of the space vehicle in the interplanetary transfer

4.4.2 2D equilibrium of the PROTO-SPHERA experiment

The 2D equilibrium of the PROTO-SPHERA experiment is computed to estimate the MHD equilibrium of the magnetically confined plasma both in fusion and in non fusion regime to feed a plasma thruster. The solution of the PROTO-SPHERA equilibrium is computed with the LIBRA code (developed for this study), which solves the free-boundary Grad-Shafranov equation assigning position and current of the poloidal coils and the gradients of the source functions, therefore the gradient of the plasma pressure profile and of the toroidal magnetic field in agreement to the expressions reported in previous studies of PROTO-SPHERA [76, 77]. The LIBRA code can simulate the two equilibrium magnetic configurations of the PROTO-SPHERA experiment, the pinch and the pinch+torus, obtained already experimentally [59, 60], assigning appropriate input values, as already described in the resolutive algorithm of the LIBRA code figure 4.9, to which is added an appropriate criterion for the computation of the plasma boundary that is different for each magnetic configuration of the PROTO-SPHERA experiment.

2D MHD equilibrium of the PROTO-SPHERA screw-pinch

The MHD equilibrium of the PROTO-SPHERA screw-pinch is computed solving the Grad-Shafranov equation for a free-boundary plasma confinement problem. Positions and currents of the Group B coils (Poloidal Field 2, PF2) are assigned both in the anode and cathode region, assuming up-down symmetry of the magnetic configuration and the plasma boundary is computed imposing a condition on the poloidal flux function at the limit surface. The limit surface of the plasma confined for the PROTO-SPHERA screw-pinch is defined as the first curve of the poloidal flux function (equi-Ψ line with major radius) that passes both in proximity of the anode PF2 and in proximity of the cathode PF2. The MHD equilibrium of the screw-pinch is assumed to be a homogeneous force-free equilibrium, that is a magnetic configuration for plasma confinement with a constant pressure profile in radial direction, with a null containment Lorentz force and with two degenerate points (X points) of null poloidal magnetic field positioned on the screw-pinch axis, one on the anode and the other on the cathode. The expressions of the source functions assumed to solve the Grad-Shafranov equation and to simulate the PROTO-SPHERA screw-pinch are the following [76, 77]:

$$P(\Psi) = P_{boundary} = constant \tag{4.76}$$

$$f(\Psi) = \frac{1}{2\pi}\mu_0 I_e \frac{\Psi}{\Psi_X} \tag{4.77}$$

where I_e is the pinch axial current and Ψ_X is the value of the poloidal flux function Ψ computed at the plasma boundary. The simulation results obtained with the LIBRA code for the PROTO-SPHERA screw-pinch are reported in figure 4.26, 4.27, 4.28, 4.29, 4.30, 4.31, 4.32. The figure 4.26 shows the poloidal magnetic field vector of the screw-pinch with arrows that indicate modulus, direction and verse of the poloidal magnetic field with a trend of the vectors that is parallel in proximity of the axis and that tends to curve always more going away from the axis showing a rotational trend of the poloidal magnetic field around the field coils PF2, sources of the plasma confinement magnetic field. This rotation, with a vortex behaviour, of the poloidal magnetic field vector is the result of the Maxwell equation $\nabla \cdot B = 0$ that states that when there is a magnetic field

gradient in a certain direction, another is generated also in the others coordinates directions and the field lines (and the associated field vector) start to curve and to rotate. The highest intensity of the poloidal magnetic field is reached where the arrows that indicate the vector field are more intense, and it is in proximity of the anode and of the cathode of the screw-pinch where the simulated value of the axial magnetic field is almost 0,5 T that is exactly the experimental value obtained for the PROTO-SPHERA screw-pinch experiment.

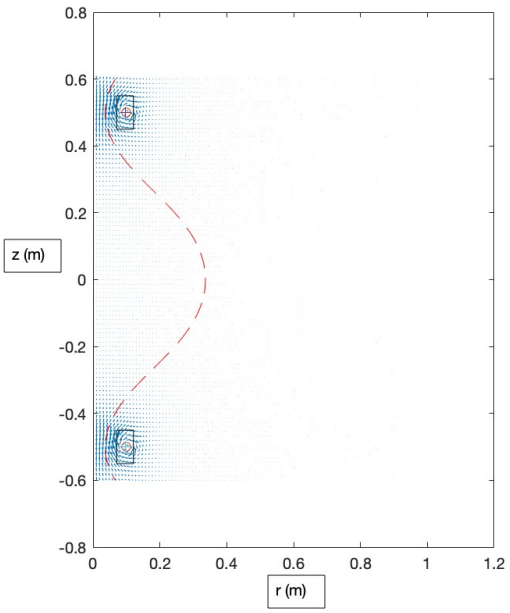


Figure 4.26: Distribution of the poloidal magnetic field of the PROTO-SPHERA screw-pinch

In figure 4.27 is instead reported the total current density of the screw-pinch in decibel simulated with the LIBRA code. The image shows that the maximum current density is in proximity of the anode and of the cathode, where the cross section perpendicular to the confined plasma axis is minimal and therefore it is maximum the current density. In the equatorial region ($z = 0$) of the screw-pinch the total current density is much lower with respect to the anode and cathode, this is because the pinch radius is maximum in the equatorial plane and because there are no high toroidal currents of the same order of the axial current.

The figure 4.28 shows the plasma pressure distribution within the magnetic configuration that, as assumed from the model of the uniform screw-pinch force-free, is constant and it is equal to the value of 10 Pa assigned as data for the simulation.

The figures 4.29 and 4.30 show respectively the countour plot of the poloidal flux function Ψ and the distribution of the dimensionless poloidal flux function $\tilde{\Psi}$ that are both maximized on the coil PF2 and they decrease moving away from the coils. In particular the contour plot of the function Ψ are closed lines described around the PF2 and from the distribution of this contour plot is determined the plasma boundary that is defined as the first contour line that passes both in proximity of the anode PF2 and in proximity of the cathode PF2, it is the dashed red line represented in figure 4.29 and it is the contour line of the poloidal flux function correspondent to the value Ψ_X indeed the plasma boundary. The function $\tilde{\Psi}$ is instead a function defined between 0 and 1 in the region in which it is contained the plasma, while it reaches values higher outside of

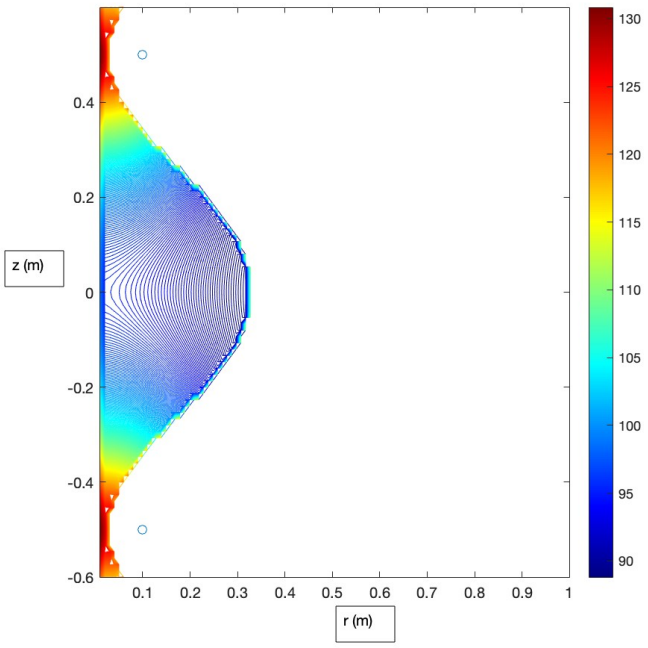


Figure 4.27: Total plasma current density distribution in dB

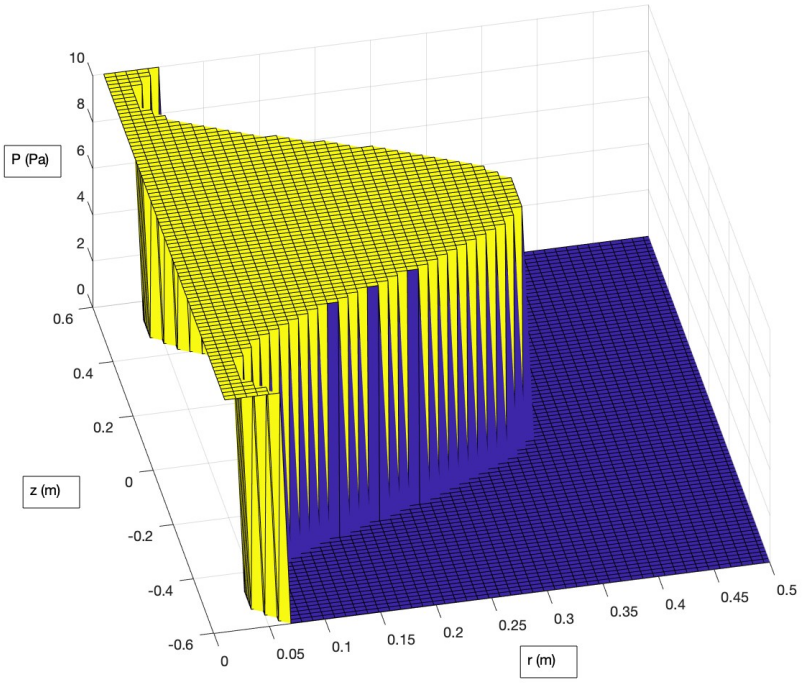


Figure 4.28: Plasma pressure distribution of the screw-pinch

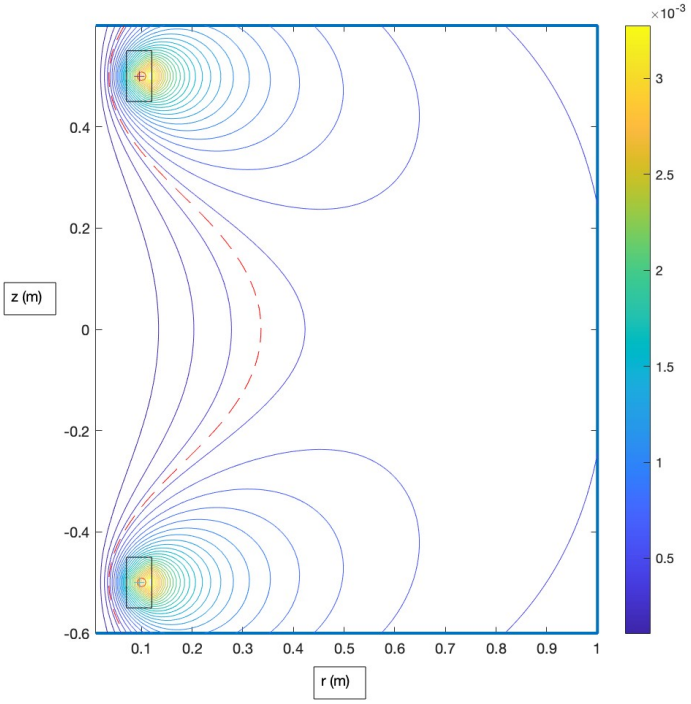


Figure 4.29: Contour plot of the screw-pinch poloidal flux function Ψ

the plasma region, as the peaks values indicated on the PF2.

The figures 4.31 and 4.32 show the convergence of the LIBRA code in the computation of the PROTO-SPHERA screw-pinch equilibrium in terms of total toroidal plasma current simulated and of error in the computation of the total toroidal plasma current at successive iterations, respectively. The code convergence in the screw-pinch simulation is very rapid, with less than 10 iterations the convergence values of the magnetic configuration are reached.

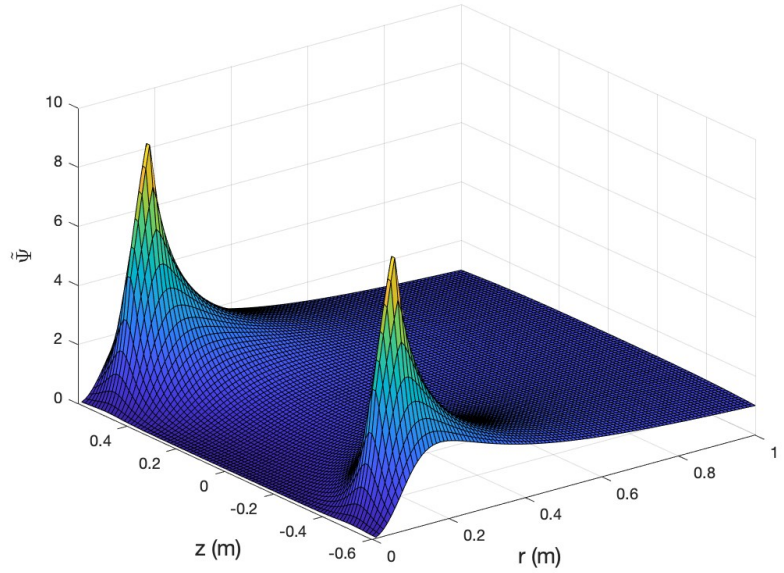


Figure 4.30: Distribution of the screw-pinch function $\tilde{\Psi}$

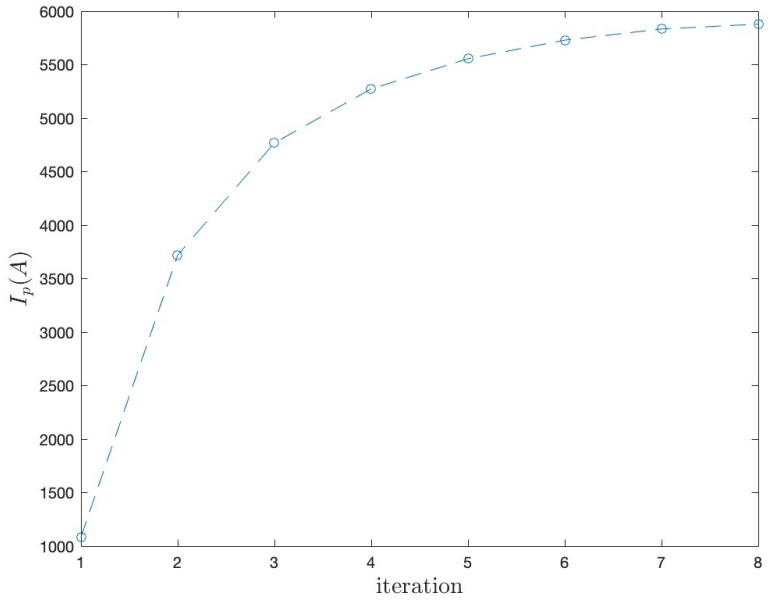


Figure 4.31: Convergence profile of the total plasma toroidal current of the screw-pinch

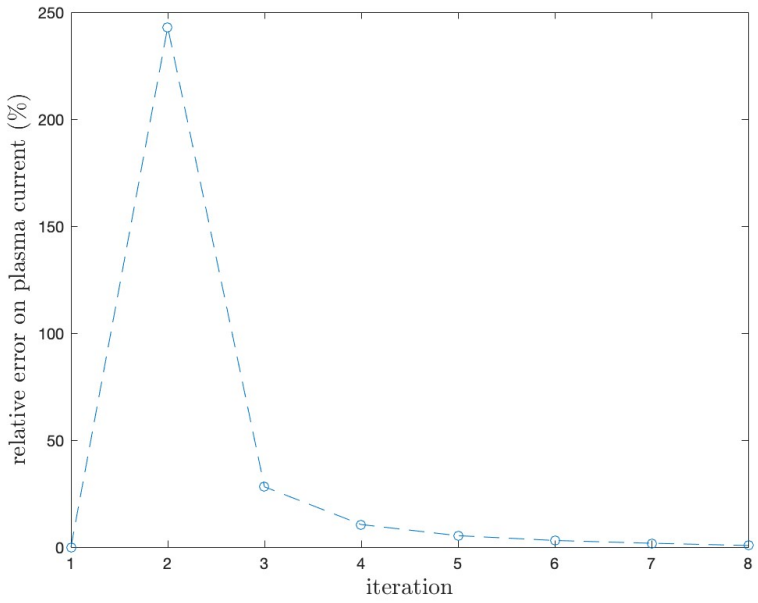


Figure 4.32: Relative error convergence on the total toroidal plasma current of the screw-pinch at successive iterations

2D MHD equilibrium of the PROTO-SPHERA pinch+torus configuration

The 2D MHD equilibrium of the PROTO-SPHERA pinch+torus is computed with the LIBRA code following the computational strategy that was illustrated in the previous paragraphs for the other equilibrium magnetic configurations computed. It is solved therefore the Grad-Shafranov equation free-boundary assigning the source functions distributions p and f in agreement to the study made on PROTO-SPHERA [76, 77], distinguishing the two regions of pinch and torus in the assegnation of the source functions, assigning the positions of the plasma confinement coils (Group A coils, Group B coils and external coils, Figure 4.33) and applying a method for the computation of the separatrix between the pinch region and the torus region, calculating therefore the boundary value of the poloidal flux function Ψ_X at the torus and pinch boundary.
The input and output values of the MHD equilibrium simulation for the pinch+torus magnetic configuration are reported in table 4.4.

The screw-pinch is modeled as a plasma homogeneous force-free MHD equilibrium, with the following profiles of the source functions assigned [76, 77]:

$$P(\Psi) = P_{0_{S-P}} = constant \tag{4.78}$$

$$f(\Psi) = \frac{1}{2\pi}\mu_0 I_e \frac{\Psi}{\Psi_X} \tag{4.79}$$

where $P_{0_{S-P}}$ is the constant plasma pressure inside the screw-pinch, I_e is the total plasma axial current between the electrodes of the screw-pinch and both data are given as input. The screw-pinch, with its source functions, is solved between the symmetry axis of the magnetic configuration and the separatrix between the pinch and the torus, therefore for values of the poloidal flux function $0 < \Psi < \Psi_X$.

Parameter	Value
Input	
I_e	15 kA
$p_{0_{S-P}}$	10 Pa
p_{0_T}	500 Pa
Output	
I_t	51,158 kA
I_t/I_e	3,41
$< \beta >$	13,2 %
$< \beta_p >$	53,15%
k	3,56
$\hat{q}$	1,43
$\hat{q}_{kink}$	1,96

Table 4.4: Table of the simulated data of the pinch+torus MHD equilibrium

The torus region, instead, is defined as the confined plasma region close to the screw-pinch that is contained in the separatrix Ψ_X that coincides with the last closed line of the poloidal flux function Ψ for the toroidal magnetic configuration. The torus is therefore computed as an MHD equilibrium magnetic configuration generated from the screw-pinch and from the poloidal coils that surround it, assuming a peak pressure p_{0_T} reported in table 4.4.The source functions assumed for the computation of the Grad-Shafranov equation solution in the torus region are the following [76, 77]:

$$P(\Psi) = P_{0_{S-P}} + C_p(\Psi - \Psi_X)^2 = P_{0_{S-P}} + C_{p_1}F_1(\tilde{\Psi}) \tag{4.80}$$

$$f^2(\Psi) = (\frac{\mu_0 I_e}{2\pi})^2 + C_f(\Psi - \Psi_X)^{1.1} = (\frac{\mu_0 I_e}{2\pi})^2 + C_{f_1}F_2(\tilde{\Psi}) \tag{4.81}$$

where the expressions have been modified with respect to the ones reported in [76, 77], with a quadratic trend for the pressure to have stable equilibria and having redefined the source functions coefficients C_{p_1} and C_{f_1} being these now function of the normalized poloidal flux function ($\tilde{\Psi}$) that goes from zero on the magnetic axis up to one on the plasma boundary:

$$\tilde{\Psi} = \frac{\Psi - \Psi_0}{\Psi_X - \Psi_0} \tag{4.82}$$

where Ψ_0 and Ψ_X are respectively the value of the poloidal flux function on the magnetic axis and at the boundary of the magnetic configuration. The coefficient C_{p_1} is computed imposing the plasma pressure at the torus center, given the pressure at the torus edge that is equal to the force-free screw-pinch pressure, while the coefficient C_{f_1} is fixed as function of the toroidal current. The results of the simulations for the PROTO-SPHERA pinch+torus equilibrium magnetic configuration obtained with the LIBRA code are reported in the following figures 4.33, 4.34, 4.35, 4.36, 4.37. The figure 4.33 show the considered geometry for the MHD equilibrium simulation of the PROTO-SPHERA experiment in the magnetic configuration of pinch+torus. In the image are reported with red circles the coils centers that generate the magnetic field of the machine and that are the Group A coils (PF1 and PF5), the Group B coils (PF2 and PF3.1) and the external coils. In addition in the image is reported in the poloidal plane the distributiom of the poloidal magnetic field for the magnetic configuration that is assumed maximum in proximity of the coils and close to the

anode and the cathode of the machine and this is obtained from the superposition of the generated magnetic fields from each coils and from the plasma. In the end in the image is illustrated with a dashed red line the boundary of the magnetic configuration, distinguishing between the screw-pinch boundary and the torus separatrix.

In figure 4.34 is reported instead an image of the countour lines of the poloidal flux function in the poloidal plane, that indicate the surfaces of equi-Ψ in the magnetic configuration that correspond to isobaric surfaces, as it can be noted also from the successive image 4.35 in which in correspondence of the minimum of the poloidal flux function (on the magnetic axis) there is plasma pressure peak. The equi-Ψ surfaces are closed curves in the poloidal plane within the torus region up to the separatrix that is identified with two X points, corresponding to the boundary value of the poloidal flux function Ψ_X, one up and one down that are also two points of null poloidal magnetic field.

The equilibrium solution of the magnetic configuration of the PROTO-SPHERA experiment pinch+torus is computed leading to convergence the LIBRA equilibrium code and in the figures 4.36 and 4.37 is reported the convergence of the simulation of the total toroidal plasma current. The code reaches convergence in almost 20 iterations with an equilibrium that has a total toroidal current $I_t = 51,158kA$ and a ratio between the torus current and the screw-pinch current $I_t/I_e = 3,41$, very close to the reference value for the PROTO-SPHERA experiment that is 4. The magnetic configuration has also a high mean poloidal dimensionless pressure $< \beta_p >= 53,15\%$, that is a value close to the ones of the spherical tokamaks [3], an elongation $k = b/a = 3,56$, therefore an elongated geometry in vertical direction and a good stability of the toroidal magnetic configuration with a safety factor higher than 1 and a safety factor for the kink instability close to 2, that is a reference value to have stable magnetic configurations, $q_{kink} = 1,96$.

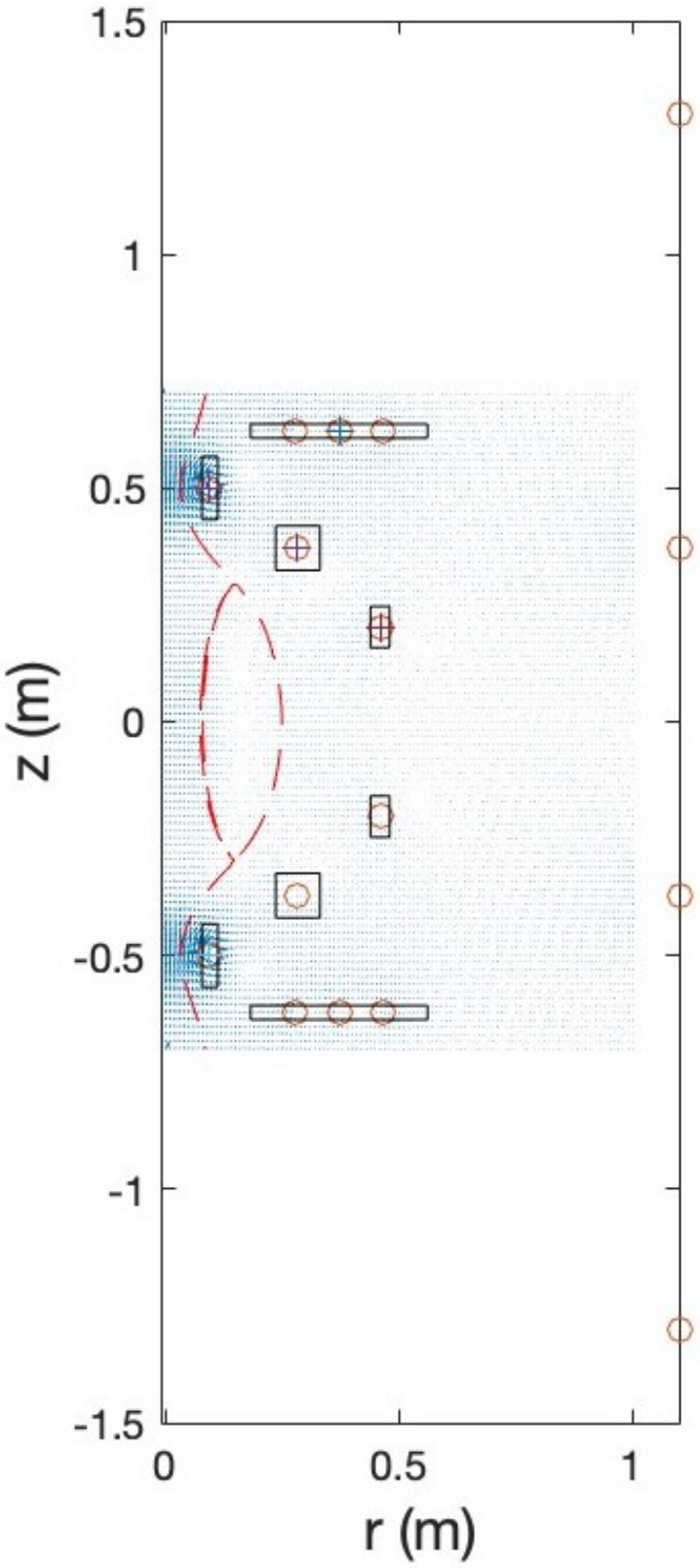


Figure 4.33: Poloidal magnetic field distribution of the pinch+torus PROTO-SPHERA MHD equilibium

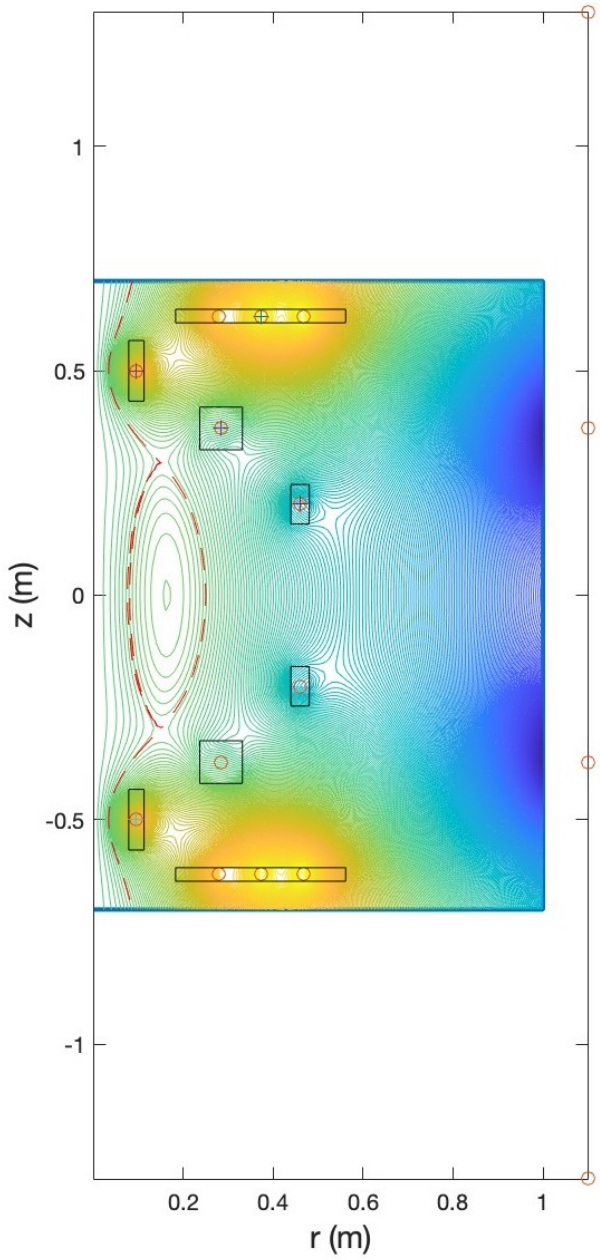


Figure 4.34: Distribution of the function Ψ of the pinch+torus MHD PROTO-SPHERA equilibrium configuration

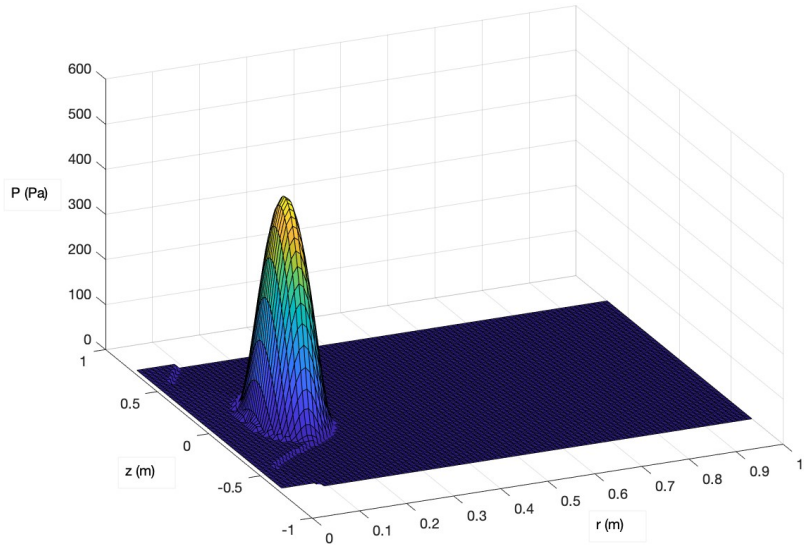


Figure 4.35: Pressure distribution of the pinch+torus MHD PROTO-SPHERA equilibrium configuration

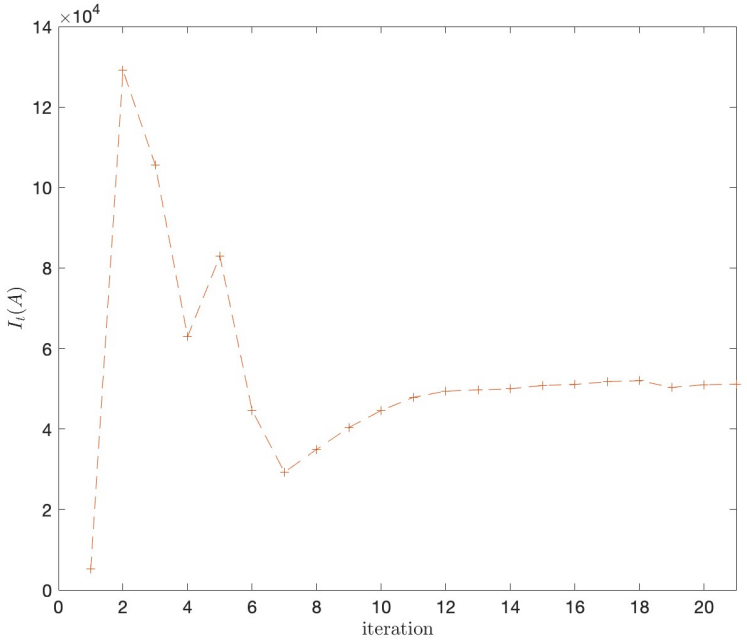


Figure 4.36: Convergence of the toroidal plasma current of the PROTO-SPHERA pinch+torus MHD equilibrium configuration

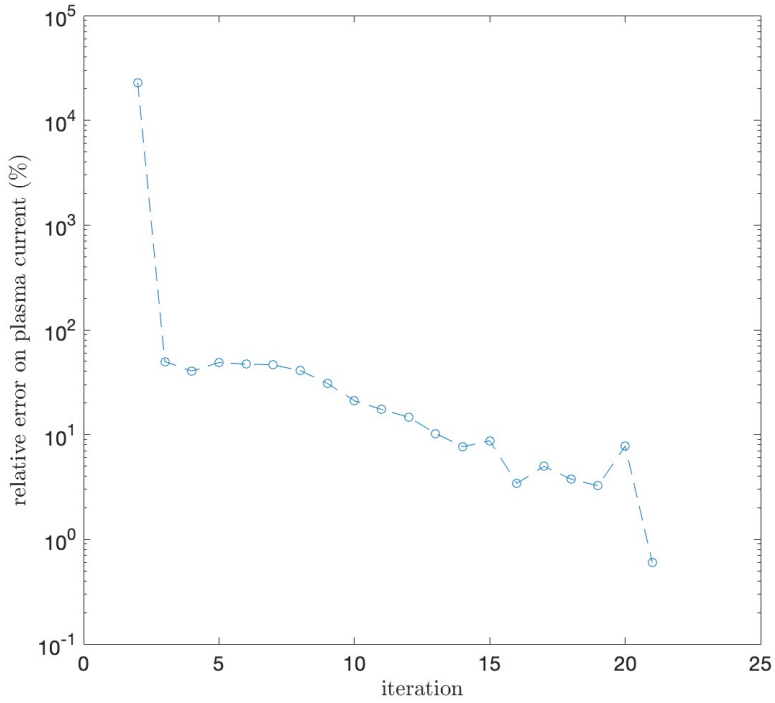


Figure 4.37: Relative error on the toroidal plasma current of the PROTO-SPHERA pinch+torus MHD equilibrium configuration

4.4.3 Fusion scaling of the PROTO-SPHERA experiment and fusion plasma thruster performance

Once the MHD equilibrium of the PROTO-SPHERA experiment has been obtained, with the LIBRA code a simulation of the PROTO-SPHERA machine with bigger dimensions is performed. The increase in dimension of the PROTO-SPHERA experiment is necessary to increase the plasma current and the plasma volume and the magnetic field that allows the machine working as a nuclear fusion reactor. The increase of the machine size, also called here scaling, is performed assuming that all the lengths of the machine scale with a "L_1" factor that is a multiplication factor for all the machine lengths, therefore the surfaces will increase with a multiplication factor L_1^2 and the volumes with L_1^3. The currents that flow in the coils of the machine and that generate the poloidal magnetic field for containing the plasma, also scale increasing the dimension of the machine and assuming that the current density in the coils is constant with the scaling of the machine, the currents in the coils scale with L_1^2. The simulated scaled configuration with the LIBRA code is then provided as input to the NUCLEUS code [20] that solves the fusion power balance of the scaled PROTO-SPHERA machine, considering a further scaling factor L_2 that is required to obtain the necessary electron temperature in the torus region of the plasma to sustain nuclear fusion reactions and the required thrust of the nuclear fusion thruster to perform the Mars mission. With these requirements it is found the minimum scaling factor $L = L_1 \cdot L_2$ that satisfies them.
Considering a value of the scaling factor $L_1 = 2$ it is determined an advanced PROTO-SPHERA machine doubled in dimensions of which is computed a stable MHD equilibrium of the magnetic configuration, that is illustrated in the following images 4.38, 4.39, 4.40, 4.41, 4.42.

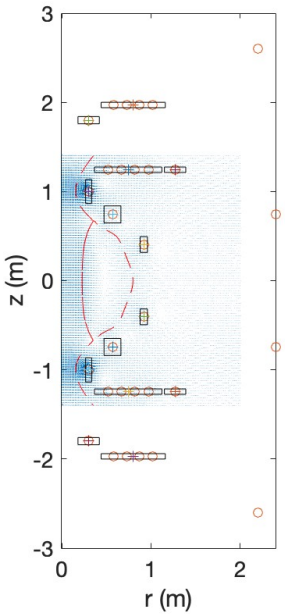


Figure 4.38: Poloidal field of the scaled non fusionist PROTO-SPHERA experiment with $L_1 = 2$

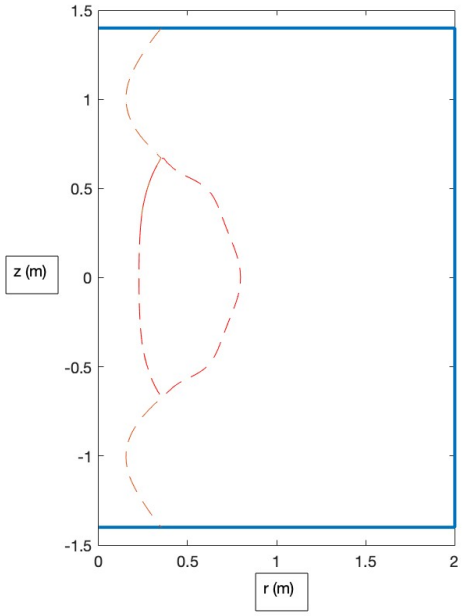


Figure 4.39: Plasma shape (separatrix) of the scaled non fusionist PROTO-SPHERA experiment with $L_1 = 2$

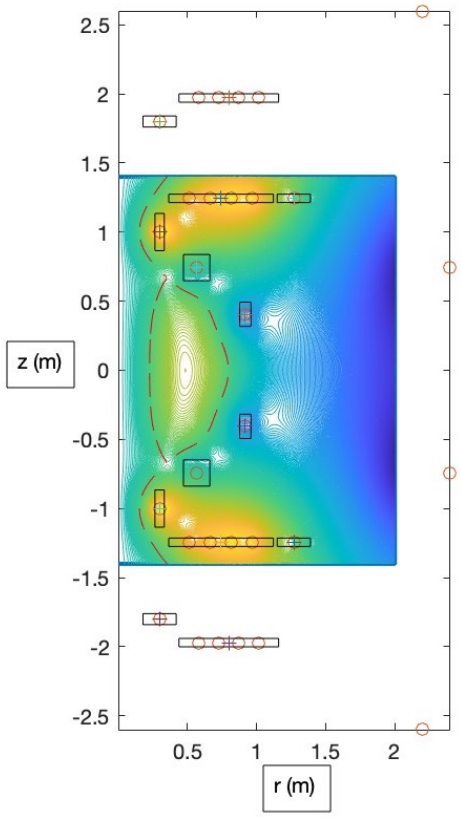


Figure 4.40: Ψ function distribution of the scaled non fusionist PROTO-SPHERA experiment with $L_1 = 2$

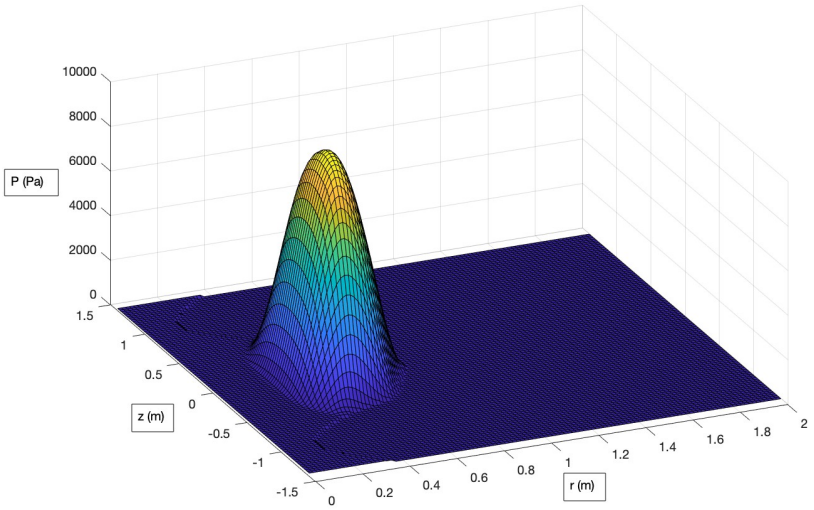


Figure 4.41: Plasma pressure of the scaled non fusionist PROTO-SPHERA experiment with $L_1 = 2$

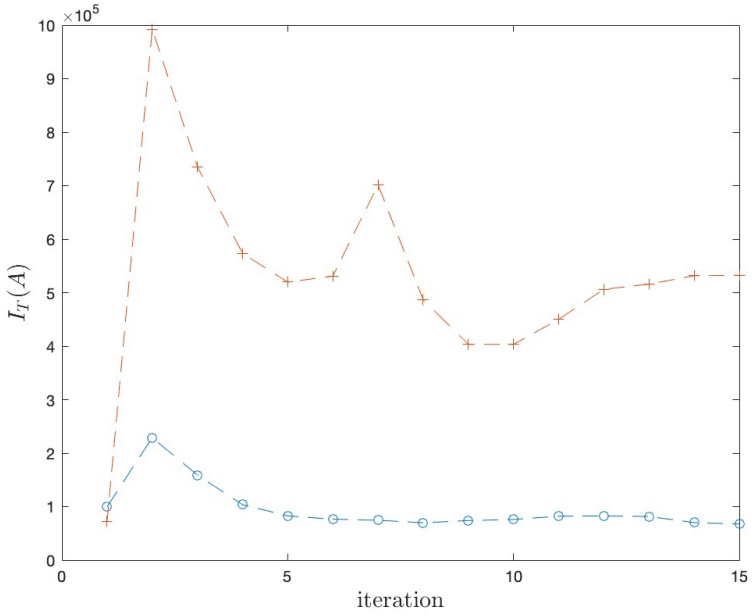


Figure 4.42: Convergence of the toroidal current (red line) and screw-pinch current (blu line) of the scaled non fusionist PROTO-SPHERA experiment with $L_1 = 2$

This initial scaled configuration of the PROTO-SPHERA experiment has the properties illustrated in table 4.5 showing that it is a stable spherical magnetic configuration, with a high $< \beta_p >= 56.69\%$ and a toroidal current of almost $0.5MA$ that make this configuration suitable to sustain fusion reactions, having a sufficient high ohmic power that is proportional to the square of the plasma current.

Initial scaling factor, L_1	2
Screw-pinch current, I_e	120 kA
Toroidal current, I_T	532,477 kA
Currents ratio, I_T/I_e	4,437
Screw-pinch peak pressure, $p_{0_{S-P}}$	100 Pa
Torus peak pressure, p_{0_T}	10 kPa
Adimensional pressure, $< \beta >$	$14,38\%$
Adimensional poloidal pressure, $< \beta_p >$	$56,69\%$
elongation, κ	2,3442
triangularity, δ	0,5758
magnetic axis radius, R_0	0,5098 m
aspect ratio, A	1,8558
Safety factor, q	1,4296
Kink safety factor, q_{kink}	1,3408

Table 4.5: Properties of the scaled PROTO-SPHERA experiment ($L_1 = 2$)

From this reference initial configuration of the PROTO-SPHERA experiment it is computed the machine scaling with the NUCLEUS code [20] in order to find the fusion scaled configuration of the machine with increased size, currents, magnetic fields that operates correctly as a nuclear fusion propulsion system. The characteristics that the enlarged machine should have are a sufficiently high volume of the plasma torus in order to produce sufficient fusion power to sustain the power balance of

the machine, an equilibrium electron temperature in the torus region that is in the temperature range that allows a sufficiently high reaction rate of the Deuterium-Tritium reactions and a sufficiently high temperature of the screw-pinch that allows to have the required thrust from the machine. The mathematical and physical model implemented in the NUCLEUS code is illustrated in the following flowchart 4.43 and it is an extended version of the power balance proposed in [41].

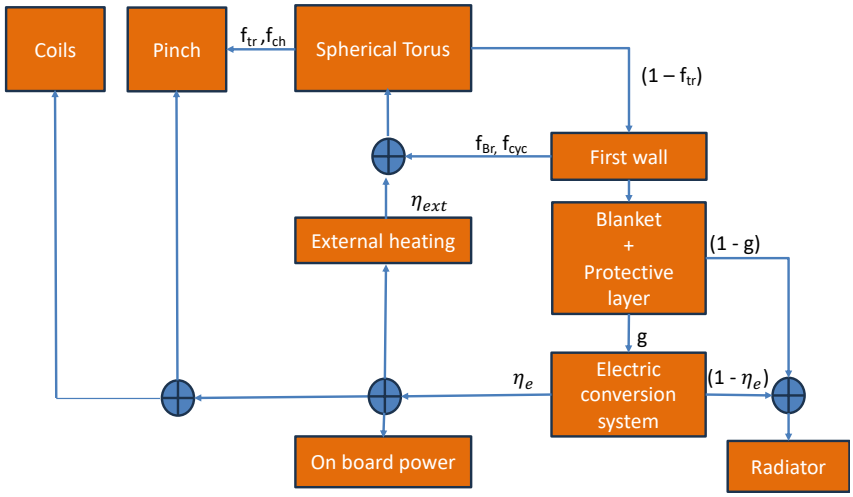


Figure 4.43: Flowchart of the NUCLEUS code for the fusion power balance

In NUCLEUS it is implemented a fusion power balance based on the power required to feed the scaled PROTO-SPHERA machine and the power that can be recovered recirculating the generated nuclear fusion power, computing therefore the minimum linear scaling factor (L_2) that allows to have self-sustainment of the engine. The power balances that are solved in NUCLEUS are two, one for the spherical torus and one for the screw-pinch, from which are computed the equilibrium electron temperatures of both regions of the plasma and therefore all the terms involved in the power balance. The power balance equation for the spherical torus is the following:

$$P_{\Omega_T} + f_{trap} P_{ch} + P_{ext} = P_{Br} + P_{cyc} + P_{tr} \tag{4.83}$$

where P_{Ω_T} is the ohmic power generated from the toroidal plasma current, f_{trap} is the fraction of charged particles power (P_{ch}) generated from the nuclear fusion reactions and trapped in the spherical torus, P_{ch} is the nuclear power of the charged particles generated in the volume of the spherical torus, P_{ext} is the external heating power given to the spherical torus, P_{Br} is the Bremsstrahlung power emitted from the spherical torus, P_{cyc} is the cyclotron radiated power and P_{tr} is the power lost from the plasma due to transport. The scaling law used in the NUCLEUS code for the computation of the energy confinement time τ_E and therefore of the power lost from the plasma due to transport, is taken from a recent study on spherical tokamaks [78] and it has the following expression:

$$\tau_E = 0,066 I_T^{0,53} B_T^{1,05} P_{abs}^{-0,58} n_e^{0,65} R^{2,66} \kappa^{0,78} \tag{4.84}$$

where I_T is the plasma toroidal current expressed in MA, B_T is the toroidal magnetic field expressed in T, P_{abs} is the total absorbed power from the plasma in the spherical torus expressed in MW, n_e is the electron density in the spherical torus expressed in $particles/(10^{19}m^3)$, R is the major radius of the spherical torus expressed in meters, κ is the elongation of the spherical torus(and it is dimensionless). The goal in the computation of the spherical torus equilibrium from the power balance is that the electron temperature reached in the torus is sufficiently high to self sustain the fusion reaction and also to heat the screw-pinch guaranteeing the thrust level required from the propulsion system. Instead, the power balance equation that solves the screw-pinch equilibrium is the following:

$$P_{\Omega_{S-P}} + P_{heat_{S-P}} = P_{S-P_{anode}} \tag{4.85}$$

where $P_{\Omega_{S-P}}$ is the input power required from the screw-pinch to generate the ohmic power associated to the input current I_e, $P_{heat_{S-P}}$ is the heating power given from the spherical torus to the screw-pinch by transport and charged particles and $P_{S-P_{anode}}$ 4.40 is the power loss to the anode. The heating power from the spherical torus to the screw-pinch is computed according to the following expression:

$$P_{heat_{S-P}} = f_{ch}P_{ch} + f_{tr}P_{tr} \tag{4.86}$$

where f_{ch} is the fraction of charged particles lost from the spherical torus towards the screw-pinch that is assumed equal to the half of the total charged particles loss and f_{tr} is the fraction of transport power loss of the spherical torus that is computed as the ratio between the surface where the two separatrices of the two plasma regions (screw-pinch and torus) are in contact and the total surface of the spherical torus separatrix. This equilibrium is computed after the computation of the spherical torus power balance, because a part of the source power is given from the spherical torus itself ($P_{heat_{S-P}}$) and to compute it the equilibrium of the spherical torus must be known. As stated previously, the goal of the computation of the screw-pinch power balance is that the thrust level is at least the one required for the space mission. When the computation is completed, the minimum fusion scaling factor (L_2) is found. In the power balance computation it is assumed that a fraction ($f_{br} = 0,10$, $f_{cyc} = 0,95$ [41]) of the radiative power emitted from the plasma towards the first wall is reflected back to the plasma with a suitable choice of the wall materials [41], while the remaining radiative, thermal and neutron power is transferred to the blanket and to a protective layer. The blanket is assumed to be a cylindrical composite porous wall, made with a layer of C (graphite as moderator to thermalize the energetic neutrons) and a layer of B_4C (as absorber of the thermalized neutrons) with a porousity of 35% for the graphite and cooled with Helium, that surrounds the plasma and that can intercept only a fraction of the power emitted by the plasma given by the view angle from the center of the magnetic configuration and it absorbs this power with an efficiency $g = 0,9$. The blanket is partially made with a fissile material (B_4C), therefore it is assumed that it increases the neutron power absorbed of almost 17% the neutron power generated by Deuterium-Tritium nuclear fusion reactions. X rays produced by the nuclear reactions with energy spectrum between 10 keV and 100 keV are absorbed by a layer of tungsten (W) with assigned thickness which is added to the blanket in order to absord this radiation. A bio-shield is made with the same principle and material of the blanket and it is positioned on the top part of the machine

to shield the habitat part of the space vehicle from the radiation emitted by the plasma. Both the power absorbed from the blanket and the protective layer (bio-shield) is given to an electric conversion system based on a Stirling cycle, with Helium as a fluid, that converts the thermal power in electrical power with an efficiency $\eta_e = 0{,}5$ that is partially given in input to the screw-pinch to sustain the arch discharge, partially provided to an external heating system (efficiency $\eta_{ext} = 0,9$) that provides the required heating input power to the spherical plasma and the power in excess is given to the on board system as extra power available for the mission. The thermal power that is not converted into electricity is assumed to be radiative power that must be dissipated with a radiator that works at an equilibrium temperature of 1000 K. From this fusion power balance the minimum fusion scaling factor L_2 is determined with which is obtained the recovered power that is at least equal to the required from the plasma to be sustained in nuclear burning phase. Once the fusion power balance is computed the masses of the main components of the fusion propulsion system are calculated: the masses of the blanket, the protective layer, the X rays absorber and the radiator are computed from the dimensions estimated with the NUCLEUS code, while for the mass of the PROTO-SPHERA experiment (structures, coils and power supply system) is assumed a reference scaling factor $\alpha_{P-S} = 79,5774 kg/m^3$ that has been further improved assuming to substitute the steel components with alluminum and the copper components with superconductor, making the structure of the machine lighter. The mass of the electric conversion system is computed assuming a scaling factor $\alpha_e = 500 W/Kg$ and the mass of the cryogenic system, necessary to cool down the superconductor coils, is computed as a fraction of the superconductor mass. From this computation a mass budget is obtained and the results are reported in table 4.6 with a total estimated mass of the propulsive system equal to 535,130 tons and an available mass for the space vehicle design equal to 464,870 tons for a total mass of the space vehicle equal to 1000 tons.

Mass	**Value**
total space vehicle mass, m_0	1000 tons
total propulsion system mass, m_{pr}	535,130 tons
PROTO-SPHERA vacuum mass, m_{P-S}	125,190 tons
blanket mass, m_b	152,430 tons
protective layer mass, m_{p-l}	20,703 tons
X rays absorber mass, $m_{X,abs}$	28,567 tons
electric conversion system mass, m_e	181,490 tons
radiator mass, m_{rad}	9,395 tons
cryogenic cooling system mass, m_{cryo}	17,357 tons
available space vehicle mass, m_a	464,870 tons

Table 4.6: Mass budget of the fusion propulsion system

The performance of the nuclear fusion thruster based on this scaled version of the PROTO-SPHERA experiment, increased with a scaling factor L, is computed assuming that a fraction of the convective power transferred from the screw-pinch to the anode that has the following expression:

$$P_{S-P_{anode}} = \frac{5}{2} J_{z0} T_e A \tag{4.87}$$

is transformed in power of the jet. Where J_{z0} is the axial current density of the screw-pinch, T_e is the electron temperature in eV and A is the screw-pinch mean cross section, with the units in SI.

The jet power is therefore computed as:

$$P_{jet} = \eta_{jet} P_{S-P_{anode}} \tag{4.88}$$

with the fraction η_{jet} of the convective power that is computed from the formula of the magnetic mirror loss cone angle (θ_{jet}) already introduced in section 4.44 assuming that only the particles contained in the loss cone towards the anode are emitted and can be ejected to form the jet, and the fraction has the following expression:

$$\eta_{jet} = H \cdot (1 - cos(\theta_{jet})) \tag{4.89}$$

where H is a correction factor of the lost particles that takes into account collisions and kinetic instabilities of the plasma and also the electric field of the screw-pinch. From this computation there are obtained the performance parameters for the scaled fusion PROTO-SPHERA machine operating as a nuclear fusion thruster that are summarized in table 4.7.

Fusion scaling factor, L_2	3,6
Total scaling factor, $L = L_1 \cdot L_2$	7,2
Thrust, T	2015,6 N
Specific impulse, I_{sp}	8110 s
Mass flow rate, $\dot{m}$	0,0253 kg/s
Thrust efficiency, η_T	16,20 N/MW
Torus equilibrium temperature, T_{e_T}	31 keV
Screw-pinch equilibrium temperature, $T_{e_{S-P}}$	41 eV

Table 4.7: Performance of the fusion plasma thruster based on the scaled fusion PROTO-SPHERA experiment

Assuming that the interplanetary flight is made at constant specific impulse, if one computes the velocity increment with the Tsiolkovsky equation the same velocity increment could be obtained with a solid chemical rocket, assuming a specific impulse of 250 s but with a mass ratio of the space vehicle equal to 580,12 reducing significantly the mass available that is not propellant.
From the results obtained with the simulation the scaled fusion machine is capable to operate as a fusion propulsion system for the selected mission to Mars, satisfying the requirements on the total mass of the propulsion system, thrust and specific impulse provided with a total mass of the stage equal to 1000 tons, a mass ratio of the space vehicle MR equal to 1,22 and a flight time equal to 97,75 days.
In conclusion, in this chapter has been performed a modeling of the nuclear fusion thruster based on the PROTO-SPHERA experiment, designing the machine required for confining magnetically the fusion plasma with a scaling of the PROTO-SPHERA magnetohydrodynamic equilibrium, from which it is computed also the nuclear fusion thruster performance. The mass budget of the designed propulsion system is obtained from a scaling of the PROTO-SPHERA masses and the feasibility of the interplanetary mission is determined with a dedicated mission analysis.

Chapter 5

Conclusion

During this PhD research period a study on two innovative concepts of electric propulsion has been performed, the helicon thruster and the nuclear fusion thruster, two plasma propulsion technologies that are of interest for space flight and interplanetary flight, based on reliable and green systems that could represent a unique solution for space missions. The main advantage in the use of such electric propulsion systems is the highest specific impulse obtainable with a moderate thrust level that makes space flight missions achievable with a low propellant consumption. This technology is still at laboratory level and must be tested in orbit in order to overcome some limitations such as the low thrust level and the high engine mass when it is scaled to high thrust levels. From the research made in this PhD project, new models have been proposed for the design of the main components both of the helicon thruster and of the nuclear fusion thruster that allow to find a suitable propulsion system for a target mission. Interesting results have been obtained on the design of helicon antennas with a model that allows to size a helicon antenna for the generation of a target plasma that can be integrated as plasma source in a helicon thruster of a given performance. Also the conceptual design of the nuclear fusion thruster based on the PROTO-SPHERA experiment of the ENEA Research Center in Frascati showed the feasibility of such plasma thruster for a space mission, with both high thrust and high specific impulse that would have interesting features as a propulsion system for interplanetary missions. This last project revealed some limitations related to the high mass of the engine that is required when it scales to high thrust levels but this problem can be partially solved using lighter and more performing materials that make the system lighter. The research work here reported has been in part already published and presented at international conferences and will be part of future projects on plasma propulsion that are oriented to the design of such new propulsion systems. As a follow-up of the present research is the construction and test of a helicon antenna in the laboratory of the ENEA Research Center that then can be integrated in a helicon thruster. Meanwhile, the design of the nuclear fusion thruster is still at conceptual level and for the moment the research will continue in the study of innovative plasma magnetic confinement machines.

D. Iannarelli, F. Napoli, S. Mannori, A. De Ninno, A. Ingenito, P. Teofilatto, Plasma thruster design through a predictive model of the Proto-sphera experiment arc state, Symposium SYNC 2022, Sapienza University, Roma 20-23 June 2022.

D. Iannarelli, F. Napoli, F. Alladio, G. Apruzzese, F. Bombarda, P. Buratti, J. Delfini, A. De

Ninno, F. Filippi, D. Fiorucci, A. Ingenito, S. Mannori, P. Micozzi, P. Teofilatto, A new indirect measurement method of the electron temperature for the Proto-sphera's pinch plasma, Journal of Instrumentation, 18, 04, C04017, IOP Publishing, 2023.

D. Iannarelli, F. Napoli, A. De Ninno, A. Ingenito, S. Mannori, A Nagoya type-III antenna designed for a space thruster, 2nd International Conference on Aerospace and Aeronautical Engineering, Firenze 21-23 March 2024.

D. Iannarelli, F. Napoli, A. Ingenito, A. Cardinali, A. De Ninno, S. Mannori, A Rational Design Method for the Nagoya Type-III Antenna, Aerospace 11, 1056, MDPI, 2024.

F. Napoli, D. Iannarelli, F. Cichocki, A. De Ninno, S. Mannori, New Space Plasma Propulsion Activities in ENEA C.R. Frascati, Workshop ASI "Tecnologie spaziali per le future missioni di ASI", Roma 16-19 April, 2024.

D. Iannarelli, A. Ingenito, F. Napoli, F. Cichocki, C. Castaldo, A. De Ninno, S. Mannori, A. Cardinali, F. Taccogna, Full Helicon thruster modeling, 38th International Electric Propulsion Conference, Toulouse 23-28 June, 2024.

D. Iannarelli, F. Napoli, A. Ingenito, A. De Ninno, S. Mannori, A plasma thruster based on the screw-pinch physics, submitted to Applied Physics Journal (2025).

F. Napoli, D. Iannarelli, A. Ingenito, S. Mannori, A. De Ninno, P. Buratti, A. Cardinali, C. Castaldo, F. Cichocki, C. Di Troia, Nuclear fusion scaling of the PROTO-SPHERA experiment, submitted to 2nd European Conference on Magnetic Reconnection in Plasmas, Torino 17-19 June, 2025.

D. Iannarelli, A. Ingenito, F. Napoli, C. Castaldo, F. Cichocki, A. De Ninno, S. Mannori, A. Cardinali, Antenna optimization for helicon plasma thrusters, submitted to IEPC, London 14-19 September, 2025.

F. Napoli, F. Cichocki, A. De Ninno, S. Mannori, D. Iannarelli, A. Ingenito, Conceptual design of a nuclear fusion thruster based on the PROTO-SPHERA experiment, submitted to IEPC, London 14-19 September, 2025.

Bibliography

[1] Marco Ariola, Alfredo Pironti, et al. *Magnetic control of tokamak plasmas*, volume 187. Springer, 2008.

[2] Davide Melazzi and V Lancellotti. A comparative study of radiofrequency antennas for helicon plasma sources. *Plasma Sources Science and Technology*, 24(2):025024, 2015.

[3] Alessandro Lampasi, Giuseppe Maffia, Franco Alladio, Luca Boncagni, Federica Causa, Edmondo Giovannozzi, Luigi Andrea Grosso, Alessandro Mancuso, Paolo Micozzi, Valerio Piergotti, et al. Progress of the plasma centerpost for the proto-sphera spherical tokamak. *Energies*, 9(7):508, 2016.

[4] PL García Martínez and R Farengo. 3d numerical simulations of the dynamics of a flux core spheromak. In *4th IAEA Technical Meeting on Spherical Tori, Frascati, Italy*, 2008.

[5] PL García Martínez and R Farengo. Flux core spheromak formation from an unstable screw-pinch. In *Proceedings of the 35th EPS Conference on Plasma Physics, Hersonissos, Greece*, pages 9–13, 2008.

[6] RW Boswell. Plasma production using a standing helicon wave. *Physics Letters A*, 33(7):457–458, 1970.

[7] Francesco Romano, Y-A Chan, Georg Herdrich, C Traub, S Fasoulas, PCE Roberts, K Smith, S Edmondson, S Haigh, NH Crisp, et al. Rf helicon-based inductive plasma thruster (ipt) design for an atmosphere-breathing electric propulsion system (abep). *Acta Astronautica*, 176:476–483, 2020.

[8] HIPATIA team. Hipatia, 2023. January 24, 2025.

[9] Mark Wade. Astronautix, 2019. January 24, 2025.

[10] Aerojet Rocketdyne. Satcatalog, 2024. January 24, 2025.

[11] DARPA. Darpa, 2025. February 26, 2025.

[12] ASI. Asi, 2025. February 26, 2025.

[13] Adam Boxberger, Alexander Behnke, and Georg Herdrich. Current advances in optimization of operative regimes of steady state applied field mpd thrusters. In *36th International Electric Propulsion Conference*, pages 2019–585, 2019.

[14] Felix Schäfer, Georg Herdrich, Zhe Zhang, Christoph Montag, Rene Laufer, Fabio Santoni, Fabrizio Piergentili, Paolo Marzioli, Diego Amadio, and Lorenzo Frezza. In-orbit testing of the petrus pulsed plasma thruster on the greencube 3u cubesat. In *8th Edition of the Space Propulsion Conference*, pages SP2022–S2239, 2022.

[15] Kazunori Takahashi. Direct thrust measurement of a permanent-magnets helicon plasma thruster for space propulsion. *Fusion Science and Technology*, 63(1T):123–126, 2013.

[16] Benjamin W Longmier, Leonard D Cassady, Maxwell G Ballenger, Mark D Carter, Franklin R Chang-Díaz, Tim W Glover, Andrew V Ilin, Greg E McCaskill, Chris S Olsen, Jared P Squire, et al. Vx-200 magnetoplasma thruster performance results exceeding fifty-percent thruster efficiency. *Journal of Propulsion and Power*, 27(4):915–920, 2011.

[17] S Thomas, M Paluszek, and S Cohen. Fusion-enabled pluto orbiter and lander, niac phase i final report. *NASA Award Number: NNX16AK28G, New Jersey*, 2017.

[18] TA Bond and JA Christensen. Nstar ion thrusters and power processors. Technical report, 1999.

[19] Martin Tajmar, Carsten Scharlemann, Angelo Genovese, Nembo Buldrini, Michael Boss, Helmut Frueholz, and Rainer Killinger. Indium feep micropropulsion subsystem for lisa pathfinder. In *42nd AIAA/ASME/SAE/ASEE Joint Propulsion Conference & Exhibit*, page 4826, 2006.

[20] Francesco Napoli. Nucleus code, enea centro ricerche frascati.

[21] Jeffrey P Freidberg. *ideal MHD*. Cambridge University Press, 2014.

[22] G. Pucella and S.E. Segre. *Fisica dei plasmi*. Fisica sperimentale. Zanichelli, 2009.

[23] Francis F Chen and Donald Arnush. Generalized theory of helicon waves. i. normal modes. *Physics of Plasmas*, 4(9):3411–3421, 1997.

[24] Donald Arnush and Francis F Chen. Generalized theory of helicon waves. ii. excitation and absorption. *Physics of Plasmas*, 5(5):1239–1254, 1998.

[25] Roderick William Boswell. Very efficient plasma generation by whistler waves near the lower hybrid frequency. *Plasma Physics and Controlled Fusion*, 26(10):1147, 1984.

[26] Francis F Chen. Plasma ionization by helicon waves. *Plasma Physics and Controlled Fusion*, 33(4):339, 1991.

[27] Francis F Chen. Helicon discharges and sources: a review. *Plasma Sources Science and Technology*, 24(1):014001, 2015.

[28] Timothy Ziemba, John Carscadden, John Slough, James Prager, and Robert Winglee. High power helicon thruster. In *41st AIAA/ASME/SAE/ASEE Joint Propulsion Conference & Exhibit*, page 4119, 2005.

[29] SN Bathgate, MMM Bilek, and DR Mckenzie. Electrodeless plasma thrusters for spacecraft: a review. *Plasma Science and Technology*, 19(8):083001, 2017.

[30] Robert G Jahn. *Physics of electric propulsion*. Courier Corporation, 2006.

[31] Daniele Iannarelli, Antonella Ingenito, Francesco Napoli, Filippo Cichocki, Carmine Castaldo, Antonella De Ninno, Simone Mannori, Alessandro Cardinali, and Francesco Taccogna. Full helicon thruster modeling. *arXiv preprint arXiv:2407.21457*, 2024.

[32] Lyman Spitzer. *Physics of fully ionized gases*. Courier Corporation, 2006.

[33] Frans Hendrik Ebersohn. *Kinetic Method for Quasi-One-Dimensional Simulation of Magnetic Nozzle Plasmadynamics.* PhD thesis, 2016.

[34] Peter C Stangeby et al. *The plasma boundary of magnetic fusion devices*, volume 224. Institute of Physics Pub. Philadelphia, Pennsylvania, 2000.

[35] LS Solov'ev. The theory of hydromagnetic stability of toroidal plasma configurations. *Sov. Phys. JETP*, 26(2):400–407, 1968.

[36] Mathworks. Partial differential equation toolbox™.

[37] Miguel Ramos Pascual. Fusion cross-sections for deuterium cycle fusion reactors (d-cycle): an analysis of geometric, gamow-sommerfeld and astrophysical s-factors.

[38] JD Huba. Nrl plasma formulary, revised. *Naval Research Lab. Report NRL/PU/6790-16-614, Naval Research Laboratory*, 2013.

[39] George H Miley, Harry Towner, and Nenad Ivich. Fusion cross sections and reactivities. Technical report, Univ. of Illinois at Urbana-Champaign, IL (United States), 1974.

[40] Kenneth Elric Miller. *The Star Thrust Experiment, rotating magnetic field current drive in the field reversed configuration*. University of Washington, 2001.

[41] D Petkow, RA Gabrielli, G Herdrich, R Laufer, and H-P Röser. Generalized lawson criterion for magnetic fusion applications in space. *Fusion Engineering and Design*, 87(1):30–38, 2012.

[42] Tetsuo WATARI, Tadatsugu HATORI, R Kumazawa, S Hidekuma, T Aoki, T Kawamoto, Masaaki INUTAKE, Shinji HIROE, Akimitsu NISHIZAWA, K Adati, et al. Radio-frequency plugging of a high density plasma. *Research Report: IPPJ*, 1978.

[43] Daniele Iannarelli, Francesco Napoli, Antonella Ingenito, Alessandro Cardinali, Antonella De Ninno, and Simone Mannori. A rational design method for the nagoya type-iii antenna. *arXiv preprint arXiv:2412.20839*, 2024.

[44] Max Light and Francis F Chen. Helicon wave excitation with helical antennas. *Physics of Plasmas*, 2(4):1084–1093, 1995.

[45] Ph Guittienne, R Jacquier, B Pouradier Duteil, AA Howling, R Agnello, and I Furno. Helicon wave plasma generated by a resonant birdcage antenna: magnetic field measurements and analysis in the raid linear device. *Plasma Sources Science and Technology*, 30(7):075023, 2021.

[46] Shogo Isayama, Shunjiro Shinohara, and Tohru Hada. Review of helicon high-density plasma: Production mechanism and plasma/wave characteristics. *Plasma and Fusion Research*, 13:1101014–1101014, 2018.

[47] Andrew S Richardson. *2019 NRL plasma formulary*. Naval Research Laboratory Washington, DC, 2019.

[48] Behrooz Soltani and Morteza Habibi. Development of a helicon plasma source for neutral beam injection system of the alborz tokamak. *Journal of Fusion Energy*, 36:152–160, 2017.

[49] Francis F Chen and David D Blackwell. Upper limit to landau damping in helicon discharges. *Physical review letters*, 82(13):2677, 1999.

[50] Thomas H Stix. *Waves in plasmas*. Springer Science & Business Media, 1992.

[51] A Cardinali, Davide Melazzi, Marco Manente, and Daniele Pavarin. Ray-tracing wkb analysis of whistler waves in non-uniform magnetic fields applied to space thrusters. *Plasma Sources Science and Technology*, 23(1):015013, 2014.

[52] F Taccogna, F Cichocki, D Eremin, G Fubiani, and L Garrigues. Plasma propulsion modeling with particle-based algorithms. *Journal of Applied Physics*, 134(15), 2023.

[53] Eduardo Ahedo, Sara Correyero, Jaume Navarro-Cavallé, and Mario Merino. Macroscopic and parametric study of a kinetic plasma expansion in a paraxial magnetic nozzle. *Plasma Sources Science and Technology*, 29(4):045017, 2020.

[54] Makoto Hayashi. Bibliography of electron and photon cross sections with atoms and molecules published in the 20th century. argon. 2003.

[55] AV Phelps. A compilation of atomic and molecular data, assembled and evaluated by av phelps and collaborators, 2010.

[56] F Cichocki, V Sciortino, F Giordano, P Minelli, and F Taccogna. Two-dimensional collisional particle model of the divertor sheath with electron emissive walls. *Nuclear Fusion*, 63(8):086022, 2023.

[57] Adrián Domínguez-Vázquez, Filippo Cichocki, Mario Merino, Pablo Fajardo, and Eduardo Ahedo. Axisymmetric plasma plume characterization with 2d and 3d particle codes. *Plasma Sources Science and Technology*, 27(10):104009, 2018.

[58] Francesca Cherubini. Global science, 2020. January 24, 2025.

[59] Paolo Micozzi, Franco Alladio, Alessandro Mancuso, Vincenzo Zanza, Gerarda Apruzzese, Francesca Bombarda, Luca Boncagni, Paolo Buratti, Francesco Filippi, Giuseppe Galatola Teka, et al. Final results of the first phase of the proto-sphera experiment: obtainment of the full current stable screw pinch and first evidences of the jet+ torus combined plasma configuration. *Plasma Science and Technology*, 26(2):025103, 2024.

[60] Franco Alladio, Paolo Micozzi, Luca Boncagni, Annamaria Pau, Shayesteh Naghinajad, Samanta Macera, Yacopo Damizia, Paolo Buratti, Francesco Filippi, Giuseppe Galatola Teka, et al. Proto-sphera: a magnetic confinement experiment which emulates the jet+ torus astrophysical plasmas. *Plasma Physics and Controlled Fusion*, 66(3):035011, 2024.

[61] J Bryan Taylor and MF Turner. Plasma current drive by helicity injection in relaxed states. *Nuclear Fusion*, 29(2):219, 1989.

[62] D Iannarelli, F Napoli, F Alladio, G Apruzzese, F Bombarda, P Buratti, J Delfini, A De Ninno, F Filippi, D Fiorucci, et al. A new indirect measurement method of the electron temperature for the proto-sphera's pinch plasma. *Journal of Instrumentation*, 18(04):C04017, 2023.

[63] B Tirozzi, P Buratti, F Alladio, and P Micozzi. Bidimensional analysis of the proto-sphera flow. In *2019 Days on Diffraction (DD)*, pages 204–209. IEEE, 2019.

[64] Paolo Buratti, Brunello Tirozzi, Franco Alladio, and Paolo Micozzi. 1-d modeling of the screw-pinch plasma in proto-sphera. *Fluids*, 4(1):42, 2019.

[65] Jeffrey P Freidberg. *Plasma physics and fusion energy*. Cambridge university press, 2008.

[66] Eric T Meier. *Modeling plasmas with strong anisotropy, neutral fluid effects, and open boundaries*. University of Washington, 2011.

[67] GS Voronov. A practical fit formula for ionization rate coefficients of atoms and ions by electron impact: Z= 1–28. *Atomic data and nuclear data tables*, 65(1):1–35, 1997.

[68] F Alladio, P Costa, A Mancuso, P Micozzi, S Papastergiou, and F Rogier. Design of the proto-sphera experiment and of its first step (multi-pinch). *Nuclear fusion*, 46(8):S613, 2006.

[69] Douglass Edmund Post, RV Jensen, CB Tarter, WH Grasberger, and WA Lokke. Steady-state radiative cooling rates for low-density, high-temperature plasmas. *Atomic data and nuclear data tables*, 20(5):397–439, 1977.

[70] Institut atomnoui. energii (Akademiia nauk SSSR) and M.A. Leontovich. *Plasma Physics and the Problem of Controlled Thermonuclear Reactions*. Number v. 4 in Plasma Physics and the Problem of Controlled Thermonuclear Reactions. Pergamon Press, 1959.

[71] Jacopo Delfini. Visible and uv spectroscopy in the fusion plasma of proto-sphera device, 2022.

[72] S Cesaroni, M Angelone, G Apruzzese, F Bombarda, L Gabellieri, M Marinelli, E Milani, S Palomba, G Pucella, A Romano, et al. Cvd diamond photodetectors for ftu plasma diagnostics. *Fusion Engineering and Design*, 166:112323, 2021.

[73] Stephen Jardin. *Computational methods in plasma physics*. CRC press, 2010.

[74] M Coleman and S McIntosh. The design and optimisation of tokamak poloidal field systems in the blueprint framework. *Fusion Engineering and Design*, 154:111544, 2020.

[75] R Albanese, Roberto Ambrosino, and Massimiliano Mattei. Create-nl+: A robust control-oriented free boundary dynamic plasma equilibrium solver. *Fusion Engineering and Design*, 96:664–667, 2015.

[76] P Micozzi, F Alladio, A Mancuso, and F Rogier. Ideal mhd stability limits of the proto-sphera configuration. *Nuclear fusion*, 50(9):095004, 2010.

[77] F Alladio, P Costa, A Mancuso, P Micozzi, S Papastergiou, and F Rogier. Design of the proto-sphera experiment and of its first step (multi-pinch). *Nuclear fusion*, 46(8):S613, 2006.

[78] GS Kurskiev, VK Gusev, NV Sakharov, Yu V Petrov, NN Bakharev, IM Balachenkov, AN Bazhenov, FV Chernyshev, NA Khromov, EO Kiselev, et al. Energy confinement in the spherical tokamak globus-m2 with a toroidal magnetic field reaching 0.8 t. *Nuclear Fusion*, 62(1):016011, 2021.